Design of Auxetic Stents by Topology Optimization

by Huipeng Xue

Thesis submitted in fulfilment of the requirements for the degree of

Doctor of Philosophy

under the supervision of A/Prof Zhen Luo and Dr. Terry Brown

University of Technology Sydney
Faculty of Engineering and Information Technology

October 2020

Title of the thesis:

Design of Auxetic Stents by Topology Optimization

Ph.D. student:

Huipeng Xue

E-mail: **huipeng.xue@student.uts.edu.au**

Supervisor:

A/Prof Zhen Luo

E-mail: **zhen.luo@uts.edu.au**

Co-Supervisor:

Dr. Terry Brown

E-mail: **terry.brown@uts.edu.au**

Address:

School of Mechanical and Mechatronic Engineering

The University of Technology Sydney, Sydney, NSW 2007, Australia

Certificate of Original Authorship

I, Huipeng Xue declare that this thesis, is submitted in fulfilment of the requirements for the award of Doctor of Philosophy, in the School of Mechanical & Mechatronic Engineering at the University of Technology Sydney.

This thesis is wholly my own work unless otherwise referenced or acknowledged. In addition, I certify that all information sources and literature used are indicated in the thesis.

This document has not been submitted for qualifications at any other academic institution.

This research is supported by the Australian Government Research Training Program.

Signature of Student:

Production Note:
Signature removed prior to publication.

HUIPENG XUE

Date: 16/10/2020

Acknowledgments

I would like to take this opportunity to express my deep gratitude to all those who helped me throughout my candidature.

First and foremost, I would like to extend my sincere gratitude to my principal supervisor, A/Prof. Z Luo. During the studying of the course and the writing of the thesis, he had contributed greatly by giving useful suggestions and constructive criticism. He devoted a considerable portion of his time to reading my manuscripts and making suggestions for further revisions. Moreover, he gave me many encouragements and other help in my study and life. Also, I would like to express my heartfelt gratitude to my co-supervisor Terry Brown and my technical instructor Dr. Jindong Yang for their support and guidance. Their outstanding knowledge, intelligence and wisdom have a profound influence on me.

I also wish to express my gratitude to Dr. Hao Li and Dr. Yu Wang. They offered me great help and gave me many valuable suggestions. My sincere thanks should also go to my colleagues Jing Zheng, Jie Gao, Shuhao Wu, Xianfeng Man and Zuyu Li for their support.

My last and special thanks would go to my beloved family for their loving considerations and great confidence in me all through these years.

Huipeng Xue

Sydney, 2020

Publications and Conference Contributions

International scientific journal publications:

[1] **H. Xue**, Z. Luo, T. Brown, & S. Beier, Design of Self-Expanding Auxetic Stents Using Topology Optimization. Frontiers in Bioengineering and Biotechnology, 2020. 8: p. 736.

[2] J. Gao, **H. Xue**, L. Gao, & Z. Luo, Topology optimization for auxetic metamaterials based on isogeometric analysis. Computer Methods in Applied Mechanics and Engineering, 2019. 352: p. 211-236.

[3] **H. Xue**, Z. Luo, S. Beier, & B. Halkon, Design of Self-Expanding Auxetic Coronary Stents by Considering Hemodynamics Using Topology Optimization. IEEE Transactions on Biomedical Engineering, about to be submitted.

International scientific book section:

[4] **H. Xue**, & Z. Luo, Design of Auxetic Coronary Stents by Topology Optimization, in Computational Biomechanics for Medicine. 2019, Springer. 17-31.

International conference publications:

[5] **H. Xue**, & Z. Luo, Negative Poisson's Ratio Design of the Cardiovascular Stent

Using a Level Set-based Parameterization Method. In: The 13th World Congress on Computational Mechanics (WCCM 2018), New York.

[6] **H. Xue**, P. Johal, Z. Luo, & T. Brown, Design of Auxetic Coronary Stents Using Topological Optimization. In: The 13th World Congress of Structural and Multidisciplinary Optimization (WCSMO 13), Beijing.

List of Figures

List of Tables

Abbreviations

BE	Balloon-expandable
BESO	Bi-directional Evolutionary Structural Optimization
BMS	Bare-metal stent
BVS	Bioresorbable vascular scaffolds
CAD	Coronary artery disease
CFD	Computational fluid dynamics
CFL	Courant–Friederichs–Lewy
CoCr	Cobalt-chromium
CSRBF	Compactly supported radial basis function
CT	Computed tomography
DAPT	Dual antiplatelet therapy
DES	Drug-eluting stents
ESO	Evolutionary structural optimization
FDA	Food and Drug Administration
FEA	Finite element analysis
FSI	Fluid-structure interaction
HJ-PDE	Hamilton-jacobian partial derivative equation
ISR	In-stent restenosis

IVUS	Intravascular ultrasound
LSM	Level set method
MFP	Modified fluid permeability
MMC	Moving morphable components
NIH	Neointimal hyperplasia
NPR	Negative Poisson' ratio
NS	Naiver-stokes
OC	Optimality criteria
OCT	Optical coherence tomography
ODE	Ordinary differential equation
PCI	Percutaneous coronary intervention
PLSM	Parametric level set method
PtCr	Platinum-chromium
SE	Self-expanding
SIMP	Solid Isotropic Material with Penalization
ST	Stent thrombosis
TAWSS	Time-averaged wall shear stress
WSS	Wall shear stress
WSSG	Wall shear stress gradient
X-PLSM	Extended parametric level set method

Abstract

As high efficiency and minimal invasive, percutaneous coronary intervention with stents is a popular treatment for coronary artery disease but suffering from the risks of stent thrombosis and in-stent restenosis. Apart from the biological factors, stenting structures have been demonstrated to have strong associations with the incidences of these complications. The impacts of stenting structures mainly concern two aspects, the mechanical failures, and the induced hemodynamic changes. This thesis introduces mechanical metamaterials and topology optimization into stent design to overcome the limitations. As a kind of artificially engineered metamaterials, the auxetic material with unique mechanical properties due to the effective negative poison's ratio is incorporated into the stent design to overcome mechanical failures of the conventional stenting structures. Based on the auxetics, a multiscale topology optimization method is developed to generate auxetic stenting structures to enhance their mechanical performances. Additionally, a modified fluid permeability is proposed to quantify the stent induced obstructions to the blood flow. It successfully combines hemodynamic considerations into the developed topology optimization design for stents.

Chapter 1 provides a brief introduction to this research. Chapter 2 gives the background and a comprehensive literature review, including different coronary stents, the mechanical and hemodynamic factors of the complications, the stenting optimization, topology optimization, multifunctional artificial cellular composites, and auxetic metamaterials.

In Chapter 3, an extended parametric level set method (X-PLSM) is proposed to transform the parametric level set method (PLSM) from the cartesian coordinate system to a curvilinear system. Thus, the X-PLSM can implicitly represent the boundaries of shell structures efficiently rather than using the conventional PLSM for 3D models, which can benefit the design of stents.

In Chapter 4, a multiscale topology optimization based on X-PLSM is developed to introduce auxetics into the design of self-expanding (SE) stents, aiming to enhance the stenting performances and overcome their mechanical failures. Then, the optimized auxetic SE stent is numerically validated in software ANSYS and prototyped using additive manufacturing techniques.

In Chapter 5, a modified fluid permeability (MFP) is proposed to quantify the stent induced obstructions to the blood flow. After that, a multiscale multi-objective topology optimization based on PLSM is developed and performed to introduce the auxetic properties, maximize macroscopic stiffness, and minimize the stent induced obstructions. During the optimization, the impacts of each design objective function on the stenting structures are discussed.

In Chapter 6, the deformation mechanism of the optimized stents and the surrounding blood flow is numerically simulated in ANSYS and CFX, respectively.

Finally, conclusions and prospects are provided in Chapter 7.

Contents

Chapter 1 Introduction

1.1 Overview of the project

Implanting stents is the most efficient intervention technique for treating coronary artery diseases but cannot eliminate the risks of stent thrombosis (ST) and in-stent restenosis (ISR). Over the past 40 years, numerous stents have been applied in the clinic practice, but a systematic design optimization method to enhance deliverability, safety, and efficacy is still in demand. However, most current stent designs mainly focus on patient and biological factors, underestimating the mechanical failures related to stenting structural architectures, such as inadequate stent expansion, stent fracture, stent malapposition, and foreshortening. Since the mechanical failures have been demonstrated to associate with the increase of the complication incidences, many studies began to improve the mechanical performances of stents by structural optimizations. However, most of current works were only focused on parameter optimization based on surrogate models, and only limited improvements can be obtained.

Topology optimization, as the latest development of structural optimization technique, provides an efficient way to iteratively find the best material distribution when the objective function is optimized under given design constraints in the prescribed design domain. Based on an initial design it can finally achieve a new topology for the structure. Thus, this thesis aims to introduce the auxetic metamaterials into the conventional stent

structures and then topology optimization method is applied to search the best topology for the auxetic stenting architecture, to overcome the limitations in current designs.

On the other hand, concerning the above mechanical factors, the self-expanding (SE) stents may perform better than the balloon-expandable (BE) stents due to the difference of their deformation mechanisms. However, the poor deliverability, placement accuracy, and precise size requirements of the SE stents make them not popular in today's clinical applications. Hence, we will develop a multiscale topology optimization method to find new SE stenting structures with auxetic features to overcome the drawbacks of the current SE stents. Thus, the occurrence of the above mechanical failures can be significantly reduced by using the topologically optimized auxetic stents, correspondingly resulting in reduced incidences of ST and ISR. In the topology optimization method, an extended parametric level set method (X-PLSM) with shell elements is proposed to enhance computational accuracy and efficiency during the optimization, with the numerical homogenization method to realize the design of auxetic microstructures.

However, apart from mechanical failures, the adverse hemodynamic changes caused by the stent implantation are also associated with the risks of ISR and ST due to the change of the wall shear stress (WSS). Moreover, the hemodynamic changes were highly related to the structural characteristics of stents. Hence, the structural optimization design for stents should consider the impacts on surrounding blood flow.

A modified fluid permeability (MFP) is proposed to quantify obstructions to fluid along with different directions of the microstructures. Then, the purpose of reducing the adverse

hemodynamic changes around stents can be obtained by minimizing the MFP in other directions except for the direction of blood flow. Thus, the hemodynamic topology optimization can get results by single objective function MFP. Besides that, the proposed MFP can also be computed by the numerical homogenization method. Therefore, we will further develop an improved multiscale topology optimization method considering the multiple design criteria in the SE stents, aiming to reduce the incidences of ST and ISR caused by both mechanical and fluid aspects. In the optimization, the design of auxetic properties can improve the flexibility and deliverability of SE stents, and the adverse fluid motions caused by the stent can be reduced by minimizing the MFP in other directions except for the direction of blood flow. A Darcy-Stokes coupling system is established to describe both solid and fluid behaviors in stenting microstructures. Besides that, the macroscopic stiffness of the stent is also under consideration in the optimization. Finally, all the design works are numerically validated in the commercial software ANSYS.

1.2 Research contributions

This thesis aims to improve the stent performances by structural topology optimization. Two aspects of stent performances are considered in the research: mechanical performances and the induced hemodynamic changes. On the one hand, this research introduces auxetic metamaterials into stent designs to overcome the mechanical failures. On the other hand, stent induced hemodynamic changes are also considered by MFP in the design to improve the flow environment around the stent. The specific objectives and contributions are given as follows:

1) The parametric level set method (PLSM) can simultaneously perform topology and shape optimization, obtaining smooth and clear structural boundaries. Since the stenting performances are highly sensitive to the stenting structural topology and shape, PLSM is suitable for the stent designs. However, due to the particular characteristics of stenting structures, the result may lose accuracy and computationally expansive by using conventional PLSM method. Thus, an extended parametric level set method (X-PLSM) is developed for the thin-walled shell structures of stents. In X-PLSM, the level set model is converted from the Cartesian coordinate system to a curvilinear system. By doing this, a shell element with four nodes can be adopted to discretize stenting structures. Therefore, the developed method can efficiently and accurately perform design for stents.

2) The risks of ST and ISR by using stents can be reduced by overcoming the related mechanical failures. However, these issues currently are not well addressed. In this work, the auxetic mechanical metamaterials will be introduced into SE stents, by making use of their unusual mechanical properties due to the negative Poisson' ratio (NPR), to help overcome the mechanical failures and therefore reduce the incidences of ST and ISR. We intend to empower the SE stents with new performance to reduce the mechanical failures and the injuries to the coronary arteries. Thus, the design of the SE stents is converted to a problem for how to overcome the drawbacks of today's SE stents while keep their favourable features. A multiscale topology optimization method is then developed based on the X-PLSM to implement the auxetic SE stents.

3) The stent induced adverse hemodynamic changes are strongly associated with the high incidences of ST and ISR. We propose a modified fluid permeability (MFP) to quantify the obstructions of stents on the blood flow in topology optimization. It is challenging to consider both mechanical and fluid factors in the optimization. Based on MFP, we develop an improved multiscale multi-objective topology optimization method for SE stents to account for the hemodynamic changes.

1.3 Outline of the thesis

The thesis consists of 7 chapters, shown as follows:

Chapter 1: The overview and research contributions of this thesis are introduced.

Chapter 2: A literature review is provided for coronary stents, the mechanical and fluid factors in stent designs, stent optimization, topology optimization, multifunctional artificial cellular composites, and auxetic metamaterials.

Chapter 3: The X-PLSM based on PLSM is developed and discussed.

Chapter 4: A multiscale topology optimization model is established to introduce auxetics into SE stents. The numerical validations and the printed prototype are provided.

Chapter 5: The MFP is proposed. A multiscale multi-objective topology optimization model is developed for stent design by considering both mechanical and fluid aspects.

Chapter 6: The deformation mechanism of the optimized stents and the surrounding blood flow are numerically simulated in software ANSYS and CFX, respectively.

Chapter 7: Conclusions of this work and further recommendations are presented.

Chapter 2 Literature review

In this chapter, the developments of different coronary artery stents are reviewed and discussed. The mechanical and hemodynamic factors associated with stent performances and related optimization strategies are summarized, respectively. This thesis aims to introduce topology optimization and auxetic metamaterials into stent designs. Thus, both of them are also reviewed in this section.

2.1 Coronary artery stents

Coronary artery disease (CAD) is the globally leading cause of death with the majority concerns in recent decades [1]. The statistics in 2015 show that 110 million people were affected by CAD, with 8.9 million deaths [2, 3]. The treatments for CAD are rapidly developed for more than 40 years, but they cannot eliminate the related complications. That is also the reason why it has the highest morbidity and mortality. The successful applications of coronary artery stents provide more efficient treatments for CAD but still facing the risks of different complications. Hence, the evolution of stents has been driven by the purpose of reducing the incidences of these complications.

2.1.1 Bare-metal stents (BMS)

In 1964, Charles Dotter and Melvin Judkins [4] proposed a concept of angioplasty, setting up the bases for developing the first balloon coronary angioplasty by Andreas Grüntzig

in 1977 [5]. The treatment generated a new subject named interventional cardiology [6]

and promoting the development of percutaneous coronary intervention (PCI) technology.

However, the high rates of restenosis and abrupt closure of arteries after angioplasty arose

the safety challenges [7, 8], prompting in the birth of stent implantation [9].
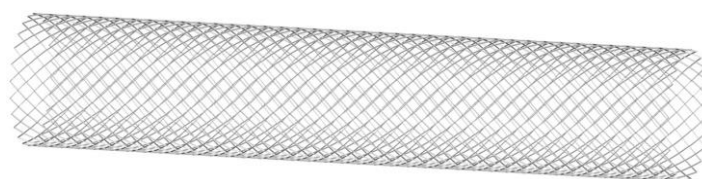
Figure 2-1 A typical bare-metal stent

The first balloon-expandable (BE) intracoronary bare-metal stent (BMS) was implanted

in a dog [10]. In 1986, the self-expanding (SE) coronary stent made of stainless steel was

firstly implanted in a human patient to prevent occlusion and restenosis after angioplasty

[11]. Early coronary stents showed efficiency in treating abrupt and susceptible vessel

closure [12]. Their applications were still significantly hampered due to the high rate of

subacute thrombotic coronary artery occlusion after implantation [13]. After two famous

comparison trials (BENESTENT and STRESS) [14, 15] were performed to investigate

stent implantation and balloon angioplasty, two stents were approved by the Food and

Drug Administration (FDA) in the US in 1994. The safety of coronary stents was then

widely accepted in clinics, and most PCI procedures began to adopt stent implantation. A

typical BMS structure is presented in Figure 2-1.

The apparent advantage of implanting stents is the efficient continuous support for

clogged arteries. However, stents also suffer from the risks of stent thrombosis (ST) and in-stent restenosis (ISR) [16]. ST is a complicated multifactor induced complication. It is rare but with high mortality (5-45%) and relapse rate (15–20%) at five years [17]. In order to reduce the incidence of ST, the accompanying pharmacotherapy was usually used, such as dual antiplatelet therapy (DAPT) [18]. However, ST in BMS cannot be eliminated, and with a rate of about 1.2% [19]. Another complication by implanting stents is ISR, which is caused by neointimal hyperplasia (NIH) and belonging to widespread biological responses after PCI. ISR significantly decreases the efficiency of stents, leading to revascularization. Although numerous therapies have been proposed to control ISR since the development of PCI, it is about 20-30% incidence of ISR in BMS when facing long-term treatments [19]. The high rate of ISR directly results in the birth of first-generation drug-eluting stents (DES).

2.1.2 Drug-eluting stents (DES)

The first-generation DES [20-22] carrying local drug delivery platforms were proposed to prevent NIH efficiently, leading to a reduction in ISR. A typical DES consists of three components: the metal stenting platform (the same as BMS), the polymer coating to store and release drugs, and the antiproliferative drugs, such as sirolimus and paclitaxel for the first-generation DES [23, 24]. A typical DES structure is illustrated in Figure 2-2. Even though the NIH can be significantly limited by drugs released from drug-eluting stents (DES), the antiproliferative drugs also prevent the formation of a new endothelial layer.

However, in vascular healing, endothelialization plays an essential role in inhibiting clot formations. Besides that, the polymer coatings might activate hypersensitivity reactions of the arteries and lead to an increased rate of ST. The evidence showed that the first-generation DES can effectively reduce the ISR incidence to 5-15 % at 12 months [25], but leading to an increased rate of late and very late ST (up to 2%) [26, 27]. Thus, the second-generation DES was developed by seeking new stenting platforms, new drugs, and related polymer coatings.
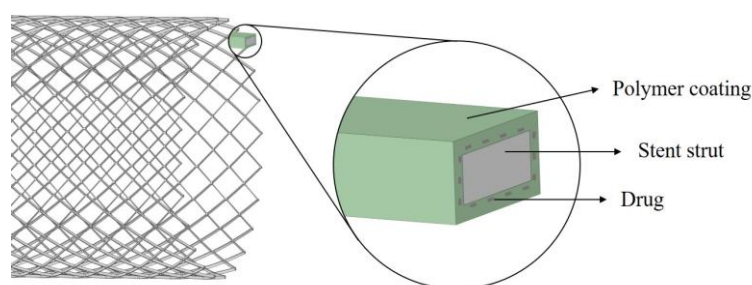
Figure 2-2 A typical drug-eluting stent

In the second-generation DES, the stenting platforms adopted metal alloys, such as cobalt-chromium (CoCr) and platinum-chromium (PtCr), leading to thinner struts thickness, higher radial strength, and flexibility [28]. The applications of new drugs, such as zotarolimus, everolimus, and novolimus, exhibited more safety and efficient results [29]. The developed new polymers were more biocompatible with less inflammatory response and faster drug elution [30]. The applications of the second-generation DES successfully further reduce the incidence of ISR to less than 5% incidence within 12 months [19]. Moreover, the second-generation DES exhibits a 0.7% rate of ST [29] and

is superior to other current stents. However, the duration of DAPT is still needed for at least one year [27, 31]. Besides that, the long healing time is still facing late stent failures that may increase the risks of ISR and ST.

No matter for the first or second-generation DES, the durable polymer poses a risk of hypersensitivity reactions and affect the incidence of ST. Thus, the polymer-free DES is developed to overcome the drawbacks of durable polymers. The surface of the polymer-free DES is manufactured with porous to carry antiproliferative drugs. However, it is tough to control the drug release rate, and the stents were demonstrated that cannot further improve the DES [32]. Another improvement for DES is the stents with biodegradable polymers, such as poly-DL-lactide-co-glycolide or PLLA [30]. The DES with a biodegradable polymer can act as a standard DES in the early treatment to reduce the ISR rate and becomes a BMS when the polymer disappeared to decrease the duration of DAPT [33]. However, apart from the advantages in the early treatment, the results of very late ST did not show any improvement, compared with the second-generation DES [34, 35].

2.1.3 Bioresorbable vascular scaffolds (BVS)

Once deployed, stents permanently exist in the artery. All the stents with permanent platforms or polymer coatings face the risks of late stent failures [36]. The bioresorbable vascular scaffolds (BVS) is developed to support the clogged artery but can degrade during the treatment to avoid long-term risks [37]. However, due to the material properties, the BVS has to adopt thick struts to obtain enough radial strength, significantly affecting

blood flow in the stented segment and facing an incomplete expansion [38]. Besides that, the most risk comes from the increased incidence of device thrombosis. Moreover, inferior clinic outcomes of BVS led to a withdrew of the first commercial Absorb BVS from the market in 2017, which was just approved by the FDA in 2016. Thus, the BVS exhibits significant potential but facing big challenges.

2.1.4 Balloon-expandable (BE) and self-expanding (SE) mechanism

Based on the expansion mechanism, stents can be divided into balloon-expandable (BE) stents and self-expanding (SE) stents. By the inflation of an inside balloon, BE stents are plastically expanded from the crimped-state to match the artery diameter [39]. SE stents are constructed to fit the artery diameter and constrained within a delivery catheter. When deployed, the SE stents are released from the catheter and elastically recover to the initial shape or a slight compressed state. The property of SE can be obtained in several ways, such as adopting superelastic shape-memory materials or mechanical 'spring-like' designs. Because of easy to be deployed precisely, most commercial coronary stents utilize BE stenting platforms. However, concerning some atypical and complex coronary lesions [40, 41], SE stents are superior to other stents due to the characteristic of positive remodelling. Recently, as the developments, the unique properties of SE stents reattract interests, which can be demonstrated by the successful clinic applications of commercial product Stentys® Self-Apposing® stent [42]. To further discuss the differences between BE and SE stents, both advantages and disadvantages are summarized in the following.

1) BE platforms

Since the insider balloons control the expansion of the BE platforms, the most advantages of the BE mechanism are easily positioned and precisely deployed [43]. Besides that, BE stents have strong universality when matching the diameter of the vessel due to the expansion size controlled by balloons. Another benefit of BE platform is the good deliverability, compared with the cumbersome delivery devices of the early SE stents. On the other hand, the drawbacks of BE platforms are also obvious. (1) The permanent deformations cannot adaptively match the changes of the vessel diameters during the treatments, which may lead to malapposition. (2) The expansion of a BE stent is driven by the inflation of the balloon. It may easily cause inadequate expansions or dogboning phenomena. (3) During the expansion, BE stents often cause immediate vessel injury and even edge dissections. All these drawbacks can significantly increase the incidence of complications.

2) SE platforms

SE platforms usually adopt superelastic materials, such as Nitinol. They have better mechanical performances, such as high fracture toughness, corrosion resistance, and good biocompatibility. The benefits of SE platforms mainly focus on the following aspects. (1) The BE stents exhibit a gradual expansion process, resulting in no-reflow, lower edge dissections rates, and adequate expansion [44]. (2) The gradual expansion process can

also avoid the immediate vessel wall injury to reduce acute thrombosis and NIH [43]. (3) Due to the elastic deformation mechanism, SE platforms can adapt to the changes of the vessel diameter to prevent the late stent malapposition [40, 44]. Thus, SE stents can effectively support the enlarged vessel after the disruption of plaques. (4) SE platforms exhibit better flexibility due to material elasticity, especially for bifurcations and significant tapering vessels [41], leading to a low fracture incidence.

However, some drawbacks of SE stents significantly hinder their popularity in applications. (1) The early SE stents had poor deliverability with cumbersome delivery systems, although they have been improved in the current SE stents. (2) The phenomenon of foreshortening during the expansion leads to much lower deployment accuracy [43]. The deviation of deployment can lead to uncovered lesions, resulting in a high risk of thrombosis complications. (3) SE platforms are manufactured to match the target vessel diameter or slightly above, leading to a high requirement for the size. However, it is difficult to measure the dimensions of the target vessel precisely in clinical cases. Thus, it may result in an over-small size causing stent malapposition or an over-large size, causing a larger lumen [6].

2.2 Mechanical factors in stent design

The associations between stenting structural designs and their clinical outcomes are investigated but are still underestimated. The performances of stents not only depend on

the patient's factors, stenting materials, and drugs but also strongly rely on the stenting structural architectures, because stents are first a kind of structures subject to loading. Thus, how to improve stent structures and their associated performances will be expected to reduce the risks of complications.

2.2.1 Mechanical failures

Apart from patient and biological reasons, the increased incidences of ST and ISR are strongly correlated with stenting mechanical failures, such as foreshortening, dogboning, recoil, inadequate expansion, malapposition, and fracture.

The foreshortening exists in the stents when expanding after the implantation due to the stenting material properties: positive Poisson' ratio. It increases the difficulty of stent deployments and easily leading to uncovered lesions. The issue of dogboning only occurs in BE stents. It is caused by nonuniform balloon expansion, resulting in the expanded stent with a dog-bone-like shape [45]. Besides that, the occurrence of dogboning may induce edge dissections to damage the artery. The stent recoil also only exists in BE stents and is caused by elastic recoil after plastic deformations of the stent. The risk of stent recoil is to generate gaps between the stent and the vessel wall. The gaps can also be caused when suffering inadequate stent expansion. Stent malapposition, or incomplete stent apposition, indicates the stent struts that do not tightly contact the vessel wall and leave gaps between them. Stent malapposition is of great importance because it can increase the risk of subsequent ST [46]. The stent fracture is the worst failure that directly

threatens the patient's life [6]. The above mechanical failures can be summarized as causing gaps between stents and vessel walls or injures to vessel walls. Both of the results can active NIH and leading to a high incidence of ISR [47]. The evidence also shows that these mechanical factors were strongly associated with late or very late ST [17].

2.2.2 Stent designs

Hundreds of different stents are designed in the following few decades after the successful applications of coronary stents in PCI. A typical stent consists of periodic structural unit cells, and different struts comprise each unit cell. These struts are approximately oriented to the stenting axial direction and periodically distributed around the circumference, forming periodic U-, V-, S-, or N-shapes [48]. Two typical structures of stents are illustrated in Figure 2-3, where transverse bridges connect the struts in different circumferences. From the figure, we can see the stents consist of V-shape periodic struts and S- or I-shape bridges or links. Most stents are also designed based on similar simple strut shapes. Thus, in the early period, the traditional stenting structures were usually designed depending on experience and further improved based on clinical trials and the results from patients.
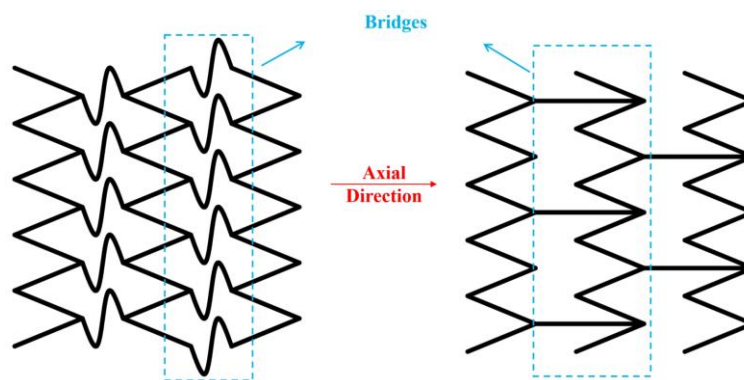
Figure 2-3 Two typical stenting structures

As a computational simulation tool, the finite element analysis (FEA) can numerically evaluate stenting mechanical performances and efficiently guide stent designs [49-51]. Thus, more and more studies have performed stent designs based on FEA [52, 53]. Most of these studies improve the mechanical performances of stents by evaluating different stenting structural variables belonging to size or shape optimization methods. Among that, the optimization based on surrogate models has been utilized for the design of stents [54]. A typical example of stenting design is illustrated in Figure 2-4. As discussed, stenting structures are determined by the periodic unit cells, so the optimization for the stent can be performed for one unit cell with identified parameters. In the example, five structural parameters are defined. Thus, by creating response surfaces in surrogate models, the association between the parameters and specified design objective functions are established. Then, the design can be achieved by selecting proper combinations of the parameters. The design objectives are usually adopted based on the above mechanical failures and some crucial performances of stents, such as flexibility, radial stiffness, and fatigue. The structural design variables are the strut thickness, bridge width and length,

strut width and length, curve radius, profile shape, and pattern numbers.
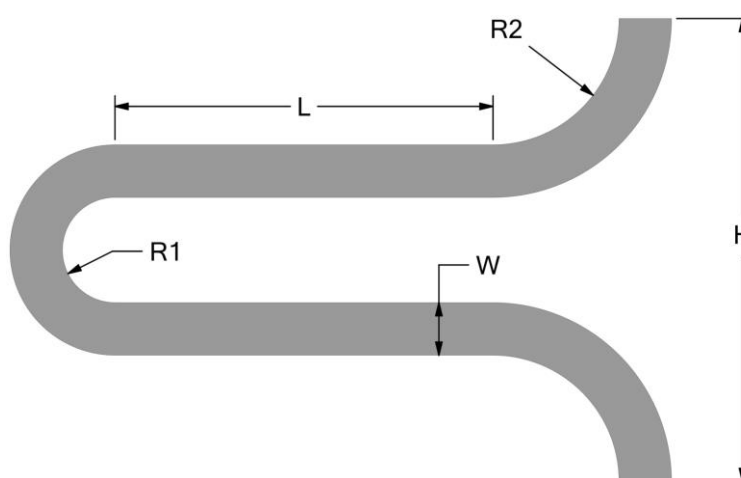
Figure 2-4 A parametric strut for optimization

The optimization for stents aims to enhance the performances and then the safety. Since different kinds of stents are affected by specific factors, the optimization designs are only performed for specific stent types, such as dog-boning and recoil for BE stents, and corrosion resistance for biodegradable or bioabsorbable stents. As for some universal design objectives, such as foreshortening, flexibility, radial stiffness, and fatigue, the related optimization designs are also different by adopting different stent types.

Stent flexibility and longitudinal stiffness were investigated as essential considerations for BE stents [55]. Some studies found that the properties are strongly related to the link shapes and numbers [56, 57]. The phenomena of dog-boning and elastic recoil in BE stents can cause significant stent malapposition or vessel injury, which were studied simultaneously in multi-objective optimization models [58]. As the prevalent issue in both BE and SE stents, foreshortening was usually defined as an objective in stenting

optimization works [53]. Because of cyclic pulsatile loads from heart beating, the fatigue resistance is another essential optimization objective and widely studied, especially for SE stents [59, 60]. As the newly developed stent types, stents with biodegradable polymer and fully bioabsorbable stents strongly rely on optimization designs to consider corrosion resistance and related stress distributions. Some studies [50, 61] have already successfully improved the bioabsorbable stents via optimization designs to some extent.

Although some stenting optimization works have already achieved good results, the related improvements are limited only within a narrow range. That is because most optimization studies adopt different surrogate models. The final structures after optimization are restrained by their given shape and topologies and cannot obtain new layout with different material connectivity for stenting structures. Few studies also tried to use topology optimization to minimize stent recoil [62] and eliminate foreshortening [63]. However, the optimized results cannot maintain the requirements of stents due to numerical instabilities issues and less engagement of stent working conditions.

2.3 Hemodynamics in stent design

Apart from the effects of mechanical factors discussed above, the hemodynamic change caused by implanting stents is another essential aspect associated with high risks of ST and ISR [64, 65].
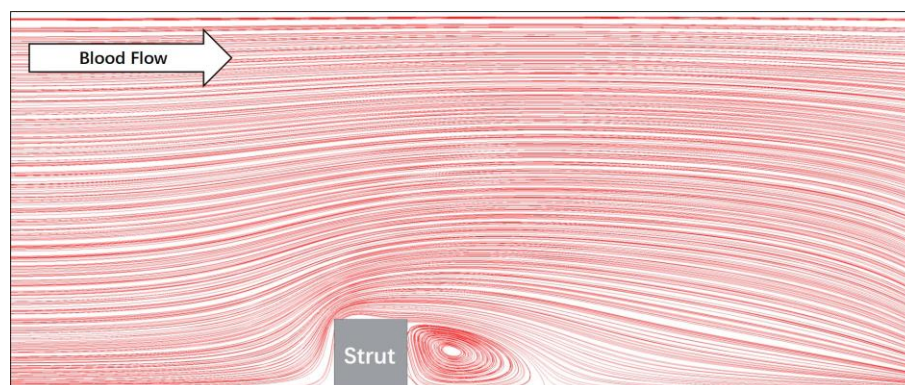
Figure 2-5 Blood obstruction of stent strut

Stents can open narrowed arteries to positively restore blood flow but change flow patterns in the stented segments due to stent induced obstructions [54] and geometric alterations of arteries [66]. The obstacles from stenting struts can cause flow disturbances, flow separation, and recirculation zones to adversely affect distributions of shear stress on the artery walls [67], leading to platelet deposition and smooth muscle cell proliferation [68, 69]. The modifications of the artery shape can magnify the hemodynamic changes [66], but the geometric alterations are mainly determined by the flexibility of the stent, which is not discussed in this chapter. A simple example simulated in the commercial software CFX 2019R3 presents the flow patterns disturbed by a stent strut in Figure 2-5. The example illustrates the stent geometry plays a crucial role in determining hemodynamic changes in the artery. Hence, how to minimize the adverse stent hemodynamic conditions is another essential consideration in the stent design.

2.3.1 Metrics of hemodynamics

The shear stress on the endothelial cells of coronary arteries was demonstrated as a major

factor associated with atherosclerotic disease development [65, 70] and determined by

the blood flow. Therefore, to evaluate the impact of stent implantation on hemodynamic

changes, wall shear stress (WSS), and the derived wall shear stress gradient (WSSG) and

time-averaged wall shear stress (TAWSS) are widely adopted as metrics [71, 72].

Table 2-1 The impact of WSS magnitude on the stent region

WSS(Pa)	Impact of WSS on the stent region
< 0.5	Prone to atherosclerosis
> 1.2	Less atheromatous narrowing [73] and more positive remodeling [74]
< 1.5	Intimal hyperplasia is promoted by the release of tissue growth factors
> 2.5	At the high risk of plaques rupture to increase the incidence of thrombosis and occlusion [75]

WSS is generated when blood flows across the endothelium and proportional to the blood

viscosity and the velocity gradient [76]. It is strongly related to the artery response to

hemodynamics and correlated with diameter adaptive responses, intimal thickening, and

platelet thrombosis [70]. The distributions of WSS will be changed after implanting stents

due to the altered velocity profile of the blood flow in the stent segments [77]. A steady

laminar distribution of WSS can promote endothelial cells release factors to inhibit

coagulation, migration of leukocytes, and smooth muscle proliferation, facilitating the

healing of narrowed vessels [78]. However, abnormal WSS can cause neointimal

hyperplasia and atherosclerotic plaque formations [71]. Many studies [73-75, 79] have

shown that the regions with low WSS are prone to intimal thickening and atherosclerosis, while high WSS may increase the risk of plaque rupture and thrombosis [64]. The effects of WSS magnitude can be summarized in Table 2-1. However, except for the commonly accepted thresholds 0.5 and 2.5 Pa, no exact values of WSS are defined in the range of 0.5-2.5 Pa to distinguish the behaviors of positive vessel remodeling and adverse intimal hyperplasia. Ku [70] demonstrated WSS less than 1.0 Pa might lead to a continuum of adverse action, as well as in the WSS higher than 2.0 Pa. Therefore, the ideal WSS is approximately in the range of 1-2 Pa [64, 71].

The various responses of vascular endothelium to the WSS can be well quantified in the uniform fluid condition with a steady-state. However, in the unsteady flow regions, WSSG is more sensitive to the influence of nonuniform flow on endothelial cells [80, 81]. The WSSG can be described as the rapid changes of WSS over short distances [64]. The regions with WSSG above 200 Pa/m are usually associated with atherogenesis and suffer from intimal hyperplasia [82]. The high WSSG can also increase endothelial permeability and accelerate platelet activation and thrombus formation [80].

TAWSS is a metric used to quantify responses of arteries to the pulsatile blood flow state. It is the averaged WSS over one cardiac cycle. The approximate value of TAWSS was 1.4 Pa found in healthy human coronary arteries [83], while TAWSS with a value of less than 0.5 Pa is associated with cellular proliferation and intimal thickening [70].

2.3.2 Investigations of stent strut geometries

The protrusion of stent struts inside the arterial lumen can disturb blood flow, induce local hemodynamic changes, and affect the distributions of WSS and related metrics in the stented segments. Theoretically, the flow disturbance can be eliminated by the stent fully embedded in the artery walls [64]. However, by doing this, the over-sizing stent can generate high tension stress on the wall and cause injury [84]. In other words, the degree of stent protrusions should be reduced to decrease the obstructions to the blood flow but unavoidable. Thus, the effects of varying strut geometric characteristics on blood flow have been widely investigated, aiming to minimize the adverse hemodynamic reactions via stent design. The computational fluid dynamics (CFD) method provides an efficient tool to measure hemodynamic metrics in the stent segments. It has been widely utilized in both *in vivo* and *in vitro* studies [85].

In the early time, some studies began to detect that stent design may dictate restenosis and thrombosis in the arteries in some other ways, except for mechanical injures [86, 87]. Neointimal hyperplasia independent of arterial injury associated with stent design was first investigated in stented rabbit iliac arteries [88]. It indicated that stent design might adversely affect fluid dynamics in the arterial lumen and induce intimal thicken. At the same time, the study by Berry et al. [89] demonstrated that enlarging strut spacing can facilitate blood flow and minimize the cumulation of neointima in a stented coronary artery. The inverse proportion relationship between neointimal hyperplasia and WSS

change after stent implantation was found by Wentzel et al. [90] and further studied by LaDisa et al. [91]. After that, geometric parameters of stent struts were regarded as critical hemodynamic considerations in the stent design and have been widely studied [54, 85, 92-94].

Among the investigations of stenting geometric characteristics, strut thickness holds most concerns because it directly determines the degree of stent protrusion inside the lumen and is strongly related to hemodynamic changes. Thicker struts were found significantly promoting intimal thickening [85]. Strut spacing is another essential factor where large spacing can restore disturbed flow [95]. Since the adverse hemodynamic changes usually exhibit flow disturbance, streamlined stent strut cross-section profiles were suggested to facilitate blood flow [92]. Besides that, some hemodynamically beneficial designs were also found when varying strut angles [93], such as aligning the orientations of struts and connectors to the flow direction [64, 95].

However, the complicated working environments in stented segments lead to numerous variables to the investigations of stenting geometries. Thus, most studies adopt some geometric simplifications for stent-artery CFD models. A common assumption is that artery walls are rigid. However, some experiments found that deformations on the artery walls were observed after implanting stents [96, 97]. Although the deformations of the arteries may change local flow environments and even affect the WSS distribution [54], the induced influences on the blood flow are relatively small. Another widely used

simplification is to assume the artery as an idealized cylinder in the CFD model to facilitate computation. However, the blood flow environment in a realistic stented coronary artery is quite different. Some researchers began to investigate the impact of the realistic geometric parameters of the stent on the hemodynamic changes, aiming to obtain more accurate results. In 2011, Gundert et al. [98] and Ellwein et al. proposed that the fluid domain of the postoperative stented coronary artery can be established by clinical images [99]. Then, Chiastra et al. [100] demonstrated that it is possible to use patient-specified stented artery models to quantify hemodynamics. After that, some researchers [101-103] began to focus on the studies of patient-specified models, but the complex of 3D reconstruction works hampers the development. The clinical imaging technologies are usually needed for the reconstructions, such as conventional angiography, computed tomography (CT) angiography, intravascular ultrasound (IVUS), and intravascular optical coherence tomography (OCT) [104]. Thus, the patient-specified realistic stent models may get more accurate hemodynamic results to benefit specified patients, but the simplified stent-artery CFD models are more suitable for the related research works.

2.3.3 CFD models

Based on CFD, by solving Naiver-Stokes (NS) equations, the motion equations of fluid, the hemodynamic changes in stented coronary arteries can be calculated as follows. The distributions of WSS can be derived from the velocity and pressure fields of stented arteries, which are computed by CFD with proper initial conditions. The CFD results

strongly rely on the established NS equations, including fluid geometries, the boundary conditions of the inlet, outlet, and artery walls. However, the computational cost is very high to solve the full NS equations. Thus, the assumptions based on the studies of Young and Tsai and Gould [105-107] are widely utilized to simplify the fluid motion equations [65]. The common assumptions are:

(1) Idealized straight arteries [85] & generic bifurcations [108], or patient-specified

The stented artery geometry determines the fluid domain and is associated with the discretization of the CFD model, affecting the computation cost. As discussed above, the adoption of a patient-specified stented vessel may obtain a more accurate outcome but with extremely high computation cost. Besides that, the realistic models usually include the lesion-specific characteristics [109], increasing the difficulty of computation. Therefore, when there is no patient-specific profiling requirement, the idealized straight arteries or generic bifurcation models are usually adopted.

(2) Newtonian or non-Newtonian fluid

Shear stress in the artery depends on the viscosity of blood. Thus, the selection of a Newtonian or non-Newtonian blood model can lead to different WSS distribution. Some studies believe that the non-Newtonian blood model, such as the Carreau-Yasuda model, can obtain more accurate hemodynamics in coronary arteries [110, 111], especially for the shear-thinning behavior of blood. However, the study by Johnston et al. [112]

indicated that only about 30% cardiac cycle was affected by the non-Newtonian model in the right coronary arteries. Thus, to simplify the CFD model, the assumption of Newtonian flow is widely accepted.

(3) Steady or pulsatile flow state

Due to systole and diastole cyclic behaviors, blood flow in all arteries presents pulsatile motion [70]. However, it was investigated that relatively small hemodynamic effects in the arteries [113, 114]. The fluid-structure interaction (FSI) between a stented artery and pulsatile blood flow is another discussion focus. The wall pulsation generated by the cyclic of the heart pump can activate FSI and change the computational fluid domain. Nevertheless, a study demonstrated only about 5% differences in TAWSS distribution by using full FSI analysis [115]. Thus, the assumption of a steady-state is reasonable, and the inlet velocity is defined as a time-averaged value over a cardiac cycle [65]. Besides that, due to the steady-state of blood flow, the outlet boundary condition in the CFD model is usually defined with constant pressure. As for a bifurcation model, a specified flow split ratio is defined at a bifurcation as the outlet conditions[116].

2.3.4 Stent optimization by CFD

In order to optimize coronary stents to minimize stent-introduced adverse flow changes, hemodynamically effects of stenting geometric characteristics have been widely studied. However, the development of related optimization design strategies is still very limited.

That is because the endovascular hemodynamic outcomes are under the effects of many different geometric features, resulting in a very complicated relationship between design variables and dynamic flow behaviors. However, to help understand the impacts of specific stenting characteristics on the hemodynamic changes, piece-wise considerations of strut geometric design features are usually adopted [64]. Thus, how to consider all the stenting geometric design variables on the blood flow behaviors simultaneously is still under development.

Similar to the methods used in stenting Topology optimization, most hemodynamic optimization research works also adopt different surrogate models as strategies to perform designs for stents. In the surrogate models, a response surface is created to establish the relationship between the objectives and the structural design variables, such as the thickness, width, angle, and spacing of stent struts. These optimization works can be approximately divided into three types:

1)   The single objective for the hemodynamic optimization model

The early hemodynamic optimization research works mainly focus on a single objective, such as minimizing low WSS areas [93, 117]. One of the basic strut features discussed above is usually defined as design variables in 2D or 3D models. Most of these studies share assumptions of rigid artery walls and steady-state blood flow. Some studies believed these assumptions mislead the optimization results. However, an investigation for the optimization with deformed artery walls and a pulsatile flow condition demonstrated that

the obtained outcomes are similar to the results of using steady flow with rigid walls [118].

2) Multi-disciplinary objectives for the design based on both structural analysis and CFD

The stent usually works in a complex endovascular environment involving structural mechanics and fluid dynamics [52]. Thus, some studies tried to perform the optimization for both aspects simultaneously [119, 120]. In the optimization models, design variables are the same as the regular used strut geometric features. The design objectives are defined based on mechanical and hemodynamic metrics, such as recoil, flexibility, and WSS. Moreover, additional objectives associated with drug release are sometimes also taken into account [119]. In the optimization, the mechanical objectives are evaluated by FEA, and the flow behaviors are obtained by CFD. Although the multi-disciplinary optimization strategy seems has a broad consideration for different physical design requirements, the fact is the optimization in respect of hemodynamic models still only adopts a single related objective and few structural design variables and cannot really capture the impacts of stenting geometric characteristics on the flow alterations in the arteries.

3) multi-objective for the hemodynamic optimization model

Some studies only focus on hemodynamic considerations to establish multi-objective optimization models, aiming to improve fluid behaviors around stents. The design

objectives are determined based on the hemodynamic metrics or relevant flow disturbances. Most of these studies adopt two optimization objectives: mean square WSS and mean swirl value [121], or the recirculation zone length and the struts reattachment distance [122]. Although these studies propose multi-objective models, they only define a few structural variables with limited improvements. Thus, some researchers attempt to include more strut geometric characteristics and more design objectives into optimization models [71] but facing two issues. The first problem is that a large number of design variables and design objectives lead to complicating optimization models significantly, and results may not converge. Another problem is most current works adopt surrogate optimization models, which are strongly dependent on the initial designs. They cannot achieve new topologies of stents, and the improvements are still in a limited range.

2.4 Topology optimization

Structural optimization is a subject for improving the performances via the alterations of structural parameters, involving the optimizations for size, shape, and topology. Among these, size and shape optimizations are dependent on the initial structures. Topology optimization is a numerical procedure that can iteratively re-distribute the material in a prescribed design domain under the given constraints and objective functions. Thus, topology optimization can get rid of the limitations of the initial structural characteristics. On the other hand, topology optimization belongs to a kind of conceptual design, strongly affecting the final design of the structure but facing more challenges as well. In 1988,

Bendsøe and Kikuchi [123] proposed the topology optimization method based on the homogenization theory. After that, topology optimization is rapidly developed in the following few decades, resulting in a wide range of applications in various fields, such as mechanical, biomechanical, fluid, aerospace, composite, etc. So far, several topology optimization approaches have been developed, including the Solid Isotropic Material with Penalization (SIMP) method [124, 125], the evolutionary structural optimization (ESO) method [126], the level set method (LSM) [127-129], the phase field method [130, 131], and the Moving Morphable Components (MMC) method [132, 133].

2.4.1 Topology optimization methods

Topology optimization for continuum structures is a kind of discretized optimization problem with the discrete design variables 0 or 1, where 0 and 1 denote void holes and solid materials, respectively. The computational cost significantly increases when dealing with large scale optimization problems. In order to apply efficient gradient-based algorithms in topology optimization, material description models are first employed to relax the discrete design variables to a continuous range from 0 to 1, such as the homogenization method and SIMP method. On the other hand, boundary description models embed the topological changes into continuous motions of the boundary. Thus, methods such as the LSM can utilize gradient-based algorithms to update the design variables iteratively.

1) Homogenization method

The homogenization theory comes from the composites field, believing macroscopic structures comprised of numerous periodic microstructures. It can evaluate the effective macroscopic properties of composites based on the microstructures [134]. Based on the theory, the effective macroscopic properties of the composites are determined by the periodic microstructures. In 1988, Bendsøe and Kikuchi proposed a homogenization-based methodology to realize topology optimization by changing the geometric features of the microstructures, such as the size and orientations [123]. After that, Suzuki and Kikuchi performed the shape and topology optimizations using the homogenization method [135]. Then, based on the homogenization method, the optimization for the structures with multiple loading conditions was realized by Díaaz and Kikuchi [136].

The homogenization method relaxes the discrete topology optimization problems to continuous size optimization of the microstructures. The existence and uniqueness of the optimization based on the homogenization method can be rigorously demonstrated [137]. However, the homogenization-based topology optimization method generates a large number of design variables that may lead to large computational cost.

2) SIMP method

As extended from the homogenization method, the SIMP method was developed by Bendsøe and Sigmund [124, 125]. It establishes a material interpolation model to associate the material properties, such as Young's modulus, to the introduced artificial element densities, which can continuously adopt the value from 0 to 1. Thus, the SIMP

method can relax the discrete problem to a continuous optimization problem in an easy way via the material interpolation model, experiencing great popularity. On the other hand, the SIMP method introduces a penalization mechanism based on a power-law criterion to converge the intermediate element density close to binary 0 or 1. However, the existence of intermediate elements density induces some numerical instability issues, such as mesh dependence, checkerboards, and local minima [138, 139]. Then, some numerical techniques were integrated into the SIMP method to reduce the instabilities, such as perimeter control and different filtering methods [139]. Due to the easiness of the numerical implementation, the SIMP method has been widely applied to various fields and also integrated into some commercial software, like ANSYS, HyperWorks, and Solid Works.

3) ESO method

The ESO method was developed in 1993 by Xie and Steven [126]. It retains the binary discrete design variables (0, 1) in the topology optimization problems without relaxation, adopting 0 as voids and 1 as the solid material. When performing optimization, the ESO method evaluates the element contributions on the assumed proper criteria and removes the element with contributions lower than the specified value. However, the ESO method easily leads to local minimal via this hard-killing manner. After that, Huang and Xie [140, 141] developed a bi-directional evolutionary structural optimization (BESO) method. It not only removes the elements with lower contributions but also has a mechanism to add

elements. The ESO/BESO method also has a wide range of applications due to the intuitive numerical implementations but has to introduce relaxation for design variables to extend the applications.

4) Level set method

The level set method (LSM) is developed initially to track and simulate the evolutions of moving boundaries and shape numerically [142]. In the LSM, the moving boundaries are implicitly presented as the zero-level set of a higher-dimensional level set function. Thus, the evolution of the boundaries can be described by the partial differential equation (PDE) of the level set function in a Eulerian system. Sethian and Wiegmann introduced the LSM to describe the structural boundaries and realized topology optimization for the structure by evolving the zero level set of the function [127]. Then, Osher and Santosa introduced the LSM to study frequency optimization problems [143]. After that, Wang et al. [128] developed a level set topology optimization method combining shape derivatives [144]. In this method, the derived first-order Hamilton-Jacobi PDE (H-J PDE) associates the normal velocity fields of the structural boundaries with the shape derivatives. Hence, the structural boundaries can be obtained by solving the H-J PDE. Short later, Wang and Wang [145] developed a 'color' level set model to realize multi-material optimization. Allaire et al. [129] proposed an LSM based on the shape sensitivity analysis and the front propagation technologies, and the velocities in the method are rigorously derived from the shape derivatives.

The optimization based on the LSM can simultaneously describe the topological and shape variations by utilizing level set function to driving the motion of the structural boundaries. Therefore, the optimized results are of smooth and clear structural boundaries. However, as for the conventional LSM, some numerical difficulties in solving H-J PDE complex the implementation. The first issue is that the optimization result is highly dependent on the initial guess. The second issue is that the Courant–Friedrichs–Lewy (CFL) condition requires a sufficiently small time step to ensure the numerical stability when using the finite difference method to solving the H-J PDE [146], leading to a significant increase in the computational cost. The other issue is that re-initialization for the signed distance function is suggested to maintain the numerical accuracy. Besides that, the normal velocity field should be extended to the neighborhood of the structural boundaries or the whole design domain [129, 146]. Hence, many improved LSMs have been developed to overcome these numerical issues. Among that, the parametric level set method (PLSM), as an efficient alternative LSM for topology optimization, was proposed by Luo et al. [147, 148]. In the PLSM, the Compactly Supported Radial Basis Functions (CSRBFs) is utilized to interpolate the level set function. Thus, the evolution of the related expansion coefficients in the proposed interpolation advances the level set function. In this way, the H-J PDE is transformed as an ordinary differential equation (ODE), and the numerical difficulties in conventional LSMs are circumvented. Additionally, many well-established efficient optimization algorithms can be directly applied in PLSM, such as

the optimality criteria (OC) and the method of moving asymptotes (MMA).

2.4.2 Topological design of microstructural metamaterials

Metamaterials are a kind of man-made composites with periodic microstructures, exhibiting unconventional properties, such as negative Poisson's ratios, negative bulk modulus, negative thermal expansion coefficient, and negative permittivity. Due to the great potential of the functional metamaterials applied in different fields, the related structural optimization designs experience great popularity [149-152]. The artificial metamaterials belong to multifunctional cellular composites [153, 154]. The effective properties of these cellular composites can be designed by changing their microstructures [155]. In particular, for the periodic cellular composites, it is more efficient to design their effective properties due to the identical microstructures.

As discussed, the homogenization method provides an efficient way to evaluate the effective macroscopic properties of composites [134]. The obtained effective properties are essentially determined by the material layouts of the periodic microstructures. Sigmund [149] developed an inverse homogenization method to achieve desired effective properties by optimizing the microstructures. The method combined the homogenization theory with topology optimization. After that, the design of material microstructures has been widely studied. Among these, the developed numerical homogenization method is accepted as an efficient numerical implementation to evaluate the effective properties of cellular composites and has been commonly applied in different topology optimization

methods to realize the material design [156-164]. Sigmund and Torquato [156] designed the material with extreme thermal expansion. Guest and Prévost [157] established a multiphysics model to design a composite with maximum elastic bulk modulus and fluid permeability. Zhang and et al. [158] developed an alternative strain energy-based method to evaluate the effective properties of cellular composites. Diaz and Sigmund [159] designed the metamaterials with negative permeability. Radman et al. [161] combined the BESO method to perform the design of isotropic cellular materials. Andreassen et al. [162] studied the design of 3D microstructures with extremal elastic properties. Wang et al. [163] applied an LSM to the optimization design of metamaterials. Li et al. [164] designed a metamaterial with auxetics by functionally graded cellular composites. The developments of the multifunctional cellular composites significantly create a large number of artificial metamaterials with different unusual properties.

The studies about artificial cellular composites extend the applications of topology optimization. After that, the structural topology optimization is not limited to the macroscopic topological alterations to enhance mechanical performances. The material layout of the periodic microstructures can also become the design objective. The topological optimization for artificial microstructures is flexible in tailoring effective extremal properties of the macroscopic structures. Thus, a wide range of unusual properties can be obtained, such as metamaterials with negative properties and the composites with ultralightweight but high performances. Moreover, the coronary artery

stents consist of periodic unit cells and can be regarded as artificial composites. Hence, the advanced optimization design method for multifunctional cellular composites can be applied in the stenting designs to benefit their performances.

2.5 Auxetic metamaterials

Auxetics belong to mechanical metamaterials consisting of artificial microstructures exhibiting unusual elasticity property, namely, negative Poisson's ratio (NPR) [165, 166]. Auxetics contract or expand in a transverse direction when compressed or stretched in an axial direction. Auxetics provide the potential for a wide range of applications in different fields due to their unique properties for energy absorption, anti-impact, indentation resistance, thermal isolation, and fracture toughness.

Based on the deformation mechanism, the auxetic metamaterials can be divided into three different types: re-entrant [167, 168], chiral [169-171], and rotating [172]. In the early period, the design of auxetics was mainly obtained based on mathematical optimization and experiments, leading to a limited range of the auxetic structural configurations. The auxetic property belongs to a macroscopic deformation behavior of the structure and can be derived from the material elastic properties. With the development of the design of multifunctional cellular composites, the auxetic design has been rapidly developed. Thus, the structure with effective macroscopic auxetic properties can be achieved by the optimization design of microstructures. The early study about the topology optimization

for auxetics can be found in [160], obtaining a 3D microstructure with auxetics. Then, 2D auxetic metamaterials were designed based on different topology optimization methods [173-175]. The application of an LSM in the material design of auxetics can be found in [163]. On the other hand, the design of Poisson's ratios involving nonlinear and over large deformations were investigated [176-178]. Zong et al. [179] proposed a two-step design strategy to perform material design for Poisson's ratios and refine the structural boundaries, respectively. However, the 3D auxetic metamaterials design is still facing challenges due to significant high computational cost, where more efficient design approaches are necessary. The drawback of the auxetics is that the structure contains many pores leading to a decrease of stiffness. However, that limitation can actually benefit coronary stent designs to obtain good flexibility. Moreover, the usual NPR deformation mechanism of auxetics can improve stenting performances. All the improvements of auxetics to the stenting structures will be discussed in Chapter 4.

2.6 Summary for the literature review and the research gaps

In summary, the development of BMS provides an efficient way to treat CAD. After that, the occurrence of complications ST and ISR after stent implantation promotes the development of DES. Although the antiproliferative drugs released by DES significantly reduce the incidence of ISR, the polymer coatings used for carrying drugs cause an increase risk in late ST. That promotes the development of BVS. However, due to the limitations of the material properties, BVS is still under the study. In respect of expansion

mechanism, SE stents present better mechanical performances than BE stents, but more complicate in use due to the deliverability and high precise size requirements.

On the other hand, as the developments of stents, the stent mechanical failures and the induced adverse hemodynamic changes rase more and more concerns for researchers to focus on the relationships between stent structures and the complications. However, the relevant structural optimizations are still facing some problems. The first problem is most current optimization strategies are strongly dependent on the initial designs, they cannot achieve new topologies of stents and the improvements are still limited. Another problem is that these strategies are hard to consider all the stenting structural features, because a large number of design variables and design objectives lead to complicating optimization models significantly, and results may not converge.

In order to overcome above limitations of the current stent optimization strategies, this project introduces level set based topology optimization method into stent designs. In the respect of stent mechanical performances, the design of auxetic metamaterials overcome the drawbacks of SE stents and enhance the mechanical properties. In the respect of stent induced adverse hemodynamic changes, the proposed MFP associates all the stent structural features to a single design objective, and significantly reduces the amount of design variables and optimization objectives.

Chapter 3 Extended parametric level set method (X-PLSM)

Topology optimization with LSM can perform topology and shape optimization simultaneously by evolving the structural boundaries [127-129]. The PLSM is proposed to overcome the numerical difficulties in conventional LSM. In PLSM, the level set function is interpolated by the CSRBFs, which leads to the level set function only spatial dependent. Thus, it converts the H-J PDE to an equivalent ODE, significantly simplifying the LSM. An extended parametric level set method (X-PLSM) is proposed in this chapter to perform the topology optimization design for coronary stents efficiently. The X-PLSM transforms the 2D PLSM from the Cartesian system into a curvilinear coordinate system. Based on X-PLSM, the optimization for coronary stents can accurately and efficiently achieve the results by adopting shell elements.

3.1 Conventional Level set method (LSM)

3.1.1 Boundary representation

The level set method adopts an implicit description to embed the design boundaries of the structure into the zero-level set of a higher-dimensional level set function. A 2D example of the representation based on the LSM is illustrated in Figure 3-1. D is a reference domain. Ω is the structural shape, and $\partial\Omega$ is the structural boundary associated with the zero-level set. A 3D level set function $\Phi(x)$ is defined over the reference domain and can

be formulated as the following:

$$
\begin{cases}
\mathbf{\Phi}(\mathbf{x}) > 0 & \mathbf{x} \in \varOmega \setminus \partial\varOmega & (\text{Solid}) \\
\mathbf{\Phi}(\mathbf{x}) = 0 & \mathbf{x} \in \partial\varOmega & (\text{Boundary}) \\
\mathbf{\Phi}(\mathbf{x}) < 0 & \mathbf{x} \in D \setminus (\varOmega \bigcup \partial\varOmega) & (\text{Void})
\end{cases}
\tag{3-1}
$$

where *x* is the point in the space. *D*. *Ω* and *∂Ω* denote the design domain and the boundary, respectively.

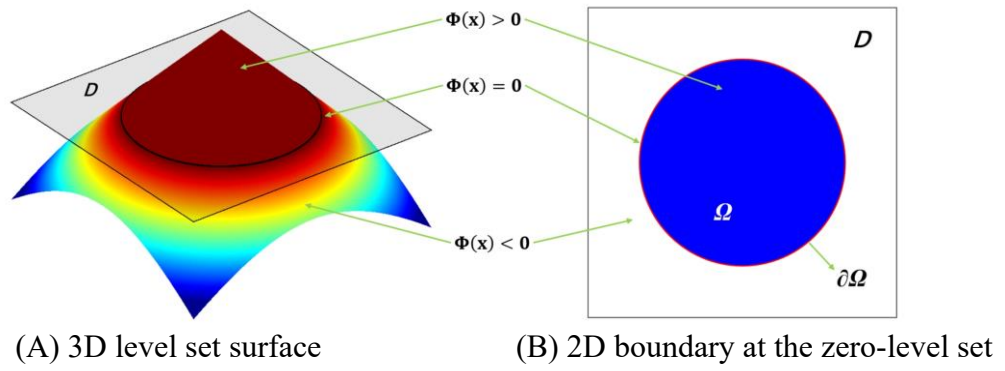(A) 3D level set surface   (B) 2D boundary at the zero-level set

Figure 3-1 A 2D boundary representation by 3D level set surface

3.1.2 Hamilton-Jacobi equation

The example in Figure 3-1 shows that the structural boundary is represented as the zero level set of the level set function. The shape of the boundary can be changed by the motion of the level set surface along the direction normal to the reference domain. In the conventional LSM, the evolution of the level set function is driven by the Hamilton-Jacobi equation, which can be numerically solved by the finite difference method [146]. The motion of the structural boundary can be enabled by introducing the pseudo-time *t* into the level set function. Thus, by differentiating the level set function at the zero level

set with respect to *t*, the H-J PDE can be obtained:

$$\frac{\partial \mathbf{\Phi}(\mathbf{x},t)}{\partial t} + \mathbf{v} \cdot \nabla \mathbf{\Phi}(\mathbf{x},t) = 0 \tag{3-2}$$

where **v** is the velocity field and given by:

$$\mathbf{v} = \frac{d\mathbf{x}}{dt} \tag{3-3}$$

The velocity field **v** has two components long the normal and tangent directions, where only the normal velocity field drives the alteration of the boundary shape. Thus, the boundary motion along the normal direction is equivalent to evolving the level set function based on H-J PDE solutions. The Eq. (3-2) is transformed as:

$$\frac{\partial \mathbf{\Phi}(\mathbf{x},t)}{\partial t} - v_n \cdot \nabla \mathbf{\Phi}(\mathbf{x},t) = 0 \tag{3-4}$$

where the normal velocity v_n along the normal direction **n** is given by:

$$v_n = \mathbf{v} \cdot \mathbf{n} = \frac{d\mathbf{x}}{dt} \cdot \left(-\frac{\nabla \mathbf{\Phi}}{|\nabla \mathbf{\Phi}|} \right) \tag{3-5}$$

In conventional LSM, it usually adopts the finite difference method to solving the H-J PDE but facing the restriction of the CFL condition, resulting in a sufficiently small time step to ensure numerical stability. Besides that, the re-initialization and the extension of the boundary velocity field are also necessary for maintaining numerical stability and accuracy. Therefore, all these strict requirements for the conventional LSM significantly difficult the numerical implementation and hamper the development.

3.2 Parametric level set method (PLSM)

PLSM [147, 148] is an efficient alternative method for conventional LSM to circumvent the discussed numerical difficulties. In the PLSM, the level set function is interpolated by the CSRBFs. It successfully decouples the time and space in the level set function, leading to the level set function only spatial dependent. In this way, the H-J PDE is transformed as an ordinary differential equation (ODE), driven by the related expansion coefficients. Moreover, many well-established gradient-based optimization algorithms can be directly applied in PLSM.

3.2.1 Compactly supported radial basis functions (CSRBFs)

Radial basis functions (RBFs) belong to real-valued functions and are calculated based on the distance to the specific point. RBFs can efficiently approximate complicated scalar functions. Different RBFs as the interpolation functions can maintain the requirements of various problems. Two types of RBF have sparse interpolation matrix: globally supported RBFs (GSRBFs) and compactly supported RBFs (CSRBFs). Both RBFs have been adopted to interpolate the level set function to circumvent H-J PDE solving. Wang and Wang [180] introduced GSRBFs into LSM. The LSM with GSRBFs successfully transformed the H-J PDE but difficult the calculations due to the full density matrix. In contrast, CSRBFs with more efficiency are of strictly positive definite property and matrix sparseness. An example of the basis function in CSRBF is shown in Figure 3-2. From the figure, we can see the supported domain of knot *i* is shown as the red circle with
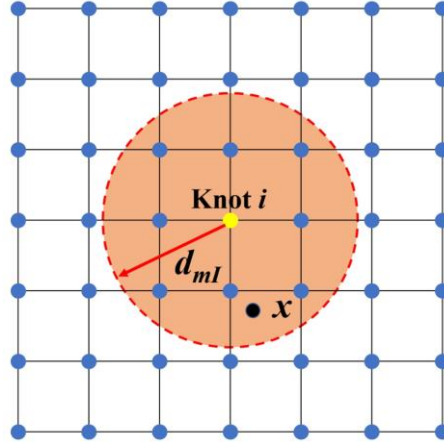
the defined radius d_{mI} in the CSRBF.

Figure 3-2 Supported domain of knot *i* with radius d_{mI}

In PLSM, CSRBFs are adopted to interpolate the level set function, improving optimization efficiency [181]. CSRBFs with various continuity orders, such as C2, C4, and C6, were investigated in [182]. The CSRBFs of the ith knot used with C2, C4, C6 continuities are given as:

$$C2: \phi_i(x) = max\left\{0, 1 - r_i(x)\right\}^4 \left(4r_i(x) + 1\right) \quad (i = 1, 2, ..., N) \tag{3-6}$$

$$C4: \phi_i(x) = max\left\{0, 1 - r_i(x)\right\}^6 \left(35r_i^2(x) + 18r_i(x) + 3\right) \quad (i = 1, 2, ..., N) \tag{3-7}$$

$$C6: \phi_i(x) = max\left\{0, 1 - r_i(x)\right\}^8 \left(32r_i^3(x) + 25r_i^2(x) + 8r_i(x) + 1\right) \quad (i = 1, 2, ..., N) \tag{3-8}$$

$r_i(x)$ is defined as:

$$r_i(x) = d_I / d_{mI} = \sqrt{(x - x_i)^2 + (y - y_i)^2} \Big/ d_{mI} \tag{3-9}$$

where d_I denotes the distance between the current sample knot (x, y) and the ith knot (x_i, y_i), and d_{mI} is the influence domain of the knot (x, y), which means only the knots in that domain can affect the current CSRBFs function. Thus, d_{mI} should not be too large to

increase the calculation or too small to cause singularities [182]. The shapes of CSRBF with C2, C4, and C6 are presented in Figure 3-3. All three functions exhibit good differentiability, where CSRBFs-C6 with the steepest caps of shape and derivatives showing the highest differentiability. CSRBFs with C6 continuity may be more sensitive to the changes of the support domain size but may also lead to a higher computational cost than others with the same support domain size. Hence, the PLSM usually adopts the CSRBFs with C2 continuity.
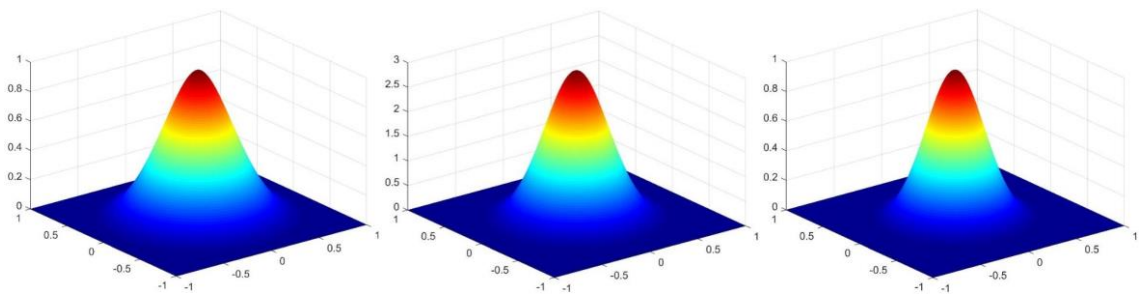
(A) Shape of CSRBFs-C2   (B) Shape of CSRBFs-C4   (C) Shape of CSRBFs-C6

Figure 3-3 A 2D boundary representation by 3D level set surface

3.2.2 Parameterization of the level set function

In the conventional level set method, the optimization process is described as the dynamic motion of the level set function $\Phi(x)$. By introducing a pseudo time t, this dynamic change can be determined by the H-J PDE Eq. (3-2). Thus, the optimization is transferred into a procedure to find an appropriate velocity field v_n to solve the Hamilton–Jacobi PDE. Within the PLSM, the level set function is calculated through centrally positioning CSRBFs-C2 at a set of given knots over the whole design domain. That interpolation method is as follows:

$$\Phi(x,t) = \varphi(x)^T \alpha(t) = \sum_{i=1}^{N} \varphi(x) \alpha_i(t) \tag{3-10}$$

where N is the number of fixed knots in the design domain. The CSRBFs of the ith knot used with C2 continuity is given in Eq. (3-6). The vector with the CSRBFs functions is:

$$\varphi(x) = \left[\phi_1(x), \phi_2(x), \ldots, \phi_N(x) \right]^T \tag{3-11}$$

and the expansion coefficient vector is given by

$$\alpha(t) = \left[\alpha_1(t), \alpha_2(t), \ldots, \alpha_N(t) \right]^T \tag{3-12}$$

Since all the RBF knots are fixed in the design domain, this interpolation decoupled the time and space in the level set function. Thus, the original level set function $\Phi(x,t)$ is now determined by the spatial functions $\varphi(x)$ located at the knots, and the temporal only expansion coefficient $\alpha(t)$. The H-J PDE is transformed into the following ODE system:

$$\varphi(X)^T \dot{\alpha}(t) - v_n \left| (\nabla\varphi)^T \alpha(t) \right| = 0 \tag{3-13}$$

Hence, the normal velocity field is given as:

$$v_n = \frac{\varphi(X)^T}{\left| (\nabla\varphi)^T \alpha(t) \right|} \dot{\alpha}(t), \quad \text{where } \dot{\alpha}(t) = \frac{d\alpha(t)}{dt} \tag{3-14}$$

3.3 Extended parametric level set method (X-PLSM)

The numerical implementation method based on zero iso-contour used in the level set method can be utilized to solve a curved shell model, but it has a higher computational cost. The H-J PDE in Eq. (3-2) can also be described as Eq. (3-15), where the local velocity v can be calculated by three components in the Cartesian coordinates.

$$\frac{\partial \Phi(x,t)}{\partial t} - v \cdot \nabla \Phi(x,t) = 0, \quad \text{where} \quad v \equiv \frac{\partial x}{\partial t} = \left[v_x, \, v_y, \, v_z \right] \tag{3-15}$$

Hence, if the velocity components are transferred in curvilinear coordinates, the evolution of the level set function can also be described with curvilinear coordinates. As an illustration in Figure 3-4, the blue color shows a level set function. The white intersection line is the boundary of a four-node shell structure located at the zero-level set, presented as the red curved surface.
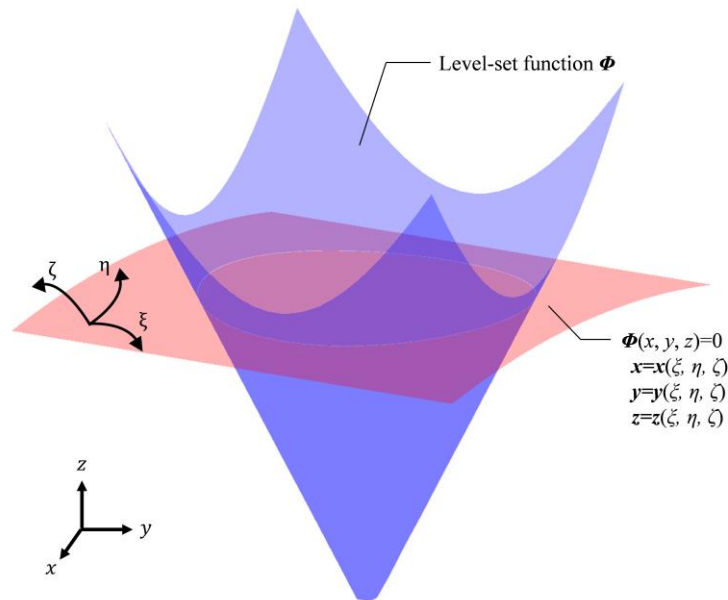

Figure 3-4 Level set function in curvilinear coordinates

Initially, this kind of transformation rule was used to deal with fluid issues [183, 184]. Then Park and Youn [185] introduced this transformation into level-set topology optimization. Based on the above works, the transformation of the level set function from Cartesian coordinates to curvilinear coordinates can be described as:

$$\frac{\partial \Phi}{\partial t}+\frac{1}{J}\frac{\partial}{\partial \xi^j}\left(\frac{J}{\sqrt{g_{jj}}}\Phi v_\xi^j\right)=0 \quad (j=1,\,2,\,3), \text{ where } \sqrt{g_{jj}}=\sqrt{g_j \cdot g_j} \tag{3-16}$$

where, $J=\det(J)$, and J is the Jacobian matrix; g_j is the covariant basis vector in curvilinear coordinates $\xi^j(\xi,\eta,\zeta)$, and v_ξ^j is the velocity component in the ξ^j-coordinate direction.

Then, we propose an extended PLSM (X-PLSM) by applying this transformation rule into the PLSM based on CSRBFs. Since the time-derivative is only related to the expansion coefficient $\alpha(t)$ in PLSM, the transformation can be applied only for the spatial functions $\varphi(x)$, as shown in Eq. (3-17), where the subscript ξ donates parameters in the curvilinear coordinates $\xi^j(\xi,\eta,\zeta)$, and $\varphi_\xi(\xi)$ is the transformed spatial functions.

$$\Phi_\xi(\xi,t)=\varphi_\xi(\xi)^T \alpha_\xi(t)=\sum_{i=1}^{N}\varphi_\xi(\xi)\alpha_{\xi,i}(t) \tag{3-17}$$

The level set model in Eq. (3-13) can then be rewritten in the curvilinear coordinates, as Eq. (3-18).

$$\varphi_\xi(\xi)^T \dot{\alpha}_\xi(t)-v_\xi^n\left|(\nabla\varphi_\xi)^T \alpha_\xi(t)\right|=0 \tag{3-18}$$

where, v_ξ^n is the normal velocity field in the curvilinear coordinates, and can be given by:

$$v_\xi^n=\frac{\varphi_\xi(\xi)^T}{\left|(\nabla\varphi_\xi)^T \alpha_\xi(t)\right|}\dot{\alpha}_\xi(t), \quad \text{where } \dot{\alpha}_\xi(t)=\frac{d\alpha_\xi(t)}{dt} \tag{3-19}$$

The X-PLSM is much more efficient than normal PLSM when addressing the issues of shell models. For example, as for a shell geometry, the 3D PLSM should be used to establish the optimization model. In the model, one element has eight nodes, and one node

has three degree of freedoms. By using X-PLSM, as for the same shell geometry, in the established optimization model, one element has four nodes, and each node has three degree of freedoms. Thus, the scale of the FEA model establish by X-PLSM is 1/4 of the normal PLSM. Besides that, the description of the zero-level set for this shell model in X-PLSM is via a curved surface, while the description of the zero-level set for the same model in normal PLSM should use a three-dimensional isosurface. That also shows the efficiency of the X-PLSM.

3.4 Conclusion

In this chapter, the conventional LSM is discussed. In order to overcome the numerical difficulties in the LSM, the PLSM adopt CSRBFs to interpolate the level set function. It successfully separates the time and space from the level set function and transforms the H-J PDE into an ODE system. Thus, the PLSM circumvents the numerical difficulties in conventional LSM and significantly improves the LSM. However, no matter for LSM or PLSM, it cannot efficiently solve a curved shell model. As for the interpolation used in PLSM, the CSRBFs drive the approximation to the level set function. Hence, the X-PLSM is developed to transform the CSRBFs from the Cartesian system to a curvilinear system, resulting in a level set function interpolated in the curvilinear system. By using X-PLSM, we can adopt curved shell elements to solve the stents model more efficiently and accurately.

Chapter 4 Topology optimization of auxetic stents considering structural performance

This chapter is mainly based on our published research work: ***Design of Self-Expanding Auxetic Stents Using Topology Optimization***. It has been published in ***Frontiers in Bioengineering and Biotechnology, 2020. 8: p. 736***.

In this chapter, we will develop a more effective systematic design method to find new stenting structures for the future generation of SE stents to improve stent performance by optimizing the stenting structure of topology and shape. The new designs for stenting structural architectures will eventually improve stent safety to low the incidence of ISR and ST. Hence, to help overcome the above drawbacks in current SE stents, this chapter will firstly introduce the auxetic microstructures into SE stents to achieve closed-cell stents, and then develop an enhanced topological optimization method with X-PLSM, which is more accurate and more efficient in finding the best architecture for auxetic microstructures.

Topology optimization has been a popular option to realize the optimization of shape and topology of geometries, because it is a numerical procedure that can iteratively find the best material distribution in the design domain. Few studies have attempted to introduce topology optimization into the design of stents, such as [63], but the topology optimization was only used for a bi-stable design during the expansion of the stent to eliminate the axial displacement. There has been no previous work that systematically integrates topology optimization with auxetics to develop auxetic SE stents, and no work

has employed a multiscale concurrent topology optimization method to create novel stenting structures. Hence, topology optimization can find the optimized performance of stenting structures, associated with the best material layout and the most efficient material usage in the design. Particularly, the concurrent multiscale topology optimization method, with X-PLSM and the numerical homogenization method, can systematically integrate the NPR mechanical metamaterials into the SE stent to implement a new mechanism for expanding by entirely making use of the auxetic behavior of microstructures. The topologically designed, micro-structured, multiscale cellular composite structure is characterized by small size, large expansion, uniform radial force, and super compliance, helping avoid the injury to vessel surface, edge-dissection, and side-branch, resulting in low ST and ISR.

Auxetics will mainly benefit the SE stents from the following aspects:

(1) Auxetic behavior can help make the size of SE stents much smaller than the current profile of SE stents. Small profiles of SE stent systems will facilitate deliverability and reduce the occurrence of complications due to potential injury in the PCI process. After implantation, they fully stretched themselves and adaptively fit the vessel wall.

(2) The effective NPR property of auxetic microstructures makes SE stents have non-shortening that facilitates accurate sent deployment when deployed, which further reduces stent malapposition. As we know, stent implantation often leads to suboptimal results, e.g., the occurrence of strut malapposition, especially in cases of complex lesions and other factors. The indentation resistance of auxetics enables a superior conformability of stent struts to automatically match the vessel wall surface, allowing the stent to contact the vessel surface perfectly without malapposition.

(3) The auxetic microstructures can adaptively respond to different radial compressive forces, making the auxetic stent have variable hoop strengths that allow the stent to adapt complex shapes such as tortuous and clogged arteries easily. In response to large artery size and small radial force, the auxetic stent will automatically change its shape, and it will continuously expand outwardly and reduce its radial resistance force to avoid malapposition. Otherwise, when the auxetic stent subject to a small artery size and large hooping force, the stent will increase its structural stiffness and strength (due to indentation resistance) to withstand an increased radial compressive force applied to the stent from the vessel. The adaptive stiffness and strength provided by the auxetic stents will help reduce the risk of ST and ISR.

(4) The auxetics can also improve stenting mechanical performance and reduce the happening of stent fracture and enhance their ability to withstand fatigue and vibration, because the NPR property can greatly improve the fracture toughness of structures. This will also benefit a low incidence of restenosis.

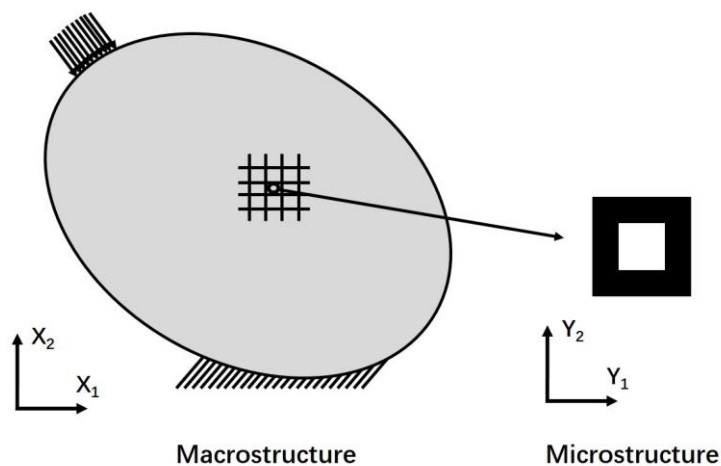## 4.1 Numerical homogenization method

Figure 4-1 An illustration of homogenization

The homogenization [123, 186] technique assumes that the design domain consists of a periodic configuration of unit cells, which are much smaller than the bulk material in size. A simple example about homogenization is illustrated in Figure 4-1. Based on that concept, in this optimization work, the numerical homogenization method will be used to roughly estimate the effective properties of the microstructures. For instance, the effective elasticity tensor D_{ijkl}^{H} can be calculated by:

$$D_{ijkl}^{H} = \frac{1}{|\Omega|} \int_{\Omega} \left(\varepsilon_{pq}^{0(ij)} - \varepsilon_{pq}^{*(ij)} \right) D_{pqrs} \left(\varepsilon_{rs}^{0(kl)} - \varepsilon_{rs}^{*(kl)} \right) d\Omega \qquad (4\text{-}1)$$

where i, j, k, l and p, q, r, s are all used to denote 1, 2. Ω is the design domain; $|\Omega|$ is the area of the design domain; D_{pqrs} is the elasticity tensor of the base material; $\varepsilon_{pq}^{0(ij)}$ is the test unit strain field, where $(1,0,0)^T$, $(0,1,0)^T$ and $(0,0,1)^T$ are used in two-dimensional cases; $\varepsilon_{pq}^{*(ij)}$ is the locally varying strain field due to the application of the unit strain field, which is defined by:

$$\varepsilon_{pq}^{*(ij)} = \varepsilon_{pq}^{*} \left(u^{(ij)} \right) = \frac{1}{2} \left(u_{p,q}^{(ij)} + u_{q,p}^{(ij)} \right) \qquad (4\text{-}2)$$

By using the finite element method with periodic boundary conditions, the displacement field $u^{(ij)}$ can be calculated by:

$$\int_{\Omega} \left(\varepsilon_{pq}^{0(ij)} - \varepsilon_{pq}^{*} \left(u^{(ij)} \right) \right) D_{pqrs} \varepsilon_{rs}^{*} \left(v^{(kl)} \right) d\Omega = 0, \ \forall v^{(kl)} \in \bar{U} \left(\Omega \right) \qquad (4\text{-}3)$$

where $v^{(kl)}$ is the virtual displacement field in $\bar{U}(\Omega)$, which denotes the space of all the kinematically admissible displacements in the design domain Ω.

4.2 Shell elements

Most stenting structures can be regarded as thin-walled structures. The thickness of most stents is around 100 μm, much smaller than sizes of width and length that are usually 4 and 10 mm, respectively. Therefore, the shell element is more suitable for approximating structures of stents. A shear deformable shell element with four nodes is used in this optimization model. Each element has four nodes, and each node has three degrees of freedom w_i, θ_{xi}, and θ_{yi}, as shown in Eq. (4-4). This kind of element is more convenient and accurate to capture the deformation of the thin-walled stenting structure. When performing FEA, the element stiffness matrix is assembled by two parts, as illustrated in Eq. (4-5): bending loads calculated by elasticity tensor D_b and shear deformation calculated by D_s.

$$q_i = \begin{bmatrix} w_i & \theta_{xi} & \theta_{yi} \end{bmatrix}^T, \quad \text{where } \theta_{xi} = \frac{\partial w_i}{\partial y} \text{ and } \theta_{xi} = -\frac{\partial w_i}{\partial x} \tag{4-4}$$

$$[D_b] = \frac{Eh^3}{12(1-\mu^2)} \begin{bmatrix} 1 & \mu & 0 \\ \mu & 1 & 0 \\ 0 & 0 & (1-\mu)/2 \end{bmatrix}, \text{ and } [D_s] = kh \begin{bmatrix} G & 0 \\ 0 & G \end{bmatrix} \tag{4-5}$$

where E and G are Young's modulus and shear modulus, respectively. μ is Poisson's ratio. k is the shear energy correction factor, and h is the thickness of the shell element.

4.3 Optimization model and sensitivity analysis

In this optimization design, the objective of the design is to obtain a structure with both auxetic behavior and the stiffness to support artery walls. Therefore, a concurrent topology optimization strategy is used to design the auxetic structure in the microscale

and meet the compliance requirement in the macroscale. Since the structure of a stent should be composed of periodic unit cells in a scale that is much bigger than the real microscale, the concept of multiscale in this optimization is a kind of heuristic model. In this heuristic multiscale model, the auxetic property is still obtained in a microscale, but the macrostructure is periodically composed of auxetic microstructures. The realization and relevant sensitivity analysis will be discussed in this section.

4.3.1 Optimization model

Initially, the effective elasticity tensor of the microstructure is firstly calculated, and then the Poisson's ratio is evaluated based on the effective elasticity tensor. Then, the objectives in macro and micro scales are calculated, respectively. After that, they are normalized and assembled by weight factors. Meanwhile, the final sensitivity of multiscale is obtained in the same way. Finally, X-PLSM is used to update the interpolation coefficients and so the structural shape and topology. In this optimization, the macrostructures are configured by a series of uniform microstructures. The overall concurrent topology optimization using X-PLSM is formulated as:

$$
\begin{cases}
Find \quad \alpha_{\xi,n}^{MI}\left(n=1,2,\ldots,N\right) \\
Min \quad J\left(\alpha_{\xi}^{MI}\right)=W_1 J^{MA}\left(\alpha_{\xi}^{MI}\right)+W_2 J^{MI}\left(\alpha_{\xi}^{MI}\right) \\
\qquad =W_1\left(\frac{1}{2}\int_{\Omega_{\xi}^{MA}}\left(u_{\xi}^{MA}\right)^T K_{\xi}^{MA}\left(D_{ijkl}^H\left(D_{ijkl}^{bH}\left(\alpha_{\xi}^{MI}\right),D_s\right)\right)u_{\xi}^{MA}d\Omega_{\xi}^{MA}\right) \\
\qquad +W_2\left(\left(\mu_1\left(D_{ijkl}^{bH}\left(\alpha_{\xi}^{MI}\right)\right)+1\right)^2+\left(\mu_2\left(D_{ijkl}^{bH}\left(\alpha_{\xi}^{MI}\right)\right)+1\right)^2\right) \\
S.t. \quad V\left(\alpha_{\xi}^{MI}\right)=\int_{\Omega_{\xi}^{MI}}H\left(\Phi_{\xi}^{MI}\left(\alpha_{\xi}^{MI}\right)\right)d\Omega_{\xi}^{MI}-V_{\xi}^{max}\le 0 \\
\qquad F_{\xi}^{MI}\left(u_{\xi}^{MI},w_{\xi}^{MI},\alpha_{\xi}^{MI}\right)=L_{\xi}^{MI}\left(w_{\xi}^{MI},\alpha_{\xi}^{MI}\right),\forall w_{\xi}^{MI}\in\overline{U}\left(\Omega_{\xi}^{MI}\right) \\
\qquad F_{\xi}^{MA}\left(u_{\xi}^{MA},w_{\xi}^{MA},D_{ijkl}^H\right)=L_{\xi}^{MA}\left(w_{\xi}^{MA}\right),\forall w_{\xi}^{MA}\in\overline{U}\left(\Omega_{\xi}^{MA}\right) \\
\qquad \alpha_{\xi,min}^{MI}\le\alpha_{\xi,n}^{MI}\le\alpha_{\xi,max}^{MI}
\end{cases}
\tag{4-6}
$$

where the superscript '*MA*' denotes the parameters in the macroscale, and '*MI*' in the microscale. The subscript ξ denotes the parameters in the curvilinear coordinates $\xi^j(\xi, \eta, \zeta)$. N is the total number of fixed knots in the micro design domain. The expansion coefficients of the CSRBF interpolation $\alpha_{\xi, n}^{MI}$ are the design variables in the microscale, ranging between $\alpha_{\xi, min}^{MI}$ and $\alpha_{\xi, max}^{MI}$. J is the equivalent objective function, comprised of the macro compliance J^{MA} and micro Poisson's ratio J^{MI}, where W_1 and W_2 are corresponding weight factors. V is the volume constraint, and the upper limit is defined as V_ξ^{max}. H is the Heaviside function[128] used to denote void and solid materials, given by:

$$H\left(\Phi_\xi^{MI}\right) = \begin{cases} \Theta & \Phi_\xi^{MI} < -\Delta \\ \dfrac{3(1-\Theta)}{4}\left(\dfrac{\Phi_\xi^{MI}}{\Delta} - \dfrac{\left(\Phi_\xi^{MI}\right)^3}{\Delta^3}\right) + \dfrac{1+\Theta}{2} & -\Delta \leq \Phi_\xi^{MI} \leq \Delta \\ 1 & \Phi_\xi^{MI} > \Delta \end{cases} \qquad (4\text{-}7)$$

where Θ is a small positive number to avoid the singularity of the element stiffness matrix, and Δ is the width for the numerical approximation of H. δ is the Dirac function which is the derivative of the Heaviside function H, and it can be described as:

$$\delta\left(\Phi_\xi^{MI}\right) = \begin{cases} \dfrac{3(1-\Theta)}{4\Delta}\left(1 - \dfrac{\left(\Phi_\xi^{MI}\right)^2}{\Delta^2}\right) & \left|\Phi_\xi^{MI}\right| \leq \Delta \\ 0 & \left|\Phi_\xi^{MI}\right| > \Delta \end{cases} \qquad (4\text{-}8)$$

The elasticity tensor of that shell element is comprised of D_b and D_s, as shown in Eq. (4-5), and the target Poisson's ratio is mainly related to D_b. Thus, the effective elasticity tensor of the microstructure $D_{ijkl}^H(D_{ijkl}^{bH}, D_s)$ is assembled by the effective D_{ijkl}^{bH} and the constant D_s. After that, the global stiffness matrix K_ξ^{MA} in the macro analysis domain

can be calculated by D_{ijkl}^{H}. Here, the optimized microstructure is defined as an isotropic or orthotropic material. Thus, there are two Poisson's ratios μ_1 and μ_2 defined in the micro objective function, and they can be obtained by D_{11}^{bH}, D_{12}^{bH}, D_{22}^{bH}, which are specific values of D_{ijkl}^{bH}, as shown in Eq. (4-9).

$$
\begin{aligned}
\mu_1 &= D_{12}^{bH}\left(\alpha_\xi^{MI}\right)\Big/D_{11}^{bH}\left(\alpha_\xi^{MI}\right) \\
\mu_2 &= D_{12}^{bH}\left(\alpha_\xi^{MI}\right)\Big/D_{22}^{bH}\left(\alpha_\xi^{MI}\right)
\end{aligned}
\tag{4-9}
$$

In the above formulas, Φ_ξ^{MI} is the level set function in the micro design domain Ω_ξ^{MI}. It can be calculated using spatial variables in the curvilinear coordinates (ξ, η, ζ) and time variables t based on the CSRBF interpolation in Eq. (4-10)

$$
\Phi_\xi^{MI}\left(\xi,t\right) = \varphi_\xi^{MI}\left(\xi\right)^T \cdot \alpha_{\xi,n}^{MI}\left(t\right)
\tag{4-10}
$$

The effective elasticity tensor D_{ijkl}^{bH} can be obtained by the numerical homogenization method:

$$
D_{ijkl}^{bH}\left(\alpha_\xi^{MI}\right) = \frac{1}{\left|\Omega_\xi^{MI}\right|}\int_{\Omega_\xi^{MI}} \beta_\xi^{MI} H\left(\Phi_\xi^{MI}\left(\alpha_\xi^{MI}\right)\right) d\Omega_\xi^{MI}
\tag{4-11}
$$

$$
\beta_\xi^{MI} = \left(\varepsilon_{pq}^{0(ij)} - \varepsilon_{pq}^{*}\left(u_\xi^{MI(ij)}\right)\right) D_{pqrs}^{b}\left(\varepsilon_{rs}^{0(kl)} - \varepsilon_{rs}^{*}\left(u_\xi^{MI(kl)}\right)\right)
\tag{4-12}
$$

where D_{pqrs}^{b} is the elasticity tensor of the solid material; ε_{pq}^{0} is the test unit strain field, $(1,0,0)^T$, $(0,1,0)^T$ and $(0,0,1)^T$ as for the 2D problem; ε_{pq}^{*} is the strain field related to the displacement u_ξ^{MI}, which can be calculated via FEA under the periodic boundary conditions of the microstructure:

$$
\int_{\Omega_\xi^{MI}}\left(\varepsilon_{pq}^{0(ij)} - \varepsilon_{pq}^{*}\left(u_\xi^{MI(ij)}\right)\right) D_{pqrs}^{b}\varepsilon_{rs}^{*}\left(w_\xi^{MI(kl)}\right) H\left(\Phi_\xi^{MI}\right) d\Omega_\xi^{MI} = 0, \ \forall\, w_\xi^{MI(kl)} \in \bar{U}\left(\Omega_\xi^{MI}\right)
\tag{4-13}
$$

where w is the virtual displacement field. The bilinear energy and the linear load forms

of the finite element analysis in the microscale can be described as:

$$F_\xi^{MI}\left(u_\xi^{MI}, w_\xi^{MI}, \alpha_\xi^{MI}\right) = \int_{\Omega_\xi^{MI}} \varepsilon_{ij}^*\left(u_\xi^{MI}\right) D_{pqrs}^b \varepsilon_{kl}^*\left(w_\xi^{MI}\right) H\left(\Phi_\xi^{MI}\left(\alpha_\xi^{MI}\right)\right) d\Omega_\xi^{MI} \quad (4\text{-}14)$$

$$L_\xi^{MI}\left(w_\xi^{MI}, \alpha_\xi^{MI}\right) = \int_{\Omega_\xi^{MI}} \varepsilon_{ij}^{0(ij)} D_{pqrs}^b \varepsilon_{kl}^*\left(w_\xi^{MI}\right) H\left(\Phi_\xi^{MI}\left(\alpha_\xi^{MI}\right)\right) d\Omega_\xi^{MI} \quad (4\text{-}15)$$

The bilinear energy and the linear load forms in the macroscale can be described as:

$$F_\xi^{MA}\left(u_\xi^{MA}, w_\xi^{MA}, D_{ijkl}^H\right) = \int_{\Omega_\xi^{MA}} \varepsilon_{ij}\left(u_\xi^{MA}\right) D_{ijkl}^H \varepsilon_{kl}\left(w_\xi^{MA}\right) d\Omega_\xi^{MA} \quad (4\text{-}16)$$

$$L_\xi^{MA}\left(w_\xi^{MA}\right) = \int_{\Omega_\xi^{MA}} p w_\xi^{MA} d\Omega_\xi^{MA} + \int_{\Omega_\xi^{MA}} \tau w_\xi^{MA} d\Gamma_\xi^{MA} \quad (4\text{-}17)$$

where p is the body force, and τ is the traction of the boundary Γ_ξ^{MA} in the macroscale.

4.3.2 Sensitivity analysis

Based on the above concurrent topology optimization model, the sensitivity of the objective function can be obtained. Because of two scales, the sensitivity is divided into two parts and calculated through the first-order derivatives of the objective functions with respect to the expansion coefficients $\alpha_{MI\xi}$. The sensitivity in the macro scale is:

$$
\begin{aligned}
\frac{\partial J^{MA}}{\partial \alpha_\xi^{MI}} &= \frac{1}{2}\int_{\Omega_\xi^{MA}} \left(u_\xi^{MA}\right)^T \frac{\partial K_\xi^{MA}\left(D_{ijkl}^H\left(D_{ijkl}^{bH}\left(\alpha_\xi^{MI}\right), D_s\right)\right)}{\partial \alpha_\xi^{MI}} u_\xi^{MA} d\Omega_\xi^{MA} \\
&= \frac{1}{2}\int_{\Omega_\xi^{MA}} \varepsilon_{ij}^T\left(u_\xi^{MA}\right) \frac{\partial D_{ijkl}^H\left(D_{ijkl}^{bH}\left(\alpha_\xi^{MI}\right), D_s\right)}{\partial \alpha_\xi^{MI}} \varepsilon_{kl}\left(u_\xi^{MA}\right) d\Omega_\xi^{MA}
\end{aligned}
\quad (4\text{-}18)
$$

The effective elasticity tensor D_{ijkl}^H contains two components, where D_{ijkl}^{bH} is the function of design variables and D_s is constant. Hence, the first-order derivatives of D_{ijkl}^H can be calculated by:

$$\frac{\partial D_{ijkl}^{H}\left(D_{ijkl}^{bH}\left(\alpha_{\xi}^{MI}\right),D_{s}\right)}{\partial \alpha_{\xi}^{MI}}=\frac{\partial D_{ijkl}^{bH}}{\partial \alpha_{\xi}^{MI}} \tag{4-19}$$

Then this sensitivity is utilized to calculate the first-order derivatives of D_{ijkl}^{bH} with respect to the design variables. Based on the shape derivative, the first-order derivatives of D_{ijkl}^{bH} with respect to the pseudo time t is:

$$\frac{\partial D_{ijkl}^{bH}}{\partial t}=\frac{1}{\left|\Omega_{\xi}^{MI}\right|}\int_{\Omega_{\xi}^{MI}}\beta_{\xi}^{MI}v_{\xi}^{n}\left|\left(\nabla \Phi_{\xi}^{MI}\right)^{T}\right|\delta\left(\Phi_{\xi}^{MI}\right)d\Omega_{\xi}^{MI} \tag{4-20}$$

v_{ξ}^{n} in Eq. (3-19) can be substituted in Eq. (4-20):

$$\frac{\partial D_{ijkl}^{bH}}{\partial t}=\left(\frac{1}{\left|\Omega_{\xi}^{MI}\right|}\int_{\Omega_{\xi}^{MI}}\beta_{\xi}^{MI}\varphi_{\xi}^{MI}\left(\xi\right)^{T}\delta\left(\Phi_{\xi}^{MI}\right)d\Omega_{\xi}^{MI}\right)\dot{\alpha}_{\xi,n}^{MI}\left(t\right) \tag{4-21}$$

The first-order derivatives of D_{ijkl}^{bH} with respect to t can also be calculated using the chain rule:

$$\frac{\partial D_{ijkl}^{bH}}{\partial t}=\frac{\partial D_{ijkl}^{bH}}{\partial \alpha_{\xi}^{MI}}\dot{\alpha}_{\xi,n}^{MI}\left(t\right) \tag{4-22}$$

Comparing Eq. (4-21) and (4-22), the first-order derivatives of D_{ijkl}^{bH} with respect to the expansion coefficients $\alpha_{MI\xi}$ can be given by:

$$\frac{\partial D_{ijkl}^{bH}}{\partial \alpha_{\xi}^{MI}}=\frac{1}{\left|\Omega_{\xi}^{MI}\right|}\int_{\Omega_{\xi}^{MI}}\beta_{\xi}^{MI}\varphi_{\xi}^{MI}\left(\xi\right)^{T}\delta\left(\Phi_{\xi}^{MI}\right)d\Omega_{\xi}^{MI} \tag{4-23}$$

Based on Eq. (4-23), the sensitivity in the microscale is also obtained by:

$$\frac{\partial J^{MI}}{\partial \alpha_\xi^{MI}} = \frac{\partial \left(\mu_1 +1\right)^2}{\partial \alpha_\xi^{MI}} + \frac{\partial \left(\mu_2 +1\right)^2}{\partial \alpha_\xi^{MI}} = \frac{\partial \left(D_{12}^{bH} / D_{11}^{bH} +1\right)^2}{\partial \alpha_\xi^{MI}} + \frac{\partial \left(D_{12}^{bH} / D_{22}^{bH} +1\right)^2}{\partial \alpha_\xi^{MI}} \quad (4\text{-}24)$$

And the derivatives of the volume constraint with respect to the design variables can be calculated by:

$$\frac{\partial V}{\partial \alpha_\xi^{MI}} = \int_{\Omega_\xi^{MI}} \varphi_\xi^{MI} \left(\xi\right)^T \delta\left(\Phi_\xi^{MI}\left(\alpha^{MI}\right)\right) d\Omega_\xi^{MI} \quad (4\text{-}25)$$

4.3.3 Numerical procedural
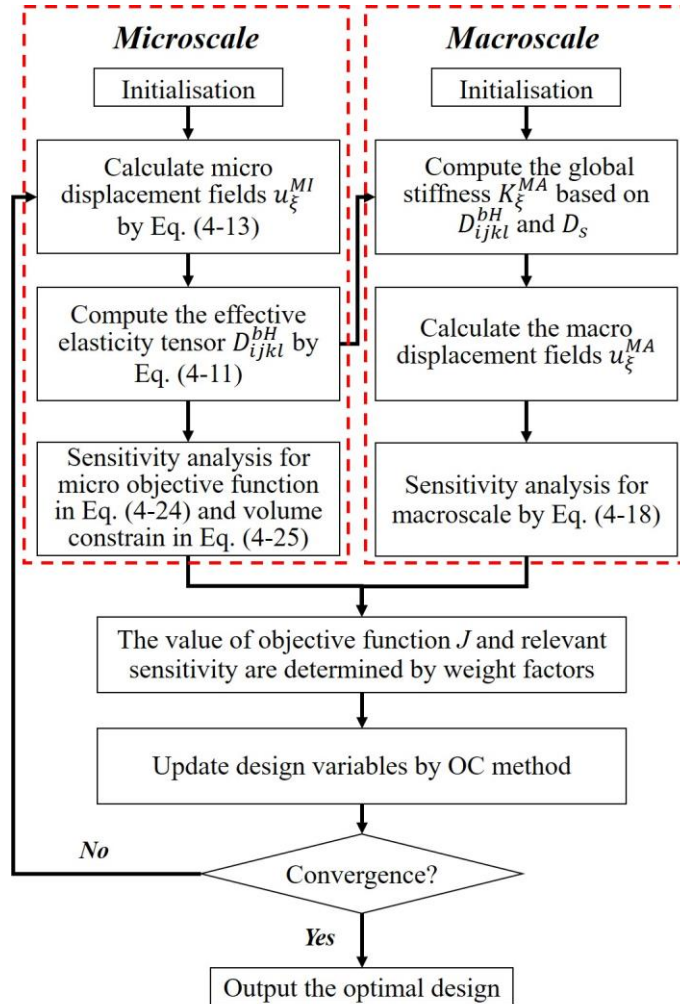
Figure 4-2 The flowchart of the concurrent topology optimization

The flowchart of the proposed optimization method is given in Figure 4-2. At first, the micro displacement fields u_ξ^{MI} is obtained by solving the equilibrium equation Eq. (4-13). Then, the effective elasticity tensor D_{ijkl}^{bH} can be computed by using the numerical homogenization method in Eq. (4-3). After that, the value of the micro objective function J^{MI} in Eq. (4-6) is calculated. The sensitivity of J^{MI} and the volume constraint with respect to design variables are obtained in Eq. (4-24) and (4-25), respectively. Simultaneously, the effective D_{ijkl}^{bH} and the constant D_s are utilized to compute the global stiffness matrix K_ξ^{MA} in macroscale, and then the macro equilibrium equation can be solved to get the macro displacement field u_ξ^{MA}. The macrostructural compliance and the derivative of J^{MA} are then calculated by J^{MA} in Eq. (4-6) and Eq. (4-18), respectively. Based on defined weight factors W_1 and W_2, the value of objective function J and relevant sensitivity can be determined. After that, the OC method is adopted to update design variables. The loop of the optimization is performed until the convergent criterion is satisfied.

4.4 Examples and discussion

The concurrent topology optimization is implemented with MATLAB to obtain the micro-structured cellular composite structure with auxetic deformation. In the process, a piece of thin-walled structure is adopted as the macro analysis domain, which is indicated in blue color in Figure 4-3, subject to the loading and boundary conditions. The displacement of the stent along the circumference is fixed, while two unit forces are applied on the left and right edges in the axial direction. Meanwhile, the micro design domain is indicated in red color in Figure 4-3. By considering the computational efficiency and accuracy, the macro analysis domain is discretized by 30×30 shell elements with four nodes, where each element has a unit length, height. The micro design

domain is discretized by 50×50 shell elements.

(A)   (B)
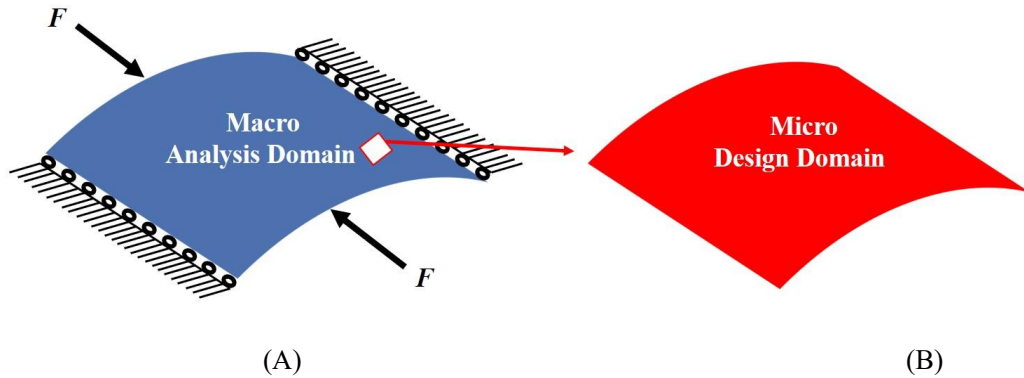
Figure 4-3 (A) Macro analysis domain; (B) micro design domain

Coronary Stents are tube-shaped devices with close-cell units to keep the clogged arteries open. Stents should have enough flexibility to accommodate turns or angles to adapt to a range of different arterial shapes. Therefore, no matter what kind of coronary stents, most of them have low volume fractions of materials. Different volume fractions in the optimization can lead to different results. In this design, a 35% volume fraction is adopted at first. The subsequent designs with smaller volume fractions will then be determined based on the design result with 35% material. To discuss design results, two parameters *Mu1* and *Mu2,* are defined:

$$Mu1 = D_{12}^{bH} \big/ D_{11}^{bH} , \quad Mu2 = D_{12}^{bH} \big/ D_{22}^{bH} \tag{4-26}$$

where D_{11}^{bH}, D_{12}^{bH}, D_{22}^{bH} are specific values within the effective elasticity tensor.

4.4.1 The result of 35% volume

The optimization results with a 35% volume fraction are presented in Figure 4-4. Four intermediate results are used to track the dynamic change of the structural boundary during the optimization process, as shown in Figure 4-4 (B-E), while (A) and (F) are the

initial design and the final result, respectively. Except for normal fluctuations from 10th to 30th optimization iterations, the objective function steadily minimized to close zero, and the convergence curve is shown in Figure 4-5 (A). The volume fraction of the structure is also steadily converged to 35%. These results indicate that the proposed method is robust. The changes in the two Poisson's ratios during the process are given in Figure 4-5 (B), where the results are Mu1=-0.8180 and Mu2=-0.8120. The two ratios are near '-1' close to the design objective, showing that the method can effectively achieve an auxetic design. However, the material distribution of the optimized structure is not uniform. The connections between the center and four branches are significantly thinner than other parts, leading to non-uniform distribution of radial force. It will easily cause stent fracture at the thin connections, resulting in high incidences of ISR and ST. Besides that, the central region of the structure is occupied by more than half materials without any gap, which may block side branches of arteries. Therefore, a smaller volume fraction of 25% is used to obtain a uniform material distribution.

| (A) | (B) | (C) |
| (C) | (D) | (E) |
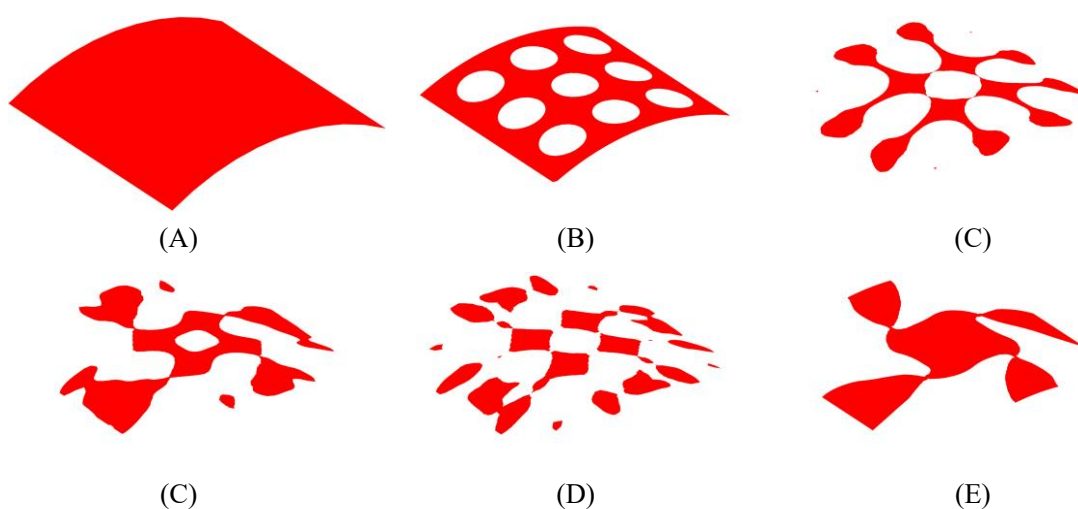
Figure 4-4 The optimization of 35% volume fraction: (A) Initial design; (B–E) four intermediate results; (F) final design.
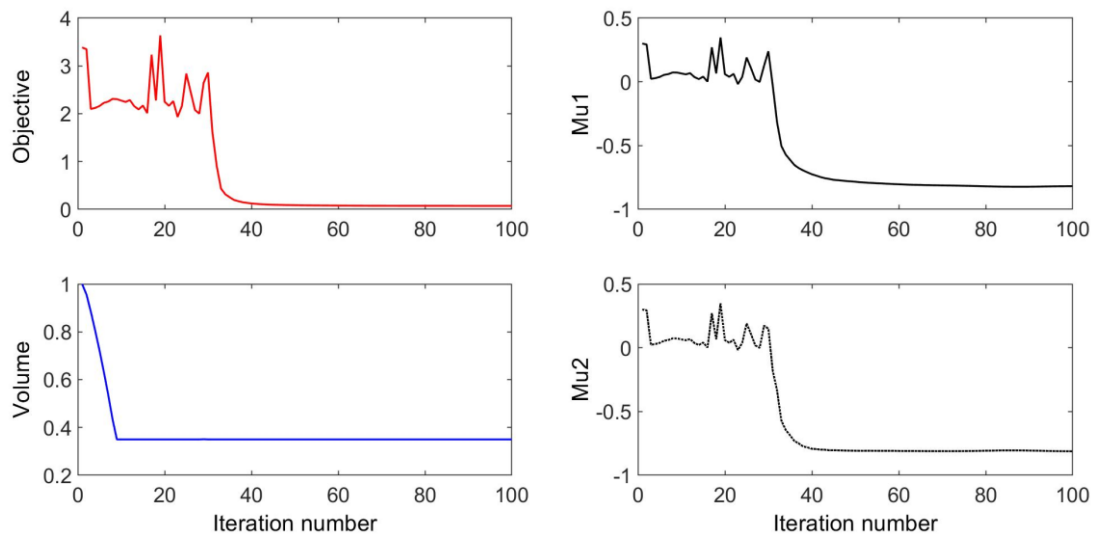
(A) objective and volume   (B) Poisson's ratios

Figure 4-5 The convergences of 35% volume fraction

4.4.2 The result of 25% volume

(A)   (B)   (C)

(C)   (D)   (E)
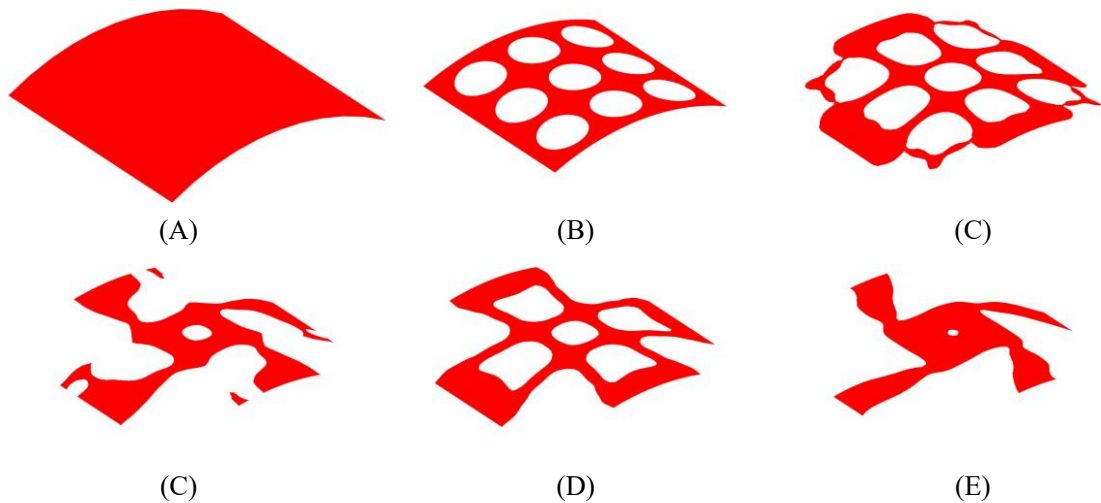
Figure 4-6 The optimization of 25% volume fraction: (A) Initial design; (B–E) four

intermediate results; (F) final design.

The optimization process of the 25% volume fraction is then presented in Figure 4-6. The convergence curves, similar to the design of 35%, can be found in Figure 4-7. The results of two Poisson's ratios are *Mu1*=-0.8209, and *Mu2*=-0.8179, respectively. Compared with the result of 35% volume, in this case, the materials in the four branches and connections

are better evenly distributed. However, the same issues still exist in the center of the structure, although a small hole is generated.

(A) objective and volume   (B) Poisson's ratios
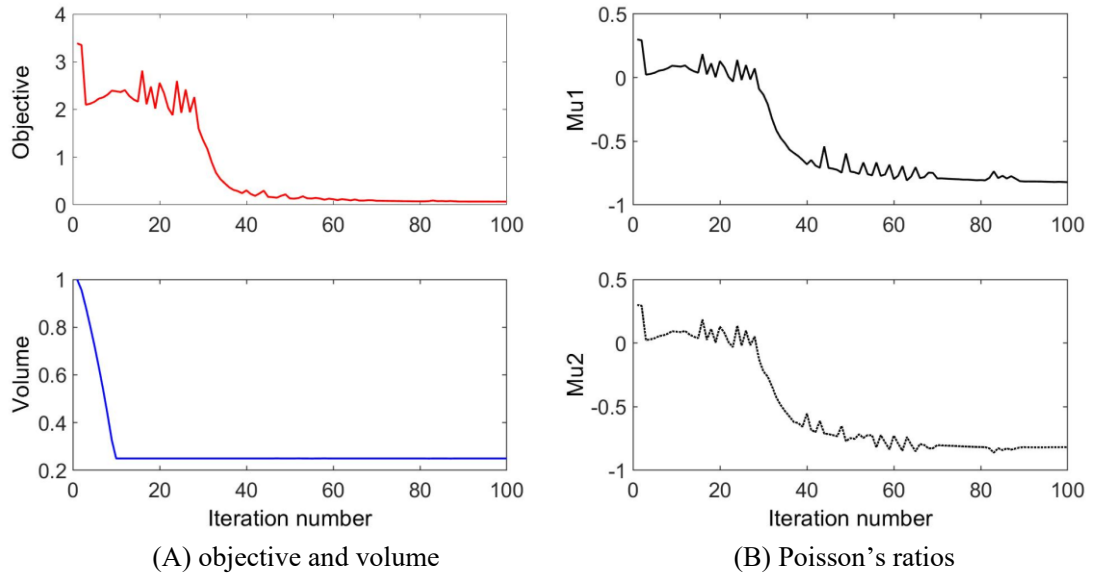
Figure 4-7 The convergences of 25% volume fraction.

4.4.3 The result of 20% volume

(A)   (B)   (C)

(C)   (D)   (E)
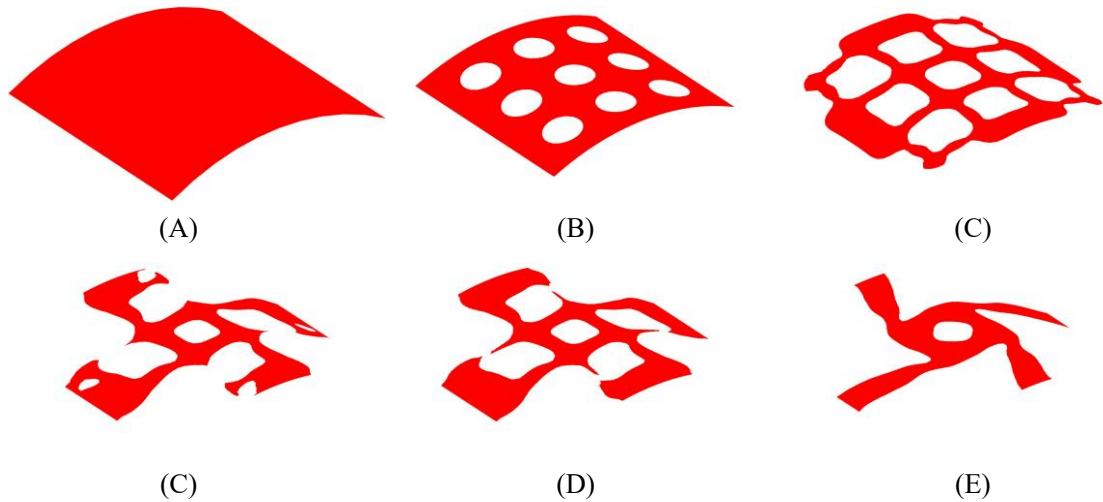
Figure 4-8 The optimization of 20% volume fraction: (A) Initial design; (B–E) four intermediate results; (F) final design

After that, a 20% volume fraction is used, aiming to remove more materials from the

centre position of the structure. The design results can be found in Figure 4-8, while the convergence curves are shown in Figure 4-9. The results of two effective Poisson's ratios of the microstructure are *Mu1*=-0.8180 and *Mu2*=-0.8186.

(A) objective and volume (B) Poisson's ratios
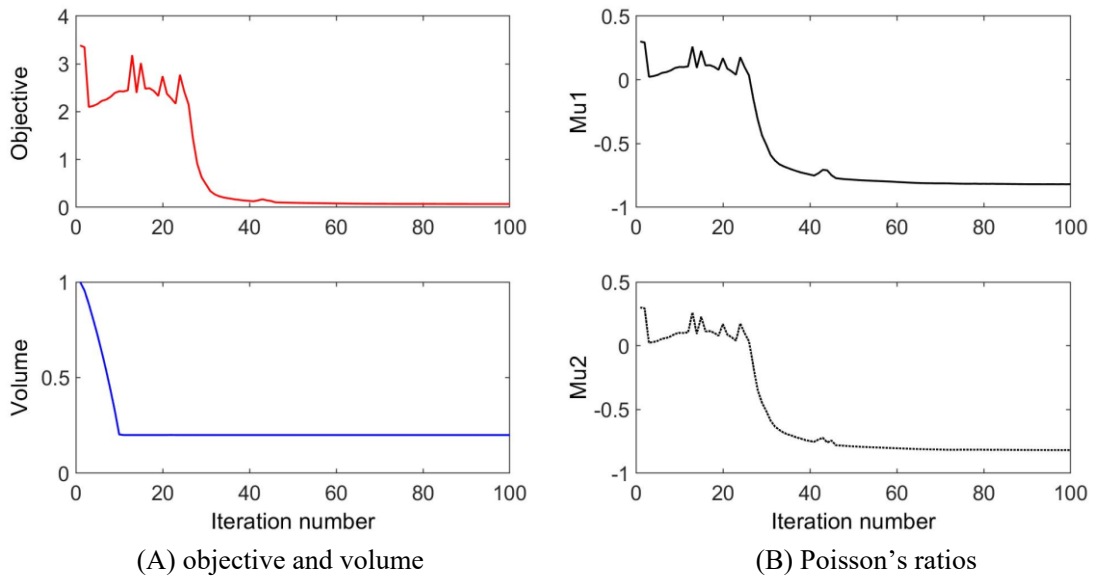
Figure 4-9 (A) The convergences of 20% volume fraction.
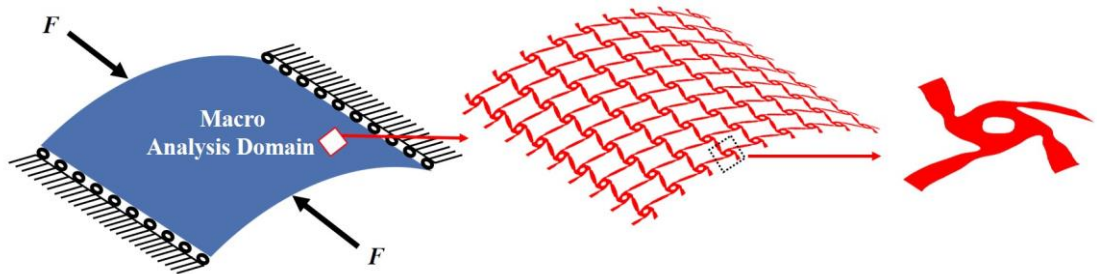
Figure 4-10 The final numerical design result

Hence, based on the comparison of these three designs, it can be seen all of them have similar negative Poisson's ratios at the circumferential and axial directions, and they are all close to the design objective. Nevertheless, the material distribution in the design of 20% is more uniform than others. It can provide a radial force that is better distributed to support vessels to prevent non-uniform expansion. The big hole in the center of the

structure increases the stent gap to benefit blood flow from side branches of the arteries. Although less cover rate of the stent can reduce the biological rejection, a reasonable amount of materials can provide stronger and long-last support for the vessel and prevent higher incidences of complications caused by mechanical failures of the stent. Therefore, the third numerical design is adopted, as shown in Figure 4-10.

4.5 Numerical validation by ANSYS

In order to perform the simulation for the design, the geometry should be built based on the numerical design result. Firstly, the numerical design result Figure 4-8 in MATLAB is output as an STL type file. The STL file is then imported into the software SpaceClaim, which is integrated into ANSYS, to get the solid geometry for simulations.
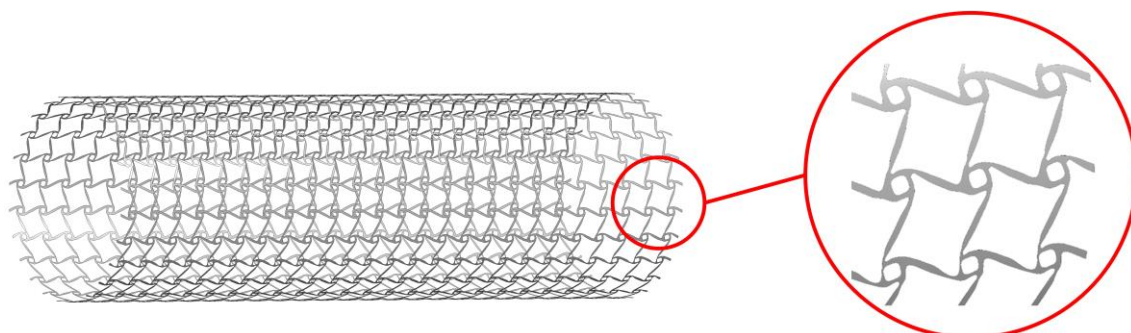
Figure 4-11 The geometry of the optimized stent

As mentioned in the design strategy, the optimized structure consists of periodic microstructures, but it is hard in practice to use microstructures with a very small scale by considering computational cost and manufacturing challenges. It is reasonable when considering the microstructures are actually independent of real dimensions but a relative scale. Therefore, the stenting architecture is assembled with 24 unit cells in the circumferential direction and 25 unit cells in the axial direction. Due to the use of the shell element, the geometry is created as a cylindrical surface with a specified thickness,

which can help reduce the computational cost. The geometry of the optimized stent structure is illustrated in Figure 4-11. As the commonly used material in SE stents, Nitinol is utilized for the optimized stenting architecture in the simulation.

4.5.1 Auxetic behavior

In that part, the compression and stretching tests are performed to validate the deformation mechanism of the optimized stenting architecture. The results are illustrated in Figure 4-12, where the grey outline wireframe shows the undeformed stent. With the compression, the NPR behavior can be easily found, which shows the size of the optimized stenting architecture becomes much smaller than the undeformed shape in both circumferential and axial directions, which will benefit the deliverability of the stent. Due to the stored strain energy from the elastic deformation, the stent structure can recover its undeformed shape via expansions in all directions when the compressed sent structure is released. Therefore, the auxetic deformation behavior can efficiently eliminate foreshortening when deploying the stent. NPR behavior can also be demonstrated in the stretching test. On the other hand, the conventional stent designs usually present the deformation behaviors with positive Poisson's ratios and will contract along the longitudinal direction when expand along the radial direction to support the vessel. And the foreshortening is an inevitable consequence for the conventional stent designs. Besides that, the maximum equivalent stress in the validation model is 299.76 *Mpa*, much smaller than the yield stress of material Nitinol that is usually greater than 600 *Mpa*. Hence the new stenting structure has good strength to withstand circle loading in practice and low the risk of failure fracture.

(A1)

(A2)

(B1)

(B2)
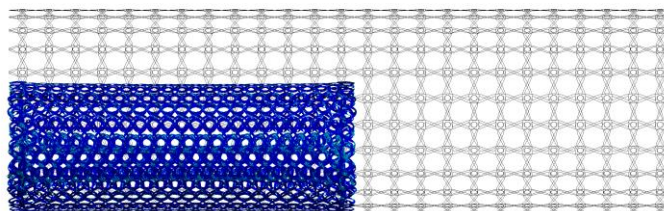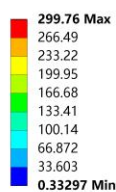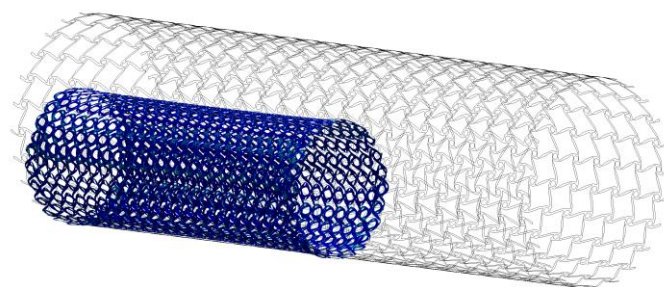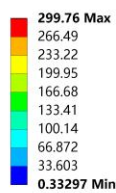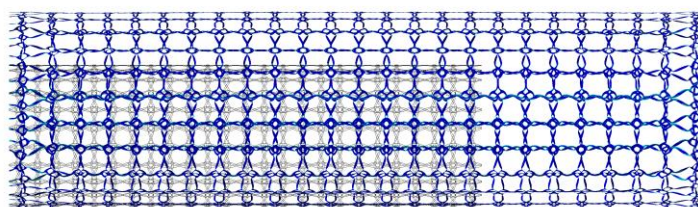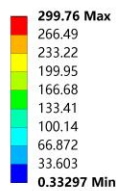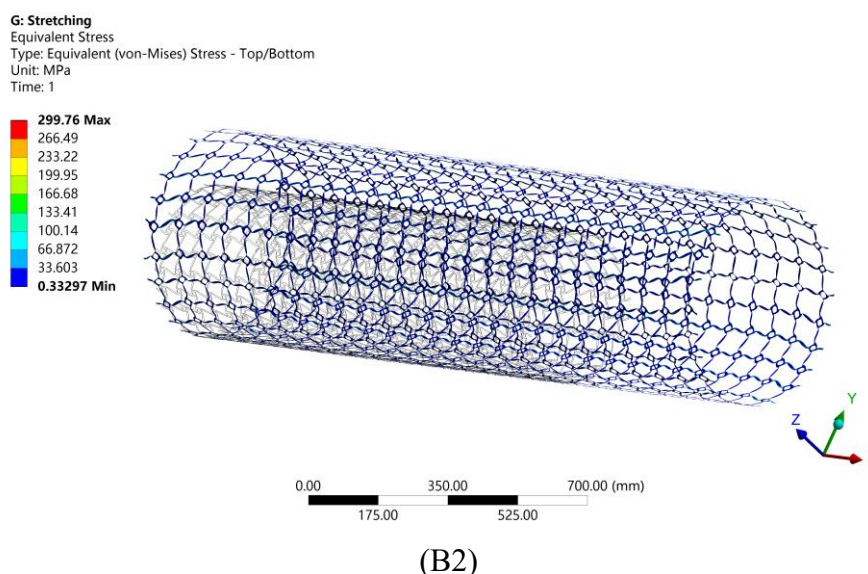
Figure 4-12 (A) Compression test; (B) Stretching test

4.5.2 Simulation of inadequate expansion and malapposition

Stents without desired flexibility and conformability may experience inadequate expansion and malapposition, further resulting in increased incidences of ST and ISR. However, due to the deformation behaviors with positive Poisson's ratios, most conventional stents will contract along the longitudinal direction after expansion leading to a decrease of flexibility along the longitudinal direction. Compared with the conventional stents, the optimized auxetic stent can obtain an opposite deformation behavior and increase the flexibility after deployment, which can help overcome the above issues. Therefore, the stent simulation is to test these mechanical performances of the optimized stenting architecture. The LS-DYNA within ANSYS is utilized to simulate the expanding process for the stent. By considering the computational cost, only a part of the stent is illustrated to simulate the expansion of the stent to the target vessel with a big plaque on the surface, as shown in Figure 4-13. From the result, it can be seen that the stent adequately expands to cover the entire lesion and adaptively deforms to fit the shape

of the vessel with no gaps around the plaque. As we know, the stent malapposition can be described as gaps existing between the stent and the vessel wall. Hence, the current simulation result can demonstrate that the optimized stent structure has excellent flexibility and conformability to prevent stent inadequate expansion and malapposition. Finally, all these benefits will help reduce the incidence of ST and ISR.

(A)

(B)
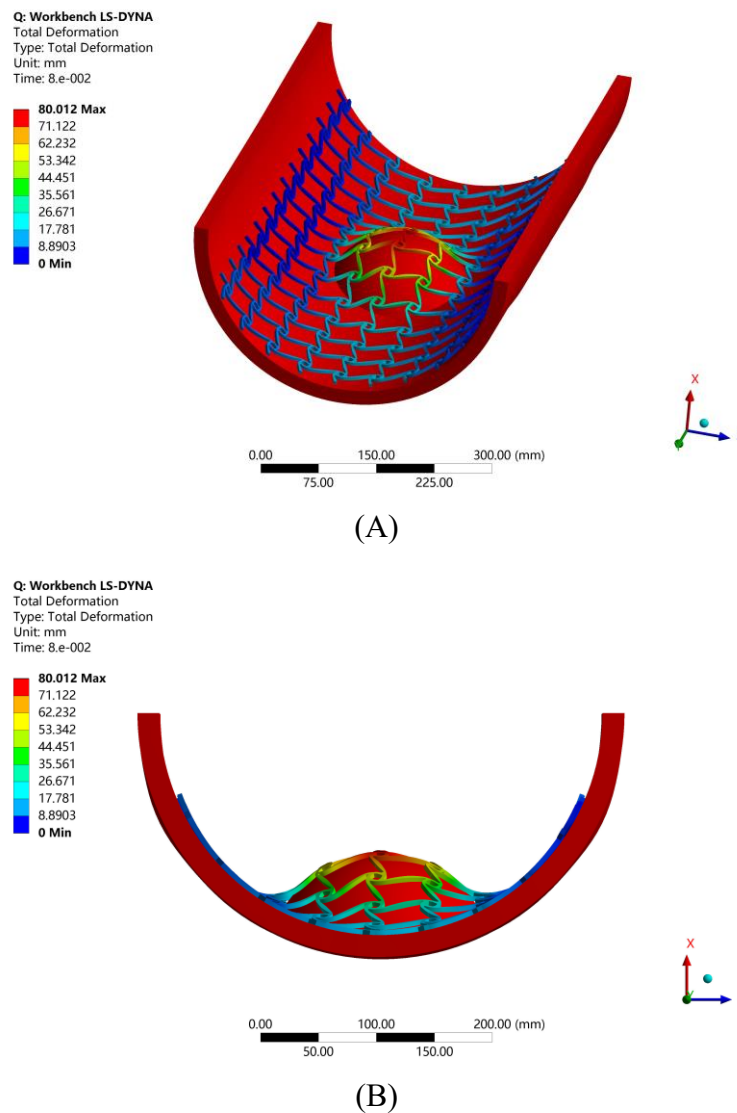
Figure 4-13 Stent expansion test

4.6 3D printing

The additive manufacturing (3D printing) technology is particularly beneficial to the

fabrication of solid geometries with complex shapes. Topologically optimized microstructures are often characterized by complex geometries, not compatible with most conventional manufacturing techniques. Hence it is a natural choice to implement topological designs with 3D printing methods. The designed stenting architecture prototype is enlarged by 15 times and then was printed using the Stratasys J750 machine at the ProtoSpace, the University of Technology Sydney. This machine can produce ultra-smooth surfaces and refined features with layer thickness as fine as 0.014 mm to represent the stent structure with auxetic microstructures.
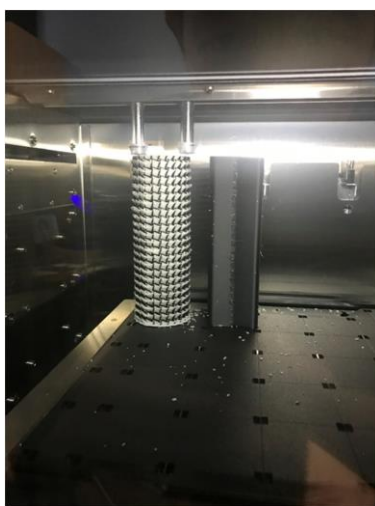
(A) The printer Stratasys J750   (B) The stenting structure
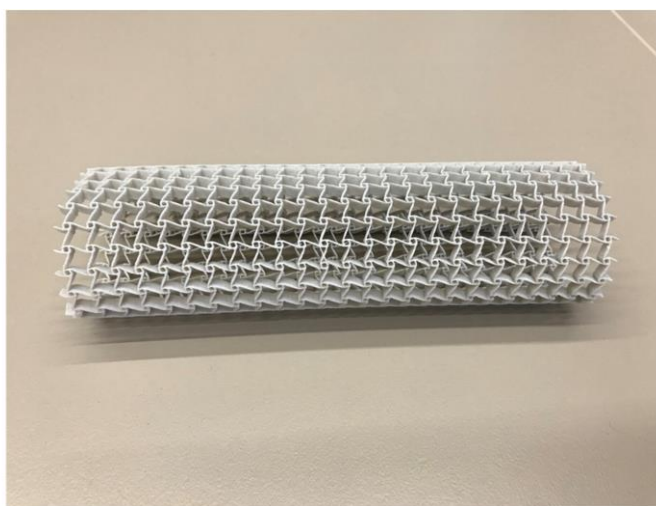
Figure 4-14 The prototype of the optimized auxetic stent

Due to the limitations of the cost and lab equipment, metallic materials such as Nitinol are not employed. A kind of plastic material is used as a prototyping validation to the optimized design. The prototyping material is composed of 30% Vero and 70% Tango, which can approximate the property of elastomer. The prototype is printed layer by layer following the axial direction, as shown in Figure 4-14 (A). The prototype is supported by a solid cylinder filled with the same material to avoid the structural deformation during the printing. After that, the inside cylinder will be washed. The final prototype for the

demonstration of the new stenting structure with 1.5mm thickness is shown in Figure 4-14 (B). The testing and characterization of the auxetic SE stents with nitinol or other metallic biocompatible materials are out of the thesis scope and will be conducted in future work.

4.7 Conclusion

This chapter proposes a topology optimization method for the design of auxetic SE stents to reduce the risks of ST and ISR caused by mechanical or procedural factors of SE stents, such as inadequate stent expansion, stent fracture, stent foreshortening, and malapposition. This design aims to reduce the incidence of ST and ISR of SE architectures, more from the mechanical structural and procedural aspects than the biological material aspect. However, the design factors of stents often influence the biological and even clinical outcomes. The importance of between stenting architectures and biological safety in the process of coronary artery disease has been shown in the study. The X-PLSM, in conjecture with the numerical homogenization method, is proposed to establish a heuristic multiscale topology optimization approach for seeking novel auxetic stenting structural architecture. The main drawbacks of most current SE stents are expected to be avoided.

The numerical examples and simulations show that the topologically optimized structures offer auxetic deformation that can enable the stenting structures automatically and adaptively to deform (e.g., expansion). The unusual deformation mechanism will help overcome the inadequate stent expansion, stent fracture, and stent malapposition, particularly in SE stents. The auxetic structures can also miniaturize the catheter enclosing the stent, which increases the deliverability of the stent system during the PCI procedure and avoids the immediate injure of the vessel. The stenting structures can also supply

variable hoop strengths that will adapt to different radial forces when the artery cross-sectional shapes change. When the shape gets smaller, larger hooping strength, and vice versa, the enhanced indentation performance. By the way, the auxetic structures will normally have a better capability to absorb vibration energy. Moreover, the proposed design optimization methodology and the auxetic cellular composite structures can also be extended to other biomedicine implants, such as esophageal stents, biliary stents, and femoropopliteal artery stents.

Chapter 5 Hemodynamic optimization of auxetic stents

This chapter is mainly based on our research work: ***Design of Self-Expanding Auxetic Coronary Stents by considering hemodynamics Using Topology Optimization***. It is about to be submitted to an international scientific journal, ***IEEE Transactions on Biomedical Engineering***.

The result of Chapter 4 shows that the application of auxetic property in stent design can enhance stenting mechanical performances and reduce ST and ISR incidences. However, apart from these mechanical factors, the adverse hemodynamic changes induced by implanting stents are also associated with higher risks of stent thrombosis (ST) and in-stent restenosis (ISR). It is another essential aspect and should be taken into account in stent designs.

Although the associations between stenting structural characteristics and the induced hemodynamic changes in coronary arteries have been widely studied, the developments of associated optimization strategies are still very limited. One of the reasons is that most related studies adopt size or shape optimization methods, which are strongly dependent on the initial design variables and subject to the initial topology of the structure. The optimized results consequently have limited improvements for the desired objectives. Another reason is that it is hard to consider all the stenting structural characteristics simultaneously by using the current optimization models. That is because a large amount of design variables is needed to define the structural parameters by using size or shape optimization methods, which significantly increases the difficulty of the optimization. However, any stenting structural alteration can induce the change of the local flow

environment. Only a few structural design variables cannot capture the real beneficial design.

This chapter adopts the topology optimization based on PLSM to overcome the above limitations and seek the optimal material distribution for the stent to minimize the adverse flow reactions in the stented arteries. In order to associate the design variables with the flow motions around the stent, a homogenized effective modify fluid permeability(MFP) is proposed, where a Darcy-Stokes coupling system is established in the design domain to describe the behaviors of the stent and fluid. Besides that, the design of auxetics and the macroscopic stiffness are performed simultaneously to enhance the mechanical performances. Thus, a multiscale topology optimization model with multi-objective is proposed. Three design objectives in the multiscale are defined in the model: the auxetic properties, the MFP, and the macroscopic stenting stiffness.

In this chapter, the assumptions are proposed to simplify the establishment of the topology optimization design model. Then, the multiscale multi-objective optimization model is established. After that, the optimized stent is numerically obtained and validated in the commercial software MATLAB and ANSYS, respectively. Finally, both advantages and disadvantages of the proposed optimization method are discussed.

5.1 Assumptions and design domain

5.1.1 Assumptions

The optimization design is established based on the simulations of both mechanical and hemodynamic behaviors of the stent. The related mechanical simulation can refer to the design in Chapter 4. As for evaluating the hemodynamic behavior of the stent in the

arteries, blood flow needs to be simulated. However, the complex endovascular flow environment and the interactions between blood, stent, and endothelial cells significantly increase the difficulties of the fluid simulations. Although CFD provides an efficient way to solve fluid motion equations, the complex blood flow model still leads to a very high computational cost. That is why the stented hemodynamic studies usually use some assumptions to simplify the computational model. As discussed in Chapter2, some assumptions have been demonstrated that have small influences on the results and have been widely accepted, such as adopting a steady flow state instead of a pulsatile one. Therefore, some assumptions are also specified in this chapter to simplify the CFD model to facilitate the optimization design.

Blood in the simulation is known as an incompressible fluid, so the Navier-Stokes (NS) equations with incompressible conditions are utilized to describe the motion of blood flow. Eq. (5-1) is the momentum equation; Eq. (5-2) denotes the incompressibility condition; Eq. (5-3) is the no-slip condition on the boundary. The equations can help to have a clear understanding of the assumptions for the fluid model.

$$\rho \frac{\partial \mathbf{u}}{\partial t} + \rho \left(\mathbf{u} \cdot \nabla \right) \mathbf{u} - \mu \Delta \mathbf{u} = -\nabla p + \rho \mathbf{g} \quad \text{in} \, \Omega_{\mathrm{f}} \tag{5-1}$$

$$\nabla \cdot \mathbf{u} = 0 \quad \text{in} \, \Omega_{\mathrm{f}} \tag{5-2}$$

$$\mathbf{u} = 0 \quad \text{on} \, \Gamma_{\mathrm{f}} \tag{5-3}$$

where Ω_{f} is a fluid domain with boundary Γ_{f}. ρ and μ denote fluid density and viscosity, respectively. $\mathbf{u}$ is the flow velocity; t is time; p is the pressure. $\mathbf{g}$ is body accelerations acting on the fluid, such as gravity and inertial, while $\rho\mathbf{g}$ denotes the external body force vector. ∇, Δ and $\nabla\cdot$ are the gradient, Laplacian, and divergence operators, respectively.

In this optimization model, the assumptions can be divided into two different aspects. One is related to the stenting structural characteristics, including the definition of the design domain and the simplification of the stent structure. Another one is about the CFD model, including fluid movements, boundary conditions, and material models.

(1) Assumptions related to the stenting structural characteristics:

a)   It is assumed that the stent consists of periodic unit cells. All the unit cells share a uniform structure. Compared with the stent dimension, each unit cell can be regarded as a microstructure and consists of fluid material and solid material.

   With this assumption, the effective properties of the stent can be achieved by performing the numerical homogenization method for the microstructures, such as the effective elasticity tensor and fluid permeability.

b)   The stent is assumed as a rigid body in the CFD analysis.

   It means no deformations of the stent are generated under blood flow. Thus, the interactions between the stent and fluid are ignored.

c)   The stenting geometry is assumed as a straight body with constant thickness and uniformed horizontal cross-section profile.

   Rather than cylindrical shape, the stent with a straight body was demonstrated as a reasonable assumption in the CFD model [81]. Under the assumption, the three-dimensional(3D) layout of the stent can be determined by the horizontal cross-section profile, which can be defined as a two-dimensional(2D) design domain. Compared with a 3D design domain, the amount of design variables is significantly reduced in the 2D design region. It can save the computational cost consequently. The details of

this assumption will be discussed in section 5.2.

(2) Assumptions of the CFD model:

a) Blood flow is assumed as an incompressible Newtonian fluid with a steady flow state.

Although blood exhibits non-Newtonian behavior in small branches and capillaries, blood belongs to Newtonian fluid in most arteries, which means the viscosity μ can be a constant [70]. The pulsatile motion is another characteristic of blood flow, but the steady-state assumption is demonstrated as reasonable in the related CFD model and can help simplify the fluid flow behavior. It indicates that the inlet velocity of the fluid is constant and does not change with time. Hence, the unsteady item in the Eq. (5-1) can be neglected.

b) No-slip conditions are only assumed on the part of the outer boundaries of the design domain.

In CFD models, no-slip boundary conditions are typically applied along the solid-fluid interfaces and require updating at every optimization iteration. Thus, penalizations are applied to the flow to simplify the constraints of solid-fluid interfaces, where the nodal velocities of solid regions are forced to close zero. Consequently, no-slip conditions along the solid-fluid interfaces in the design domain are implicitly tied into the penalizations to the flow, and only parts of the outer boundaries of the design domain require explicit no-slip constraints.

c) The terms of convective and inertia in Eq. (5-1) are neglected.

The design domain is assumed located at an extracted horizontal cross-section of the stent, where one of the periodic 2D micro patterns at that section is defined as the

design domain. The extracted cross-section is a portion of a near-wall section that very close to the endothelium cells of the artery. By regarding no-slip conditions along the fluid-solid interfaces, the fluid velocity in the design domain is relatively slow compared with other locations in the artery, and the inertial force of the fluid is smaller than the viscous force. Although the CFD model for the hemodynamic simulation is a 3D unit cell, only a thin layer of blood flow along the stent surfaces is involved in the computational model, and the motion is also mainly affected by the no-slip conditions long the solid-fluid surfaces. Hence, blood flow in the optimization model can be further simplified as a Stokes flow.
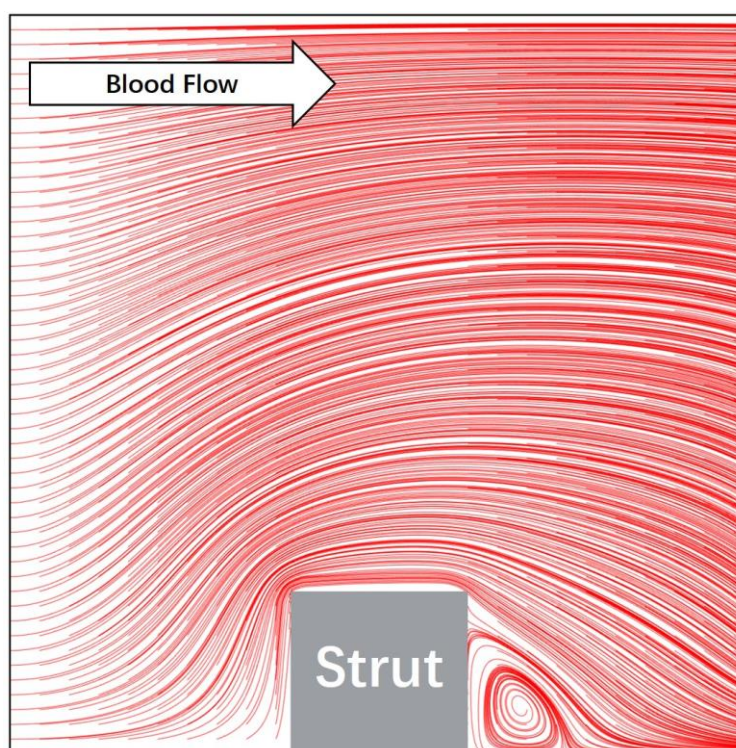
Figure 5-1 Flow pattern in the design domain

Besides that, the adverse hemodynamic influences of stents are mainly induced by disturbing the local blood flow. Their relationship can also be well captured with the assumptions of Stokes flow. An illustration of the stented disturbance under a Stokes

flow is shown in Figure 5-1. It can be seen that the flow patterns are disturbed by the obstruction of the strut, and the fluid motion behind the strut is mainly generated by the influence of viscous forces, where a recirculation zone is formed. Although the convective and inertia items in the Navier-Stokes equations are neglected, the stent disturbance to the blood flow can still be detected in the simplified model. Hence, the optimization of stenting hemodynamic behaviors can also be obtained under the assumption of Stokes flow.

d)   Constant pressure is assumed as the outlet condition of the fluid.

The orders of velocity and pressure are different in Eq. (5-1), and only the pressure gradient exists. Besides that, the Eqs. (5-2) and (5-3) are independent of pressure. Hence, constant pressures are practically specified at some boundaries to obtain a unique pressure field, such as zero pressure on the outlet of the flow domain.

5.1.2 Computational model and design domains

Based on the structural characteristics of the stent, different computational and design domains are defined to reduce the design variables and save the computational cost. The computational domain is a 3D region containing one stenting microstructure and the surrounding blood regions. The design domain is a 2D region extracted from the horizontal cross-section of the stenting microstructure in the computational domain and consists of solid and fluid phases. The relationship between the two domains is presented in the following.

As we know, in the stented segment of the artery, blood flows through the inner lumen of the stent and fills the gaps between stent struts. The fluid is separated by the stent and divided into different regions. Thus, a 3D computational domain based on one stenting

microstructure is established to evaluate the flow changes around the stent, as shown in Figure 5-2.
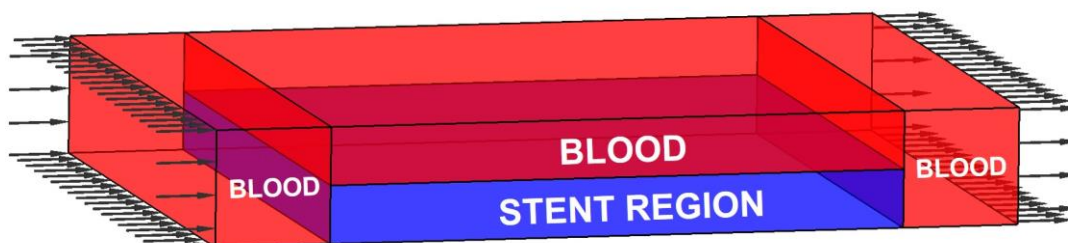
Figure 5-2 The 3D computational domain

The computational domain has four regions, three blood regions with red colour and one stent region with blue colour. In the middle of the domain, two layers are defined and share the same thickness as the stenting microstructure. One microstructure of the stent is defined in the stent region located at the bottom layer, while blood flows through the whole top layer and fills the gaps between stent struts in the bottom layer. Hence, the stent region is comprised of one stenting microstructure and filled with blood in struts gaps. Besides that, another two blood regions with the same length are defined in the two ends of the stent region to avoid the impact of the flow boundaries on the stent region, as shown in Figure 5-2. Since the convective item is ignored for the fluid, various lengths of inlet and outlet have a small effect on the fluid. The CFD simulation is then performed under the loads and boundary conditions:

1) A constant inlet velocity of blood flow is specified on the left side of the domain.

2) The outlet boundary is defined as zero pressure located on the right side.

3) No-slip conditions are applied on both the top and bottom surfaces of the simulation region; no additional conditions are applied for the solid-fluid interfaces due to the

restriction for the flow in the solid regions.

As the assumption of constant thickness, a 2D horizontal cross-section profile is extracted from the stenting microstructure and defined as the design domain. It is located at a near-wall section in the stent region, where the bottom of the stent region is defined as the endovascular wall.

When obtaining the velocity vector of the computational domain, the blood velocity field in the design domain can be extracted to evaluate the specified index of the hemodynamic changes, such as a modified permeability of the design domain defined in this thesis. The design variables will then be updated via the updating algorithm, and the profile is therefore updated in the design domain. After that, the material layout of the stent region in the computational domain can be updated by the new microstructural profile. The associations between the computational and design domains are consequently established. More details about the modified homodynamic index will be given in section 5.4.

5.2 Darcy-Stokes model applied in the microscale

In order to perform the optimization for the mechanical and fluid behaviors of the micro design domain simultaneously, the related simulations should be set up firstly, where two issues need to be taken into account. One is the no-slip conditions along the solid-fluid interfaces should be maintained. Another one is that the combination of element interpolation functions for velocity and pressure in the CFD model should be stable.

As for the first issue, the application of the Darcy-Stokes approach in saturated porous mediums [152, 187] provides an efficient way to deal with the moving-boundary no-slip conditions for solid-fluid interfaces, where the solid region can be treated as a porous

medium with flow governed by Darcy's law and the fluid region is treated as Stokes flow. After that, a single analysis model combined by scaling Darcy and Stokes equations can be established. In the model, a penalization to flow in the solid region is taken by assigning a low permeability to drive the velocity to close zero, and the no-slip conditions along the solid-fluid interface are consequently not needed [187, 188].

Another one is a stability issue about the combination of element interpolation functions for the velocity and pressure in both Darcy and Stokes flows. The velocity and pressure are dependent variables but with different orders in either Darcy or Stokes flow. The motion equations in each flow can lead to mixed pressure-velocity formulations, while the incompressible condition arises a stability requirement for the combination of the interpolation functions [189, 190]. However, not all combinations are stable [189, 191], and it was demonstrated that the classic mixed combinations could produce oscillating pressures [189] because Babuška-Brezzi or inf-sup conditions [192, 193] are unsatisfied. Computationally, as the most convenient combination, the equal-order interpolations are essential simplification techniques in this thesis but fail to satisfy the stability conditions. In order to use equal-order interpolation functions for the combinations, the stabilized mixed finite element methods proposed by Hughes et al. [189] is adopted for Stokes flow, while the method proposed by Masud and Hughes [191] is adopted for Darcy flow. Both stabilized mixed methods can help to circumvent restrictions of the Babuška-Brezzi conditions

5.2.1 Stokes flow

Stokes flow, also known as creep flow, is usually used to describe a steady viscous fluid flow with slow velocity, and the items of convective and inertia are not included in the

momentum equations. As discussed above, the design domain of the optimization model is defined as a microstructure of the stent and located at a near-wall section that closes to no-slip boundaries, where the effect of viscous forces is larger than the inertial forces. It is possible to regard the fluid as Stokes flow in the design domain. Besides that, Stokes flow is also suitable for the simulation of the flow in small length-scales. Therefore, the blood flow behavior in the micro design domain is consequently assumed as Stokes flow.

The hemodynamic optimization for the stenting structure is to minimize its adverse effect on the blood flow. In other words, the optimization aims to seek the material layout of the stent to reduce the stent-introduced disturbances and recover the flow patterns, and finally facilitate the blood flow through the stented segment. To some extent, although the assumption of Stokes flow simplifies hemodynamic behaviors in the design domain, the disturbances of the stent under the blood flow are not changed and can also be detected, which can be demonstrated in Figure 5-1. Hence, the fluid flow model under that assumption can also capture the disturbances caused by the stent and, consequently, set up the base of the related hemodynamic optimization model. Moreover, Stokes equations are a linearization of the Navier-Stokes equations, thus reducing the computational cost. Typical equations of Stokes flow can be given as the following:

$$\mu \Delta \mathbf{u} = \nabla p - \mathbf{f} \quad \text{in } \Omega_{\mathrm{f}}$$

$$\nabla \cdot \mathbf{u} = 0 \quad \text{in } \Omega_{\mathrm{f}} \tag{5-4}$$

$$\mathbf{u} = 0 \quad \text{on } \Gamma_{\mathrm{f}}$$

where the Eqs. (5-4) are directly simplified from the NS equations, and $\mathbf{f}$ is the external body force vector. In order to perform stable finite element analysis by using equal-order

interpolation functions for the velocity and pressure, a Petrov-Galerkin formulation proposed by Hughes et al. [189] is adopted as a stabilization technique for Stokes flow, and the matrix form is given by Eq. (5-5).

$$
\begin{bmatrix}
\mathbf{K}_s & -\mathbf{G}_s \\
\mathbf{L}_s + \mathbf{G}_s^{\mathrm{T}} & \mathbf{M}_s
\end{bmatrix}
\begin{bmatrix}
\mathbf{u} \\
\mathbf{p}
\end{bmatrix}
=
\begin{bmatrix}
\mathbf{F}_s \\
\mathbf{H}_s
\end{bmatrix}
\tag{5-5}
$$

where the subscript 's' emphasizes Stokes flow. $\mathbf{u}$ and $\mathbf{p}$ denote velocity and pressure vectors, respectively. $\mathbf{K}_s$ is the viscosity stiffness matrix; $\mathbf{G}_s$ is the gradient matrix; $\mathbf{G}_s^{\mathrm{T}}$ is the divergence matrix; $\mathbf{L}_s$ is the consistency matrix; $\mathbf{M}_s$ is the stabilization matrix; $\mathbf{F}_s$ and $\mathbf{H}_s$ are the nodal forces obtained from body forces and boundary conditions. More details about the definitions of these matrices are discussed in [189].

5.2.2 Darcy flow

Darcy flow usually describes the flow of a fluid through a porous medium, derived from the NS equations by the homogenization method [194]. The defined design domain consists of solid and fluid material. In order to combine the two material phrases into a single finite element system, the solid regions can be treated as porous mediums govern by Darcy flow, where the nodal velocities are driven to close zero. After that, the no-slip conditions along the solid-fluid interfaces are tied into the Darcy flow, and related additional restrictions are not needed anymore. Typical equations of Darcy flow can be given as the following:

$$\mathbf{u} = -\frac{k}{\mu}\left(\nabla p - \mathbf{f}\right) \quad \text{in } \Omega_f$$

$$\nabla \cdot \mathbf{u} = 0 \quad \text{in } \Omega_f \tag{5-6}$$

$$\mathbf{u} = 0 \quad \text{on } \Gamma_f$$

A stabilized mixed finite element method with no mesh-dependent for Darcy flow proposed by Masud and Hughes [191] is adopted to combine the interpolations of velocity and pressure fields. The stabilized matrix form for Darcy flow is given by:

$$\begin{bmatrix} \mathbf{K}_d & -\mathbf{G}_d \\ \mathbf{G}_d^{\mathrm{T}} & \mathbf{M}_d \end{bmatrix}\begin{bmatrix} \mathbf{u} \\ \mathbf{p} \end{bmatrix} = \begin{bmatrix} \mathbf{F}_d \\ \mathbf{H}_d \end{bmatrix} \tag{5-7}$$

where the subscript 'd' indicates the matrices defined for Darcy flow. $\mathbf{u}$ and $\mathbf{p}$ denote velocity and pressure vectors in Darcy flow. $\mathbf{F}_d$, and $\mathbf{H}_d$ are nodal forces similar to the Eq. (5-6). $\mathbf{K}_d$ is the viscosity stiffness matrix whose interpolation function is different from Stokes flow; $\mathbf{G}_d$ is the modified gradient matrix; $\mathbf{G}_d^{\mathrm{T}}$ is the modified divergence matrix; $\mathbf{M}_d$ is the stabilization matrix. All these element matrices are computed in [191].

5.2.3 Darcy-Stokes coupling

To simultaneously optimize mechanical and fluid behaviors of the micro design domain, a single finite element system mixed by Darcy and Stokes flows is used. In the coupling system, the solid phase is governed by Darcy's law, and the fluid phase is Stokes flow. The stabilized matrix form for Darcy-Stokes coupling is given by:

$$\begin{bmatrix} \mathbf{K}_{ds} & -\mathbf{G}_{ds} \\ \mathbf{G}_{ds}^{\mathrm{T}} & \mathbf{M}_{ds} \end{bmatrix}\begin{bmatrix} \mathbf{u} \\ \mathbf{p} \end{bmatrix} = \begin{bmatrix} \mathbf{F}_{ds} \\ \mathbf{H}_{ds} \end{bmatrix} \tag{5-8}$$

where the matrices in the Darcy-Stokes system are combined within the level set method

as the following interpolation:

$$\mathbf{K}_{ds}(x) = A\left\{ H(\Phi(x))\mathbf{K}_d + \left[1 - H(\Phi(x))\right]\mathbf{K}_s \right\}$$

$$\mathbf{G}_{ds}(x) = A\left\{ H(\Phi(x))\mathbf{G}_d + \left[1 - H(\Phi(x))\right]\mathbf{G}_s \right\}$$

$$\mathbf{G}_{ds}^{T}(x) = A\left\{ H(\Phi(x))\mathbf{G}_d^T + \left[1 - H(\Phi(x))\right]\left(\mathbf{L}_s + \mathbf{G}_s^T\right) \right\}$$

(5-9)

$$\mathbf{M}_{ds}(x) = A\left\{ H(\Phi(x))\mathbf{M}_d + \left[1 - H(\Phi(x))\right]\mathbf{M}_s \right\}$$

where *A* is the standard finite element assembly routine. The subscript 'ds' denotes the matrices defined in the Darcy-Stokes coupling system. $H(\Phi(x))$ is the Heaviside function [128] of the level set function $\Phi(x)$ at the design point *x*. It indicates solid elements have Darcy stiffness, while void elements have Stokes stiffness.

5.3 Homogenization of the stent properties

As the geometric simplifications are discussed in section 5.1, the stent is assumed to consist of periodic uniform microstructures. One of them is simplified as a straight body with a constant thickness and is defined in the 3D computational domain, which is established in section 5.2. A near-wall horizontal cross-section profile of this microstructure is extracted and defined as the 2D design domain. The numerical homogenization method is used for the 2D micro design domain to compute the homogenized effective elasticity tensor for the macro stenting structure and modified permeability tensor for the macro stent structure filled with fluid.

5.3.1 Homogenization of elasticity

The micro design domain consists of solid and fluid material. When performing the numerical homogenization method for the stenting microstructure, the solid material has normal material properties, while the stiffness of the fluid material is weighted by a small positive number to avoid the singularity of the element stiffness matrix. The effective elasticity tensor $\mathbf{D}^{\mathrm{H}}$ of the stent in the macroscale can be obtained by the linear elasticity law, as seen in the Eq. (5-10).

$$\boldsymbol{\sigma} = \mathbf{D}^{\mathrm{H}}\boldsymbol{\varepsilon} \tag{5-10}$$

where $\boldsymbol{\sigma}$ and $\boldsymbol{\varepsilon}$ are the stress and strain fields of the macroscopic stenting structure, respectively. The effective elasticity tensor D_{ijkl}^{H} can be calculated in the 2D micro design domain via numerical homogenization, as the following:

$$D_{ijkl}^{\mathrm{H}} = \frac{1}{|Y|}\int_{Y}\left(\varepsilon_{pq}^{0(ij)} - \varepsilon_{pq}^{*(ij)}\right)D_{pqrs}\left(\varepsilon_{pq}^{0(kl)} - \varepsilon_{pq}^{*(kl)}\right)dY \tag{5-11}$$

where Y is the micro design domain and denotes one unit cell of the stent, and $|Y|$ is the area of the cell. i, j, k, l=1, 2. D_{pqrs} is the elasticity tensor of the solid material in the design domain. $\varepsilon_{pq}^{0(ij)}$ is the test unit strain field, where $(1,0,0)^T$, $(0,1,0)^T$ and $(0,0,1)^T$ are usually used in 2D models; $\varepsilon_{pq}^{*(ij)}$ is the locally varying strain fields and defined by:

$$\varepsilon_{pq}^{*(ij)} = \frac{1}{2}\left(\frac{\partial u_p^{ij}}{\partial y_q} + \frac{\partial u_q^{ij}}{\partial y_p}\right) \tag{5-12}$$

By assuming the virtual displacement field $v^{(kl)}$ in $U_p(Y)$, the kinematically admissible displacement space comprised of periodic Y, the displacement field $u^{(ij)}$ can be calculated via FEA by applying the periodic boundary conditions for the unit cell, as following:

$$\int_{Y}\left(\varepsilon_{pq}^{0(ij)} - \varepsilon_{pq}^{*(ij)}\left(u^{(ij)}\right)\right)D_{pqrs}\varepsilon_{rs}^{*(kl)}\left(v^{(kl)}\right)dY = 0, \ \forall \ v^{(kl)} \in U_{p}\left(Y\right) \qquad (5\text{-}13)$$

The 2D biomaterial with square elastic symmetry is considered in the model. However, some desired performances of the stent in both mechanical and fluid aspects may achieve a stenting layout with different properties in longitudinal and circumferential directions, for example, no foreshortening when stent expanding, and struts orientated to flow direction leading to a reduction of transverse flow. Therefore, it is defined that the effective stiffness matrix of the material has four independent components where the two Young's modulus in the two main directions, as the following form:

$$D^{\mathrm{H}} = \begin{bmatrix} D_{11}^{\mathrm{H}} & D_{12}^{\mathrm{H}} & 0 \\ D_{12}^{\mathrm{H}} & D_{22}^{\mathrm{H}} & 0 \\ 0 & 0 & D_{33}^{\mathrm{H}} \end{bmatrix} \qquad (5\text{-}14)$$

The auxetic properties can be obtained by the design of negative Poisson's ratios(NPR). Hence, two Poisson's ratios *Mu1* and *Mu2* in two directions are defined for the related design objectives in this study, and the calculations of the two Poisson's ratios are shown in Eq. (5-15).

$$\begin{cases} Mu1 = D_{12}^{\mathrm{H}}\big/D_{11}^{\mathrm{H}} \\[2mm] Mu2 = D_{12}^{\mathrm{H}}\big/D_{22}^{\mathrm{H}} \end{cases} \qquad (5\text{-}15)$$

5.3.2 Homogenization of modified fluid permeability (MFP)

A typical permeability in fluid mechanics is usually used to quantify the ability of a porous material to allow fluids to pass through it. The permeability of a porous medium is mainly determined by the porosity, pore shapes, and their distributions. In other words,

the medium with higher permeability can allow the fluid more easily and rapidly to move through it. As for minimizing the stenting hemodynamic alterations, the fact of the related optimization is to reduce the obstructions of stents on the blood flow. Thus, permeability can also be applied to measure this obstruction from the stent. Since blood flow is on the top of the stent layer, not across through the stent region, as shown in Figure 5-2, a modified permeability (MFP) is proposed to quantify stenting obstructions. At first, a typical permeability in fluid mechanics is presented, and then the MFP is following derived.

The homogenization method applied in the Stokes equations can derive Darcy's law to describe an incompressible viscous fluid through a porous medium from the macroscopic [195], where the derived Darcy's law is typically given by:

$$\mathbf{U} = -\frac{1}{\mu}\mathbf{K}^{\mathrm{H}}\left(\nabla p - \mathbf{f}\right) \qquad (5\text{-}16)$$

where $\mathbf{U}$ is the vector of average velocities. μ and $\mathbf{f}$ are the viscosity and the external body force, respectively. ∇p is the pressure gradient. $\mathbf{K}^{\mathrm{H}}$ is the effective permeability tensor and can be numerically computed in the microstructure via the homogenization method [152]; the calculation of a typical permeability can be formulated as:

$$\mathbf{K}^{\mathrm{H}} = \left[K_{\mathrm{ij}}^{\mathrm{H}}\right] = \frac{1}{|Y|}\left(\mathbf{w}^{(i)}\right)^{T}\mathbf{K}_{\mathrm{ds}}\mathbf{w}^{(j)} \qquad (5\text{-}17)$$

where the effective permeability tensor $\mathbf{K^H}$ is assembled by the components $K_{\mathrm{ij}}^{\mathrm{H}}$ along the main direction. $\mathbf{w}$ is the velocity vector solved in the above Darcy-Stokes coupling system for the microstructure via Eq. (5-8). $\mathbf{K_{ds}}$ is the Darcy-Stokes viscosity matrix defined in Eq. (5-9).

After that, a modified permeability tensor is proposed for the 2D design domain. The formulation of the modified permeability can be derived from the Eq. (5-17) and defined as:

$$\mathbf{K}_{2\mathrm{D}}^{\mathrm{H}} = \left[K_{2\mathrm{D}(ij)}^{\mathrm{H}} \right] = \frac{1}{\left| Y_{2D} \right|} \left(\mathbf{w}_{2D}^{(i)} \right)^{T} \mathbf{K}_{\mathrm{ds}}^{2\mathrm{D}} \mathbf{w}_{2D}^{(j)} \tag{5-18}$$

where the subscript '2D' denotes the extracted 2D design domain. $\mathbf{K}_{2\mathrm{D}}^{\mathrm{H}}$ is the modified effective permeability tensor. $\mathbf{w}_{2\mathrm{D}}$ is the velocity vector at the 2D design domain extracted from $\mathbf{w}$, which is calculated in the 3D computational domain. $\mathbf{K}_{\mathrm{ds}}^{2\mathrm{D}}$ is the Darcy-Stokes viscosity matrix defined for the 2D design domain and derived from the mixed viscosity matrix $\mathbf{K}_{\mathrm{ds}}$. The velocity vector $\mathbf{w}_{2\mathrm{D}}$ contains two directional components: one is along the blood flow direction, and another one is vertical to the blood flow, so the components in the modified permeability are associated with these two directions in the design domain. Hence, the effect of the stenting obstruction can be reduced by restricting the permeability value in the vertical direction to facilitate blood flow in the main direction. And then, the purpose of hemodynamic optimization for the stent can be achieved.

5.4 Optimization model and sensitivity analysis

In order to perform the proposed multiscale multi-objective topology optimization design for the stent, the numerical model should be established, where the relationship between the optimization objectives and the design variables needs to be derived. As discussed, the computational and design domains are different, so the different objectives have different associations with the design variables. They will be presented in the following.

The design objectives in respect of mechanics are auxetic properties and stent stiffness or

compliance. Since the stent is assumed as a straight body with constant thickness, both mechanical objectives can be equivalently evaluated by the horizontal cross-section profile of the stent. Hence, these two objectives can be directly obtained in the 2D design domain. However, in respect of the hemodynamic objective, the MFP needs to be calculated in the 3D computational domain. Thus, the related 3D CFD model should first be established based on the updated design variables in the 2D design domain. After that, the association between the hemodynamic objective and design variables can be built, and the related sensitivity analysis can be further derived.

5.4.1 Optimization model

The numerical optimization design starts from the initialization in the 2D design domain, the boundary of the design domain is parametrized by the level set function, and the expansion coefficients of the CS-RBF interpolation in the level set function (the implicit design variables) are defined, which can be used to determine the structure shape and topology. Then, the three objectives will be computed in two aspects simultaneously. In respect of mechanical objectives, the effective elasticity tensor of the microstructure is calculated by the numerical homogenization method, and the Poisson's ratios are the following obtained. Besides that, the macroscopic compliance of the stent can also be computed by the homogenized elasticity tensor. In respect of the fluid design objective, the 3D computational domain is firstly established based on the initial 2D design domain, where the material distribution of the 3D microstructure of the stent is determined by the 2D profile in the design domain, and the surrounding blood regions are specified same as the initial definition in Figure 5-2. Thus, the computational domain is solved by the coupled Darcy-Stokes system, and the velocity vector of the 3D fluid model is achieved.

After that, the velocity field of the 2D design domain is extracted from the 3D fluid model to calculate the modified permeability. Until now, all three objectives and related sensitivities are obtained. They are then normalized and assembled by weight factors. Based on the sensitivity of the assembled objectives, the OC method is used to update the expansion coefficients of PLSM to get a new structure layout. The proposed multiscale topology optimization model for the microstructure of the stent is formulated as:

$$
\begin{cases}
Find \quad \alpha_{2D,n}^{MI}\left(n=1,2,\dots,N\right) \\[2mm]
Min \quad J\left(\alpha_{2D}^{MI}\right)=W_I J_A^{MI}\left(\alpha_{2D}^{MI}\right)+W_2 J_P^{MI}\left(\alpha_{2D}^{MI}\right)+W_3 J^{MA}\left(\alpha_{2D}^{MI}\right) \\[2mm]
\qquad = W_I\left(\left(Mu1\left(\alpha_{2D}^{MI}\right)+1\right)^2+\left(Mu2\left(\alpha_{2D}^{MI}\right)+1\right)^2\right)+W_2\left(\mathbf{K}_{2D}^{H(2,2)}\left(\alpha_{2D}^{MI}\right)\right) \\[2mm]
\qquad +W_3\left(\dfrac{1}{2}\int_{\Omega_{2D}^{MA}}\varepsilon_{ij}^T\left(u_{2D}^{MA}\right)D_{ijkl}^H\left(\alpha_{2D}^{MI}\right)\varepsilon_{kl}\left(u_{2D}^{MA}\right)d\Omega_{2D}^{MA}\right) \\[2mm]
S.t. \quad V\left(\alpha_{2D}^{MI}\right)=\int_{\Omega^{MI}}H\left(\Phi^{MI}\left(\alpha_{2D}^{MI}\right)\right)d\Omega_{2D}^{MI}-V_{2D}^{max}\le 0 \\[2mm]
\qquad F_{2D}^{MI}\left(u_{2D}^{MI},w_{2D}^{MI},\alpha_{2D}^{MI}\right)=L_{2D}^{MI}\left(w_{2D}^{MI},\alpha_{2D}^{MI}\right),\forall\,w_{2D}^{MI}\in\overline{U}\left(\Omega_{2D}^{MI}\right) \\[2mm]
\qquad F_{3D}^{MI}\left(u_{3D}^{MI},p_{3D}^{MI},v_{3D}^{MI},q_{3D}^{MI},\alpha_{2D}^{MI}\right)=L_{3D}^{MI}\left(v_{3D}^{MI},q_{3D}^{MI}\right),\forall\,v_{3D}^{MI},q_{3D}^{MI}\in\overline{U}\left(\Omega_{3D}^{MI}\right) \\[2mm]
\qquad F_{2D}^{MA}\left(u_{2D}^{MA},w_{2D}^{MA},D_{ijkl}^H\right)=L_{2D}^{MA}\left(w_{2D}^{MA}\right),\forall\,w_{2D}^{MA}\in\overline{U}\left(\Omega_{2D}^{MA}\right) \\[2mm]
\qquad \alpha_{2D,min}^{MI}\le\alpha_{2D,n}^{MI}\le\alpha_{2D,max}^{MI}
\end{cases}
\tag{5-19}
$$

where the superscript "*MA*" denotes the parameters in the macro scale, and "*MI*" in the microscale; the subscript "*2D*" denotes the parameters in the 2D micro design domain, and "*3D*" in the 3D computational domain. N is the total number of fixed knots in the 2D micro design domain. The expansion coefficients of the CSRBF interpolation $\alpha_{2D,n}^{MI}$ are the design variables in the design domain, ranging between $\alpha_{2D,min}^{MI}$ and $\alpha_{2D,max}^{MI}$. J is the equivalent objective function, comprised of the micro auxetic property(Poisson's ratios) J_A^{MI}, MFP J_P^{MI}, and macro compliance J^{MA}, where W_1, W_2, W_3 are corresponding weight factors, and the sum of them equals to "1". The subscript "*A*" and "*P*" denote auxetic and permeability, respectively. $\mathbf{K}_{2D}^H$ is the MFP, and $\mathbf{K}_{2D}^{H(2,2)}$ denotes the components in the

vertical direction. V is the volume constraint, and the upper limit is defined as V_{2D}^{max}. The volume constraint is applied to the 2D micro design domain. It can also be transformed as the constraint for the 3D computational to control the 3D microstructure volume. The details of the equations for the bilinear energy F and the linear load L will be given in the following. H in the volume constraint is the Heaviside function used to denote void and solid material in the 2D design domain, and also used to identify fluid and solid in the 3D computational model, given by:

$$H\left(\Phi_{2D}^{MI}\right)=\begin{cases}\Theta & \Phi_{2D}^{MI}<-\varDelta \\ \dfrac{3(1-\Theta)}{4}\left(\dfrac{\Phi_{2D}^{MI}}{\varDelta}-\dfrac{\left(\Phi_{2D}^{MI}\right)^{3}}{\varDelta^{3}}\right)+\dfrac{1+\Theta}{2} & -\varDelta\leq\Phi_{2D}^{MI}\leq\varDelta \\ 1 & \Phi_{2D}^{MI}>\varDelta\end{cases} \tag{5-20}$$

where Θ is a small positive number to avoid the singularity of the element stiffness matrix when calculating the mechanical properties for the stent structure, but it becomes zero when doing CFD in the computational design domain and denotes fluid material. $\varDelta$ is the width for the numerical approximation of H. δ is the Dirac function, the derivative of the Heaviside function H. It will be used for the sensitivity analysis for the numerical optimization model and can be described as:

$$\delta\left(\Phi_{2D}^{MI}\right)=\begin{cases}\dfrac{3(1-\Theta)}{4\varDelta}\left(1-\dfrac{\left(\Phi_{2D}^{MI}\right)^{2}}{\varDelta^{2}}\right) & \left|\Phi_{2D}^{MI}\right|\leq\varDelta \\ 0 & \left|\Phi_{2D}^{MI}\right|>\varDelta\end{cases} \tag{5-21}$$

The MFP in the design model related to the design variables can be obtained by:

$$\mathbf{K}_{2D}^{H}\left(\alpha_{2D}^{MI}\right)=\left[K_{2D(ij)}^{H}\left(\alpha_{2D}^{MI}\right)\right]=\dfrac{1}{\left|\Omega_{2D}^{MI}\right|}\left(\mathbf{w}_{2D}^{(i)}\right)^{T}\mathbf{K}_{ds}^{2D}\left(H^{f}\left(\Phi_{2D}^{MI}\left(\alpha_{2D}^{MI}\right)\right)\right)\mathbf{w}_{2D}^{(j)} \tag{5-22}$$

where the velocity vector $\mathbf{w}_{2D}$ is extracted from the velocity vector $\mathbf{u}_{3D}^{MI}(u_{3D}^{MI})$, which is calculated using the following momentum equation in the 3D computational domain.

$$F_{3D}^{MI}\left(u_{3D}^{MI}, p_{3D}^{MI}, v_{3D}^{MI}, q_{3D}^{MI}, \alpha_{2D}^{MI}\right) = L_{3D}^{MI}\left(v_{3D}^{MI}, q_{3D}^{MI}\right) \tag{5-23}$$

where v_{3D}^{MI} and p_{3D}^{MI} are the boundary conditions defined by the blood flow through the stent. The momentum equation (5-23) can be rewritten by a matrix form and given by:

$$\begin{bmatrix} \mathbf{K}_{ds}\left(H^f\right) & -\mathbf{G}_{ds}\left(H^f\right) \\ \mathbf{G}_{ds}^{T}\left(H^f\right) & \mathbf{M}_{ds}\left(H^f\right) \end{bmatrix} \begin{bmatrix} \mathbf{u}\left(u_{3D}^{MI}\right) \\ \mathbf{p}\left(p_{3D}^{MI}\right) \end{bmatrix} = \begin{bmatrix} \mathbf{F}_{ds}\left(w_{3D}^{MI}\right) \\ \mathbf{H}_{ds}\left(q_{3D}^{MI}\right) \end{bmatrix} \tag{5-24}$$

where H^f denotes the Heaviside function H applied to the Darcy-Stokes coupling in the CFD model, and Θ in H^f is equal to zero to identify fluid material in the design domain. The effective elasticity tensor D_{ijkl}^{H} used for the evaluation of the mechanical properties in the optimization model can be calculated by:

$$D_{ijkl}^{H}\left(\alpha_{2D}^{MI}\right) = \frac{1}{\left|\Omega_{2D}^{MI}\right|} \int_{\Omega_{2D}^{MI}} \left(\varepsilon_{pq}^{0(ij)} - \varepsilon_{pq}^{*}\left(u_{2D}^{(ij)}\right)\right) D_{pqrs} \left(\varepsilon_{rs}^{0(kl)} - \varepsilon_{rs}^{*}\left(u_{2D}^{(kl)}\right)\right) H\left(\Phi_{2D}^{MI}\left(\alpha_{2D}^{MI}\right)\right) d\Omega_{2D}^{MI} \tag{5-25}$$

where D_{pqrs} is the elasticity tensor of the solid material; ε_{pq}^{0} is the test unit strain field, $(1,0,0)^T$, $(0,1,0)^T$ and $(0,0,1)^T$ as for the 2D problem; ε_{pq}^{*} is the strain field related to the displacement u_{2D}, which can be calculated via finite element analysis using the periodic boundary conditions of the microstructure in the design domain:

$$\int_{\Omega_{2D}^{MI}} \left(\varepsilon_{pq}^{0(ij)} - \varepsilon_{pq}^{*}\left(u_{2D}^{MI(ij)}\right)\right) D_{pqrs}\varepsilon_{rs}^{*}\left(w_{2D}^{MI(kl)}\right) H\left(\Phi_{2D}^{MI}\right) d\Omega_{2D}^{MI} = 0, \ \forall \, w \in \bar{U}\left(\Omega_{2D}^{MI}\right) \tag{5-26}$$

where w is the virtual displacement field. The bilinear energy and the linear load forms of the finite element analysis in the design domain can be described as:

$$F_{2D}^{MI}\left(u_{2D}^{MI}, w_{2D}^{MI}, \alpha_{2D}^{MI}\right) = \int_{\Omega_{2D}^{MI}} \varepsilon_{ij}^*\left(u_{2D}\right) D_{pqrs} \varepsilon_{kl}^*\left(w_{2D}^{MI}\right) H\left(\Phi_{2D}^{MI}\left(\alpha_{2D}^{MI}\right)\right) d\Omega_{2D}^{MI} \qquad (5\text{-}27)$$

$$L_{2D}^{MI}\left(w_{2D}^{MI}, \alpha_{2D}^{MI}\right) = \int_{\Omega_{2D}^{MI}} \varepsilon_{ij}^{0(ij)}\left(u_{2D}\right) D_{pqrs} \varepsilon_{kl}^*\left(w_{2D}^{MI}\right) H\left(\Phi_{2D}^{MI}\left(\alpha_{2D}^{MI}\right)\right) d\Omega_{2D}^{MI} \qquad (5\text{-}28)$$

The bilinear energy and the linear load forms in the 2D macroscale can be computed by:

$$F_{2D}^{MA}\left(u_{2D}^{MA}, w_{2D}^{MA}, D_{ijkl}^H\right) = \int_{\Omega_{2D}^{MA}} \varepsilon_{ij}\left(u_{2D}^{MA}\right) D_{ijkl}^H \varepsilon_{kl}\left(w_{2D}^{MA}\right) d\Omega_{2D}^{MA} \qquad (5\text{-}29)$$

$$L_{2D}^{MA}\left(w_{2D}^{MA}\right) = \int_{\Omega_{2D}^{MA}} p w_{2D}^{MA} d\Omega_{2D}^{MA} + \int_{\Omega_{2D}^{MA}} \tau w_{2D}^{MA} d\Gamma_{2D}^{MA} \qquad (5\text{-}30)$$

where p is the body force, and τ is the traction of the boundary Γ_{2D}^{MA} in the 2D macroscale.

5.4.2 Sensitivity analysis

The sensitivities of the objective functions can be derived to quantify small perturbations of the design variables on the values of the objective functions. It supports updating algorism in the optimization model to alter the structural material layout in the design domain to obtain the desired objectives.

Based on the topology optimization model established in the Eq. (5-19), the sensitivities of three objective functions can be calculated, respectively, via the first-order derivatives of the objective functions with respect to the expansion coefficients α_{2D}^{MI}. The sensitivity of the macro compliance of the stent in the macroscale is computed by:

$$\frac{\partial J^{MA}}{\partial \alpha_{2D}^{MI}} = \frac{1}{2} \int_{\Omega_{2D}^{MA}} \varepsilon_{ij}^T\left(u_{2D}^{MA}\right) \frac{\partial D_{ijkl}^H\left(\alpha_{2D}^{MI}\right)}{\partial \alpha_\xi^{MI}} \varepsilon_{kl}\left(u_{2D}^{MA}\right) d\Omega_{2D}^{MA} \qquad (5\text{-}31)$$

Based on the shape derivative, the first-order derivatives of the effective elasticity tensor D_{ijkl}^H with respect to the pseudo time t is:

$$\frac{\partial D_{ijkl}^{H}}{\partial t} = \frac{1}{\left|\Omega_{2D}^{MI}\right|} \int_{\Omega_{2D}^{MI}} \beta_{2D}^{MI} v^{n} \left|\left(\nabla \Phi_{2D}^{MI}\right)^{T}\right| \delta\left(\Phi_{2D}^{MI}\right) d\Omega_{2D}^{MI} \tag{5-32}$$

$$\beta_{2D}^{MI} = \left(\varepsilon_{pq}^{0(ij)} - \varepsilon_{pq}^{*}\left(u_{2D}^{MI(ij)}\right)\right) D_{pqrs} \left(\varepsilon_{rs}^{0(kl)} - \varepsilon_{rs}^{*}\left(u_{2D}^{MI(kl)}\right)\right) \tag{5-33}$$

v^{n} can be determined in the parametric level set function that can be referred to the discussion in Chapter 3 and substituted in Eq. (5-32):

$$\frac{\partial D_{ijkl}^{H}}{\partial t} = \left(\frac{1}{\left|\Omega_{2D}^{MI}\right|} \int_{\Omega_{2D}^{MI}} \beta_{2D}^{MI} \varphi_{2D}^{MI}(x)^{T} \delta\left(\Phi_{2D}^{MI}\right) d\Omega_{2D}^{MI}\right) \dot{\alpha}_{2D,n}^{MI}(t) \tag{5-34}$$

The first-order derivatives of D_{ijkl}^{H} with respect to t can also be obtained by the chain rule:

$$\frac{\partial D_{ijkl}^{H}}{\partial t} = \frac{\partial D_{ijkl}^{H}}{\partial \alpha_{2D}^{MI}} \dot{\alpha}_{2D,n}^{MI}(t) \tag{5-35}$$

Comparing Eq. (5-34) and (5-35), the first-order derivatives of D_{ijkl}^{H} with respect to the expansion coefficients α_{2D}^{MI} can be obtained as:

$$\frac{\partial D_{ijkl}^{H}}{\partial \alpha_{2D}^{MI}} = \frac{1}{\left|\Omega_{2D}^{MI}\right|} \int_{\Omega_{2D}^{MI}} \beta_{2D}^{MI} \varphi_{2D}^{MI}(x)^{T} \delta\left(\Phi_{2D}^{MI}\right) d\Omega_{2D}^{MI} \tag{5-36}$$

Therefore, the sensitivity of the objective J^{MA} can be achieved by substituting Eq. (5-36) into (5-31). Since the sensitivity of the objective J_{A}^{MI} is also based on Eq. (5-36), it can be calculated by:

$$\frac{\partial J_{A}^{MI}}{\partial \alpha_{2D}^{MI}} = \frac{\partial \left(Mu1+1\right)^{2}}{\partial \alpha_{2D}^{MI}} + \frac{\partial \left(Mu2+1\right)^{2}}{\partial \alpha_{2D}^{MI}} = \frac{\partial \left(D_{12}^{H}/D_{11}^{H}+1\right)^{2}}{\partial \alpha_{2D}^{MI}} + \frac{\partial \left(D_{12}^{H}/D_{22}^{H}+1\right)^{2}}{\partial \alpha_{2D}^{MI}} \tag{5-37}$$

The sensitivity of the MFP can be derived for the Darcy-Stokes coupling system in the 3D computational domain, so the first-order derivatives of $\mathbf{K}_{2D}^{H}$ with respect to the

expansion coefficients α_{2D}^{MI} can be given by:

$$\frac{\partial J_P^{MI}}{\partial \alpha_{2D}^{MI}} = \frac{\partial \mathbf{K}_{2D}^{\mathrm{H}(2,2)}\left(\alpha_{2D}^{MI}\right)}{\partial \alpha_{2D}^{MI}} \tag{5-38}$$

where the sensitivity of the MFP can be further calculated by the application of the Heaviside function H^f in the fluid-solid coupling system:

$$\begin{aligned}
\frac{\partial \mathbf{K}_{2D}^{\mathrm{H}}\left(\alpha_{2D}^{MI}\right)}{\partial \alpha_{2D}^{MI}} &= \frac{1}{\left|\Omega_{2D}^{MI}\right|}\left(\mathbf{w}_{2D}^{(i)}\right)^T \frac{\partial \mathbf{K}_{ds}^{2D}\left(\alpha_{2D}^{MI}\right)}{\partial \alpha_{2D}^{MI}}\left(H^f\left(\Phi_{2D}^{MI}\left(\alpha_{2D}^{MI}\right)\right)\right)\mathbf{w}_{2D}^{(j)} \\
&= \frac{1}{\left|\Omega_{2D}^{MI}\right|}\int_{\Omega_{2D}^{MI}}\left(\mathbf{w}_{2D}^{(i)}\right)^T \varphi_{2D}^{MI}(x)^T \delta^f\left(\Phi_{2D}^{MI}\right)\left(\mathbf{K}_d^{2D} - \mathbf{K}_s^{2D}\right)\mathbf{w}_{2D}^{(j)}d\Omega_{2D}^{MI}
\end{aligned} \tag{5-39}$$

As discussed, the volume constraint is only defined in the 2D design domain, which can further control the 3D microstructural volume. Hence, the sensitivity of the volume constraint can be only considered in the design domain and calculated by:

$$\frac{\partial V}{\partial \alpha_{2D}^{MI}} = \int_{\Omega_\xi^{MI}} \varphi_{2D}^{MI}(x)^T \delta\left(\Phi_{2D}^{MI}\left(\alpha_{2D}^{MI}\right)\right)d\Omega_{2D}^{MI} \tag{5-40}$$

After that, all the sensitivities of the three objective functions are obtained. The non-dimensional sensitivities are calculated by Eq. (5-41) and assembled by the specified weight factors, which is advantageous to the sensitivity of the original objective in multi-objective optimization issues [196].

$$\partial J_i^{non} = \frac{\partial J_i}{\left|\partial J_i^{\max}\right|} \quad i \in (1,2,3) \tag{5-41}$$

where i denotes the defined three objective functions.

5.4.3 Numerical Procedure

A flowchart of the multiscale multi-objective optimization model is created to illustrate the numerical procedure, as shown in Figure 5-3. The numerical topology optimization is simultaneously performed in multiscale. It starts from the initialization in the 2D design domain to define the design variables. By applying the numerical homogenization method in the design domain, the micro displacement field u_{2D}^{MI} is calculated in Eq. (5-27). The effective elasticity tensor D_{ijkl}^{H} can be further obtained in Eq. (5-25) based on the test strain field and u_{2D}^{MI}. After that, the objective function J_{A}^{MI} is calculated, and the related sensitivity can also be computed in Eq. (5-37). On the other hand, the homogenized effective elasticity tensor is transferred into the 2D macroscale. By using D_{ijkl}^{H}, the macro displacement filed u_{2D}^{MA} is calculated, and the macroscopic compliance J^{MA} is following obtained. Then, the sensitivity of J^{MA} is derived in the Eq. (5-31). At the initialization stage, the 3D computational domain for the stenting microstructure is simultaneously established based on the initial design variables. The velocity filed u_{3D}^{MI} is computed via the Darcy-Stoke coupling system in Eq. (5-24). Thus, the velocity field in the 2D design domain is extracted from u_{3D}^{MI}, and then the MFP $\mathbf{K}_{2D}^{H}$ of the 2D design domain can be calculated in Eq. (5-22). The related sensitivity is obtained in Eq. (5-39). Until now, all three objective functions and related sensitivities are achieved. In order to take advantage of each design objective function, three non-dimensional sensitivities for the objective functions are transformed in Eq. (5-41). Then, objective J and related non-dimensional sensitivity are assembled by weight factors, respectively. The design variables are then updated by adopting the OC method. The loop of the optimization is performed until the convergent criterion is satisfied.
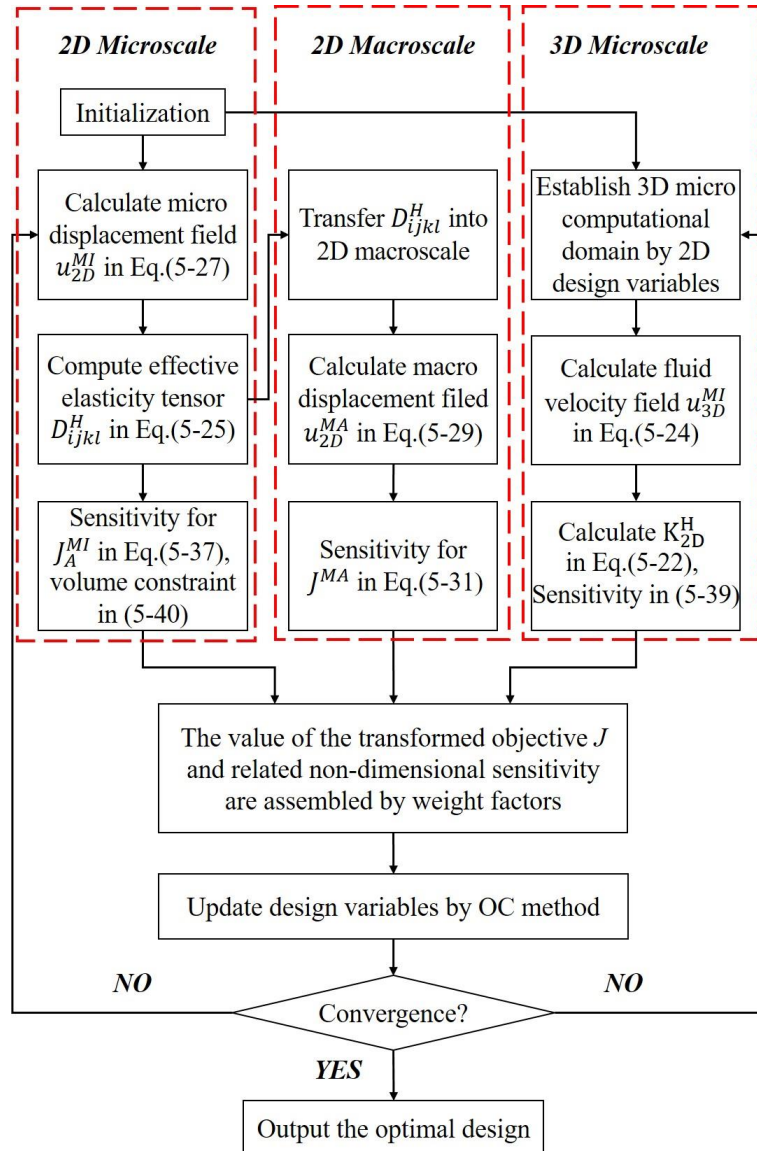
Figure 5-3 The flowchart of the topology optimization

5.5 Examples and discussion

The numerical optimization is implemented with software MATLAB 2018b to obtain the uniform microstructure for the stent. The multi-domain involved in the optimization model is illustrated in Figure 5-4.
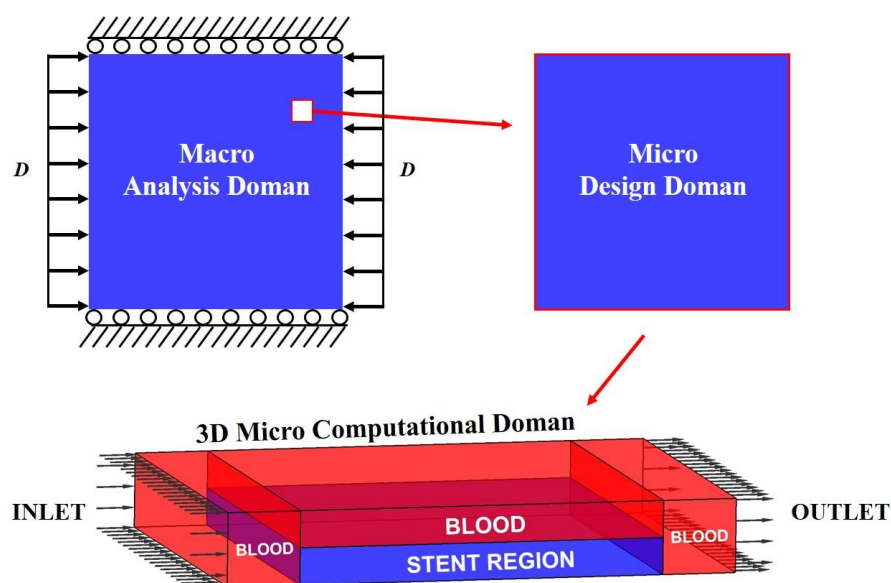
Figure 5-4 Multi-domain of the numerical model

From the figure, we can see three domains are defined in the model. The stent is expanded as a 2D structure defined as the macro analysis domain consisting of 20×20 uniform microstructures. The macrostructure of the stent subjects to the boundary and loading conditions, as shown in the figure. The vertical degree of freedoms of the stenting top and bottom edges are fixed, and horizontal unit displacements are applied on the left and right edges. One of the uniform stenting microstructures is then defined as the micro design domain regarded as the optimization design object. The micro design domain can be further treated as the constant 2D horizontal cross-section profile of a 3D stenting microstructure. Based on the 3D microstructure, a 3D micro computational field is established for the related CFD analysis. In that 3D domain, a scaled velocity of blood flow is specified as the inlet condition, while the zero pressure boundary is defined as the outlet condition. By considering the computational efficiency, a square element with four nodes is adopted to discretize the 2D micro design and macro analysis domains. In contrast, an 8-node brick element is used in the 3D micro computational field.

In the optimization model, the multi-objective is obtained by three weighted optimization objectives. Various combinations of the three weight factors can lead to different results. Besides that, the contribution of each weighted objective to the optimization result is also unknown. Hence adoptions of the three weight factors should be investigated. Some structural characteristics as the following can be utilized to evaluate the impacts of the three optimization objectives on the optimization results:

a) The MFP optimization aims to reduce the vertical flow to facilitate blood flow through the stented segment. Hence, more contributions to the optimization will lead to fewer obstructions along the flow direction.

b) The structure with auxetic properties exhibits NPR. Thus, more contributions to auxetic optimization leads to lower Poisson's ratios, presenting more significant degrees of re-entrant features, chiral characteristics with larger rotation angles, or the generation of thin connections between struts.

c) The larger weight factor for macroscopic compliance optimization leads to more material assigned along the direction of loads against the external deformation. Besides that, the consideration of macroscopic compliance can also lead to more uniform structures.

Since the adoptions of the weight factors and volume fraction can impact the optimization results, two kinds of studies are defined to investigate their influences. In the first study, the volume fraction is constant, and the combinations of the three weight factors are various. After the weight factors are determined in the first study, they will be used for the second study to investigate the impacts of different volume fractions.

5.5.1 Studies of three weight factors

In the first study, the volume fraction is specified as 30%. That is because stents with too much material can induce strong biological rejections and may block blood flow. Thus, stents usually have small volume fractions. Although there is no exact benchmark for the volume fraction, an approximate volume fraction in the first study is enough to investigate the influences of the weight factors. In the first study, three optimization series are established to analyze the contributions of the three weight factors to the optimization results. To identify the three series, the letter "A, B, C" are used. In each optimization series, eight cases are defined that the value of one weight factor is varied in a range from 10% to 80% while keeping equal amounts for others.
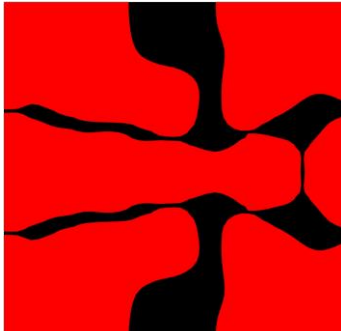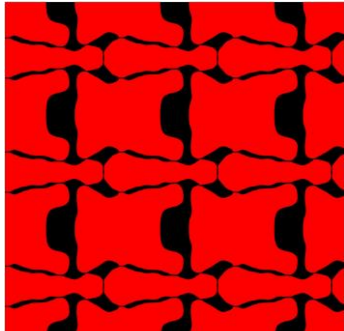
1) The results of varying W_3

W_3 is the weight factor for the optimization objective of macrostructural compliance. The optimization of varying W_3 in the range of 10 - 80% is defined as series A. The optimized microstructure and the related 3×3 arrays architecture in the 8 study cases are summarized in Table 5-1. As for each result, the design domain is filled with two material phases: the black colour denotes the solid material, and the red colour denotes the fluid. In order to identify different structural characteristics, the struts along the vertical direction are named vertical struts and orienting to the blood flow are named horizontal struts. For example, in case A-3, there three vertical struts and two horizontal struts.

In the results, the re-entrant features introduced by the auxetic optimization are formed to connect the struts when W_3 is less than 40%, but more weak connecting struts also occur as the decrease of W_3, such as the cases A-1, 2. These structures with thin struts cannot provide enough stiffness to support the arteries. In contrast, when W_3 is equal or greater

than 40%, nearly all material concentrates along the horizontal direction, the same direction of deformation condition, as shown in Figure 5-4. On the other hand, the MFP optimization can guide the material mostly assigned along the blood flow direction, leading to fewer obstructions. It can be found that all the results in the series A exhibit large fluid spaces in the middle regions of the microstructures and create openings in the inlet sides. All these structural characteristics can reduce obstacles to the blood flow. However, both the effects of W_2 and W_3 can lead the material to more consents to the horizontal struts. It cannot identify which one has more contributions to the optimized results. In series A, the different W3 results indicate a variation trend of the structure that the material in the design domain will concentrate along the vertical direction as the increase of W_3. Among that, the value of W_3 around 30% may obtain a structure with the uniform material distribution.

Table 5-1 The results of various weight factor W_3 in a range of (10-80%)

W_1-W_2-W_3 (%) (Series A)	Microstructure	Microstructure (3×3)
45-45-10 (A-1)		

40-40-20
(A-2)
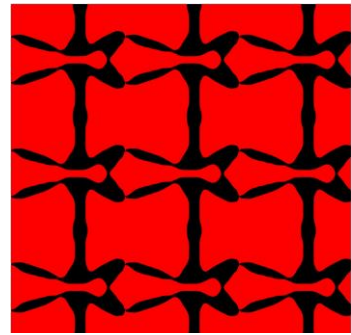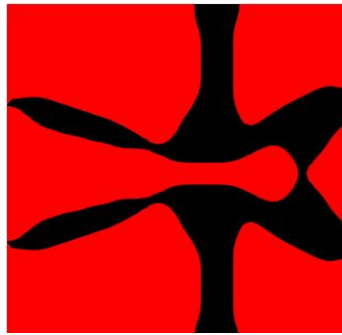
35-35-30
(A-3)
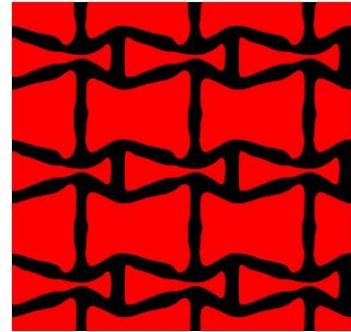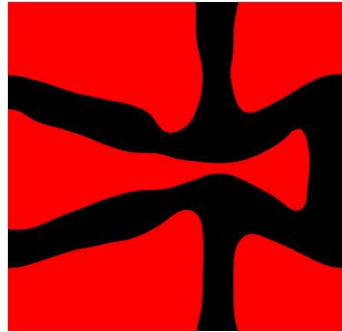
30-30-40
(A-4)
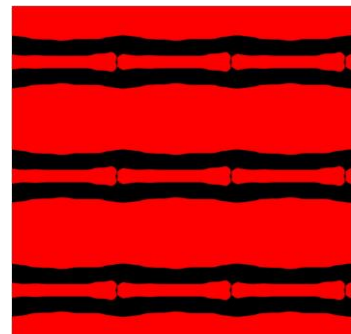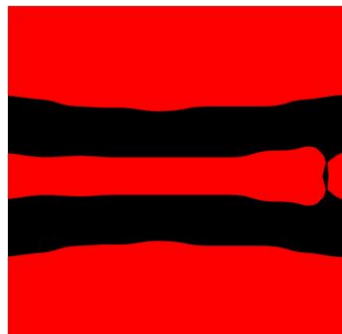
25-25-50
(A-5)

20-20-60
(A-6)

15-15-70 (A-7)		
10-10-80 (A-8)		
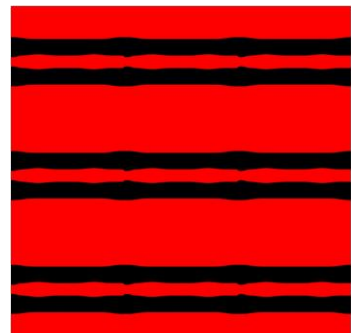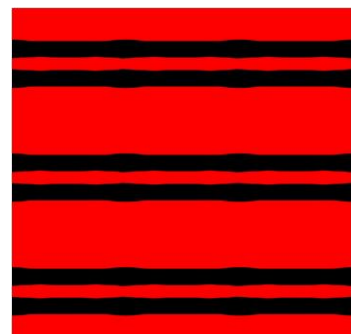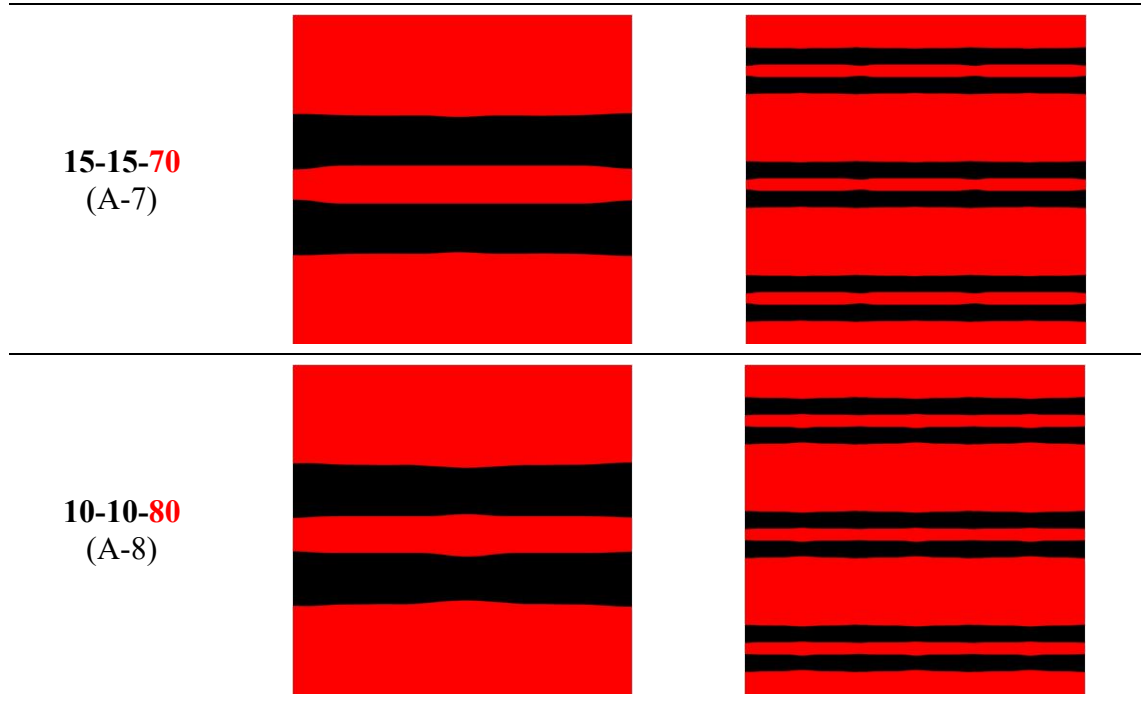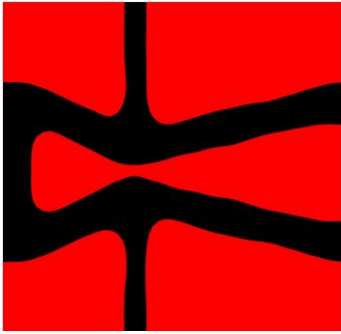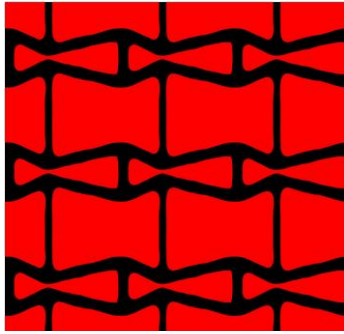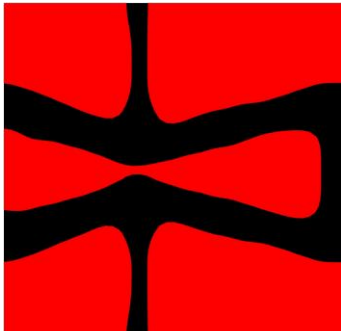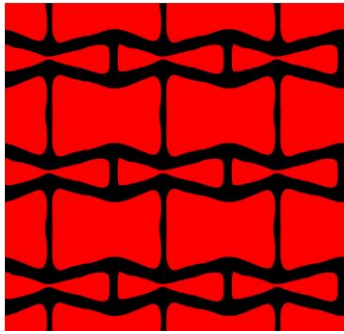
2) The results of varying W_2

W_2 is the weight factor for the optimization objective, the vertical MFP. The optimization of varying W_2 in the range of 10 - 80% is defined as series B. The optimized microstructure and the related 3×3 arrays architecture in the 8 study cases are presented in Table 5-2. The results show that the solid material concentrates more on the two horizontal struts as the increase of W_2. When W_2 is equal or greater than 40%, nearly all material is assigned to the horizontal struts. When W_2 is less than 40%, the vertical struts are formed under the impacts of W_1 and W_3, exhibiting re-entrant features and uniform material distributions. However, most vertical struts will gradually disappear as the increase of W_2.

Another significant effect of the design of MFP is that the positions of the vertical struts. Under the consideration of MFP, three vertical struts exist in the results of cases B1-3.

As the increase of W_2, the two vertical struts beside the horizontal struts will move from the left side to the right, resulting in a large fluid space behind the inlet side and facilitating blood flow. Only one connecting vertical strut exists between the two horizontal struts, which can significantly reduce the blood flow obstacles. On the other hand, the position of this short vertical strut only occurs in the inlet edge or outlet edge. Its position will finally move to the outlet edge as the increase of W_2, leading to an opening at the inlet. Overall, in series B, as the increase of W_2, the vertical struts will become thinner, and more solid material will be assigned along the flow direction. Most vertical struts will disappear when W_2 is equal to or greater than 40%.

Table 5-2 The results of various weight factor W_2 in a range of (10-80%)

W_1-W_2-W_3 (%) (Series B)	Microstructure	Microstructure (3×3)
45-10-45 (B-1)		
40-20-40 (B-2)		
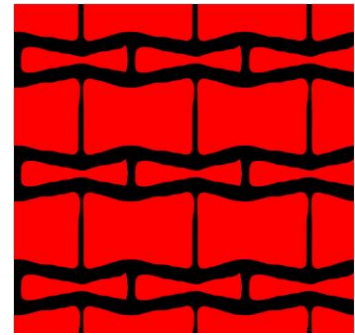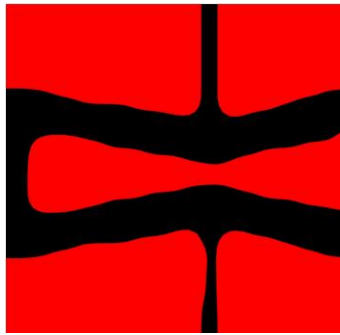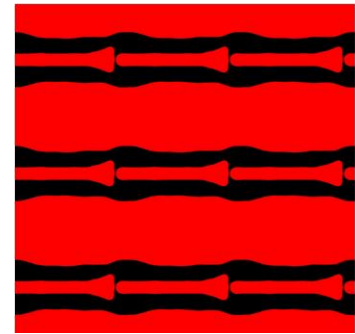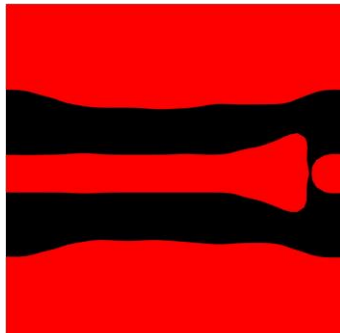
35-30-35 (B-3)		
30-40-30 (B-4)		
25-50-25 (B-5)		
20-60-20 (B-6)		
15-70-15 (B-7)		
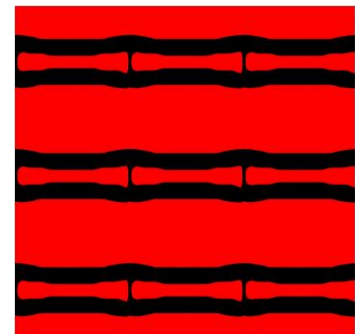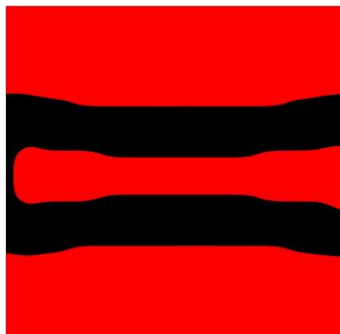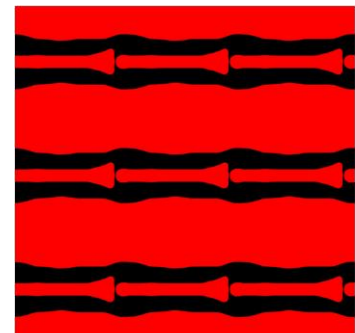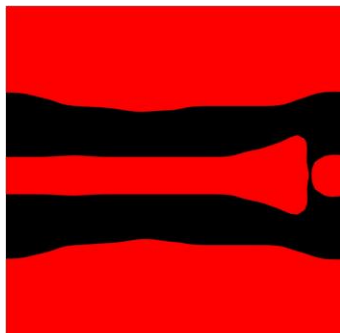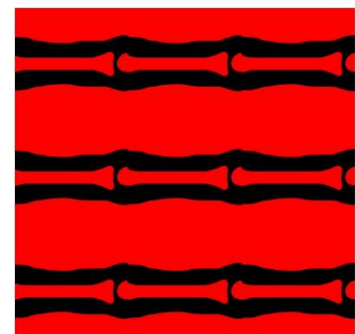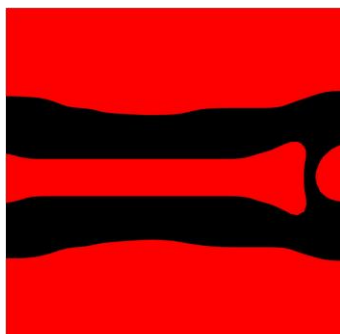
10-80-10 (B-8)		
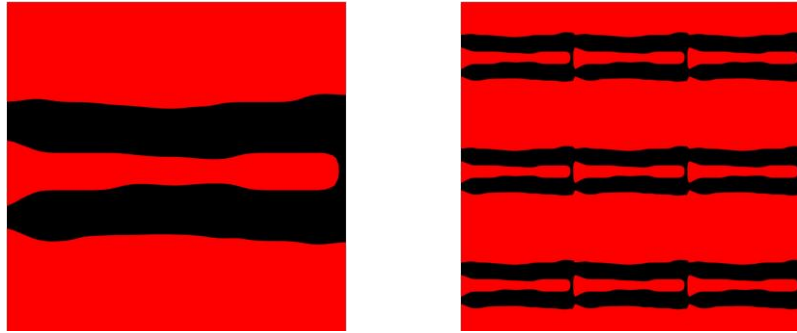
3) The results of varying W_1

W_1 is the weight factor for the auxetic optimization objective. The optimization of varying W_1 in the range of 10 - 80% is defined as series C. The optimized microstructure and the related 3×3 arrays architecture in the 8 study cases are presented in Table 5-3. In the table, when W_1 is less than W_2 and W_3, the solid material in the design domain is mainly assigned to the horizontal struts. When W_1 is greater than 30%, re-entrant features begin to be generated as the increase of W_1. When W_1 is equal to or greater than 50%, the topological changes of the structure begin to be driven by W_1 as its increase, exhibiting more thinner connecting struts appear in the optimized structures, such as the cases C-5 to C-8. Among the results, the case C-4 shows a balance between the three weight factors. In a word, in series C, when the factor greater than 30%, the structure gradually generates more features to enhance the property of NPR as the increase of W_1. However, more thin struts are formed when W_1 is equal to or greater than 50%.

Table 5-3 The results of various weight factor W_1 in a range of (10-80%)

W_1-W_2-W_3 (%) (Series C)	Microstructure	Microstructure (3×3)
10-45-45 (C-1)		
20-40-40 (C-2)		
30-35-35 (C-3)		
40-30-30 (C-4)		

50-25-25 (C-5)		
60-20-20 (C-6)		
70-15-15 (C-7)		
80-10-10 (C-8)		
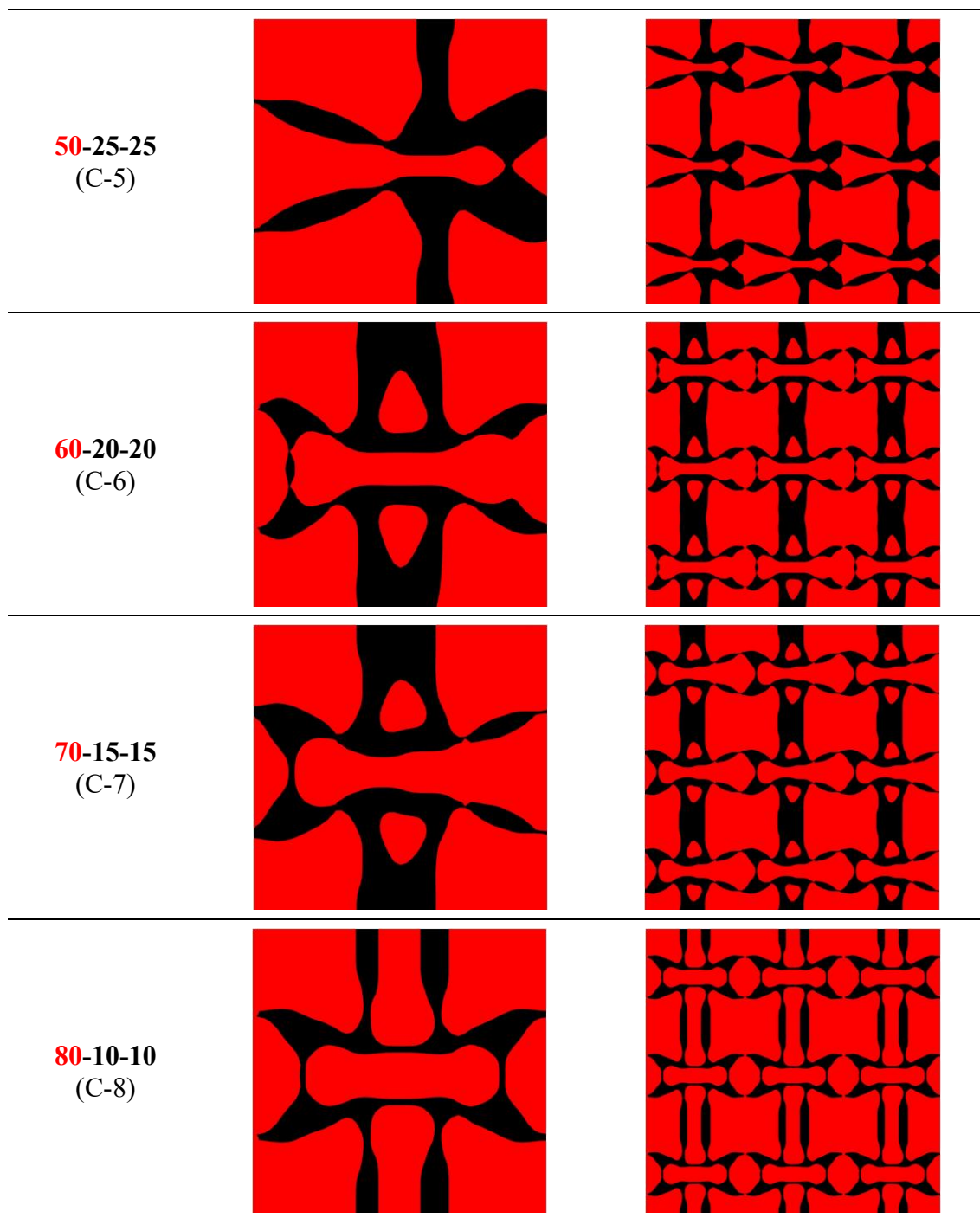
4) The results of varying combinations of W_1 and W_2

In the above three series studies of the weight factors, the impacts of the three optimization objectives on the structural changes can be summarized as follows. (1) The

optimization of auxetic properties introduces re-entrant features and thin connections. (2) The optimization of MFP leads to thinner vertical struts and drives the solid material to concentrate along the flow direction. (3) The design for the stenting macroscopic stiffness can concentrate the solid material along the load direction.

Among the results, when W_3 is greater than 30%, the solid material is mainly assigned to the horizontal struts, as shown in results A-4 to A-8, C-1 to C-3. However, when W_3 is less than 30%, the material distributions will become non-uniform and more thin connecting struts, such as the results A-1, A-2, C-5 to C-8. Thus, the value of W_3 equal to 30% may lead to more uniform material distributions, such as the results A-3 and C-4.
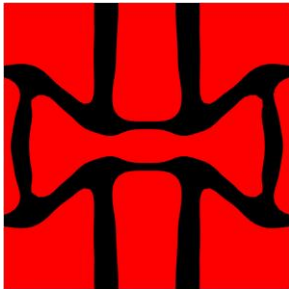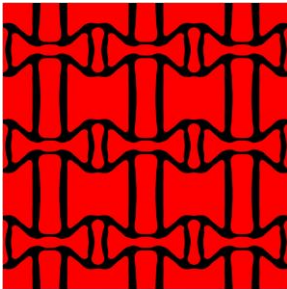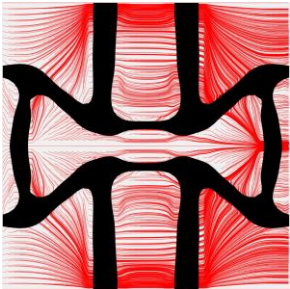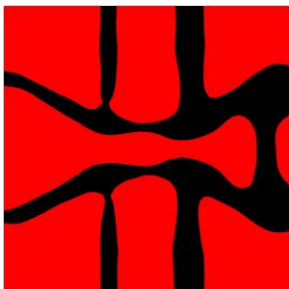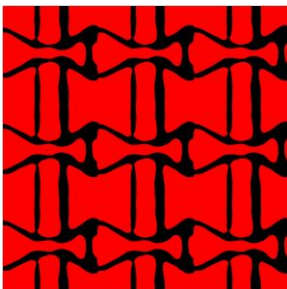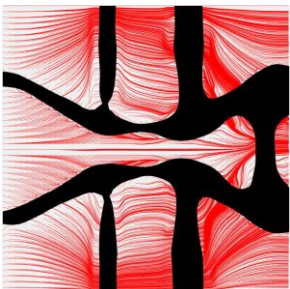
In respect of the MFP optimizations, the effects of W_2 are similar to W_3. Both of them can drive the material to be assigned to the horizontal struts. In series B, the trend of the structural changes may under the influences of both W_2 and W_3. The impacts of W_2 can be easily detected when it significantly larger than W_3. Thus, it is hard to determine the exact proper range for W_2.

As for the optimizations of auxetic properties, the related weight factor in a range between 30% and 50% exhibit uniform re-entrant features, as illustrated in the results A-3, B-1, B-2, C-4. However, when W_1 less than 30%, either W_2 or W_3 is greater than W_1. Any of the situations can lead to more material concentrate on the horizontal struts. On the other hand, when W_1 is greater than 50%, the value of W_3 is less than 30%. It is the reason why many thin struts appear in the results.

Therefore, the exact adoptions of the relevant weight factors W_1 and W_2 cannot be determined in the above studies. The fourth series study is established for varying the combinations of three weight factors W_1 and W_2 under the specified W_3 to investigate the

adoptions of W_1 and W_2. In order to facilitate the comparison of the optimization results, the same value of the volume fraction 30% is used in the fourth series study. The results of different combinations of the weight factors W_1 and W_2 are defined as series D and summarized in Table 5-4, where the microstructure of each case and the related 3×3 array structure are presented. In order to capture the impacts of various combinations of the weight factors on the blood flow, the streamlines generated by blood flow through the micro design domain are also provided in the table.

Table 5-4 The results(W_3=30%) of various weight factor W_1 and W_2

W_1-W_2-W_3 (%) (Series D)	Microstructure	Microstructure (3×3)	Streamline
70-**0**-**30** (D-1)			
65-**5**-**30** (D-2)			

60-**10**-**30**
(D-3)
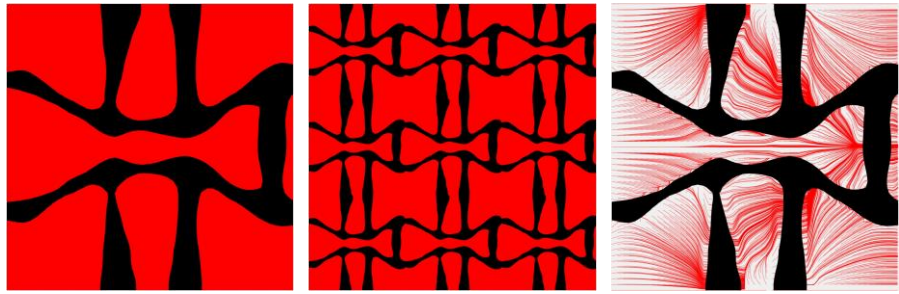
55-**15**-**30**
(D-4)
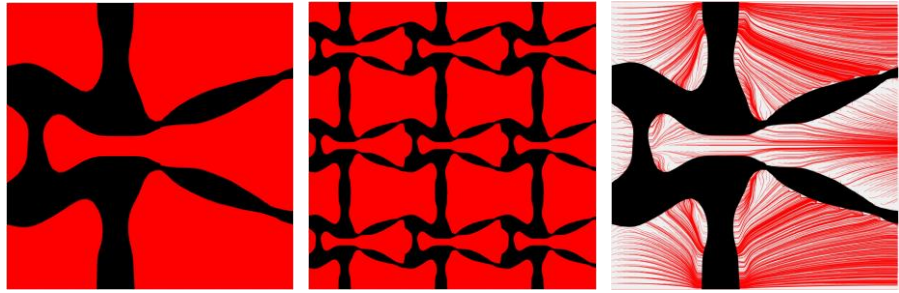
50-**20**-**30**
(D-5)
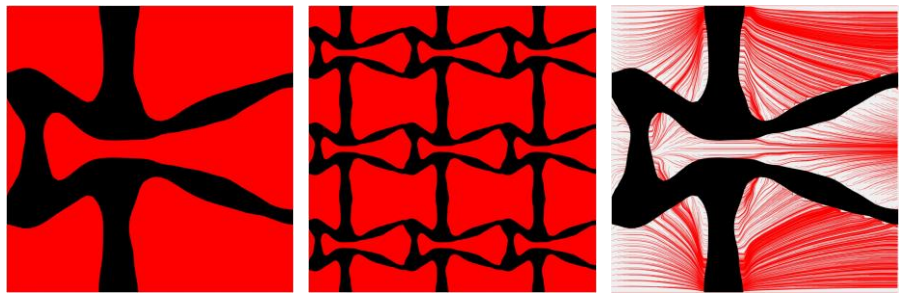
45-**25**-**30**
(D-6)
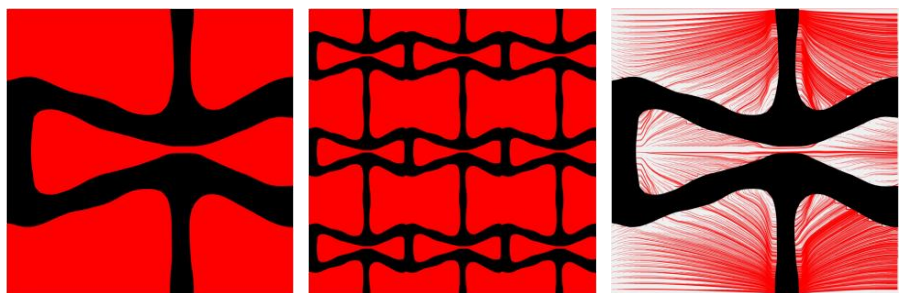
40-**30**-**30**
(D-7)
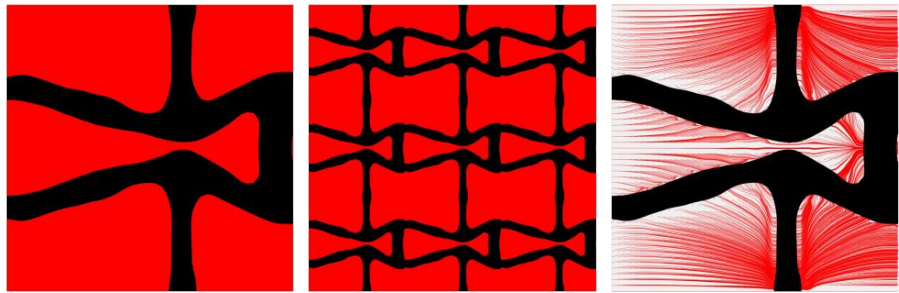
35-**35**-**30**
(D-8)
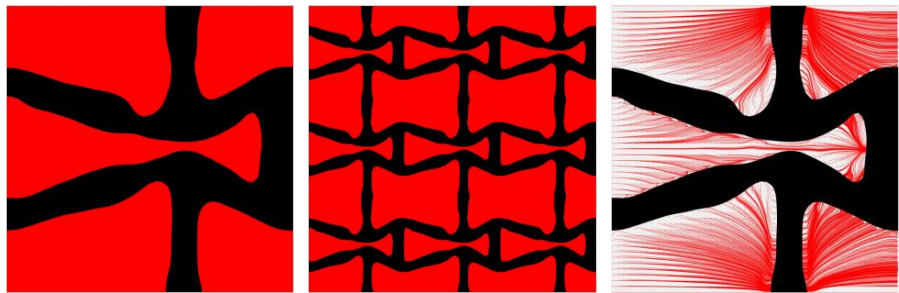
30-**40**-**30**
(D-9)
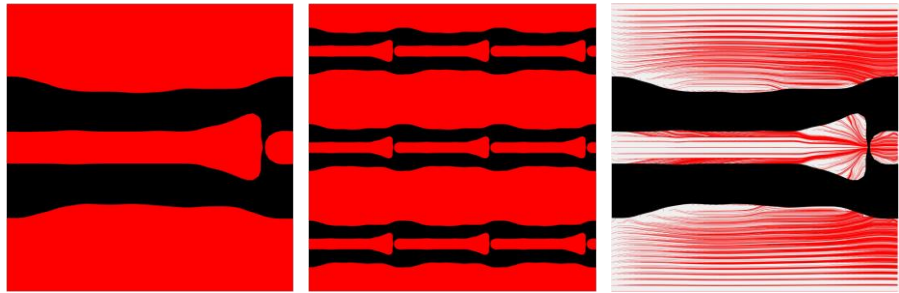
25-**45**-**30**
(D-10)

20-**50**-**30**
(D-11)

15-**65**-**30**
(D-12)

10-**60**-**30**
(D-13)

5-**65**-**30**
(D-14)

0-**70**-**30**
(D-15)
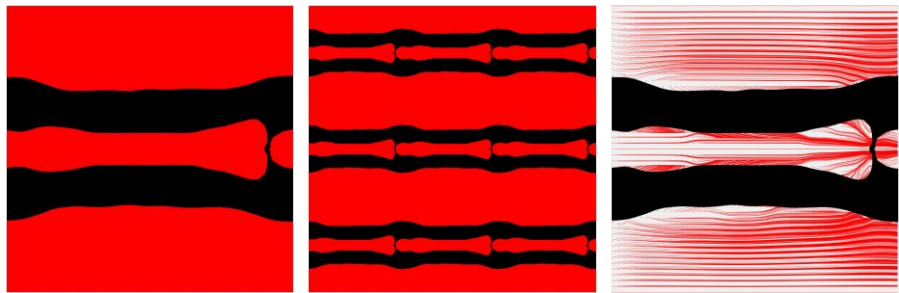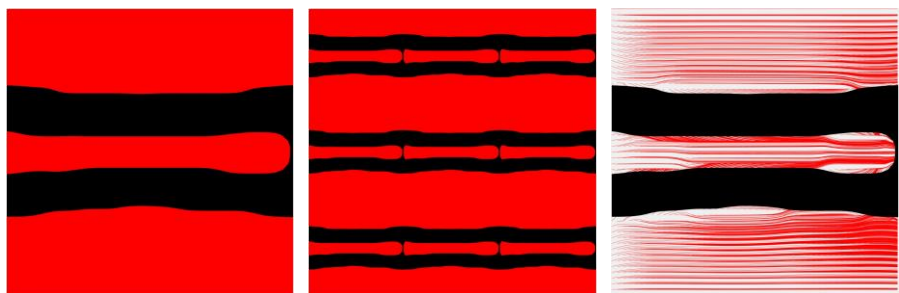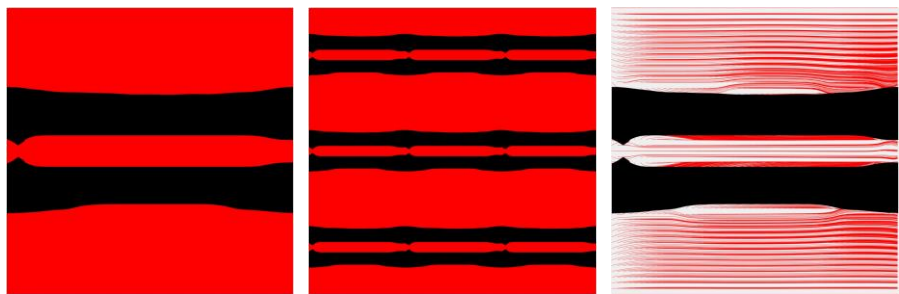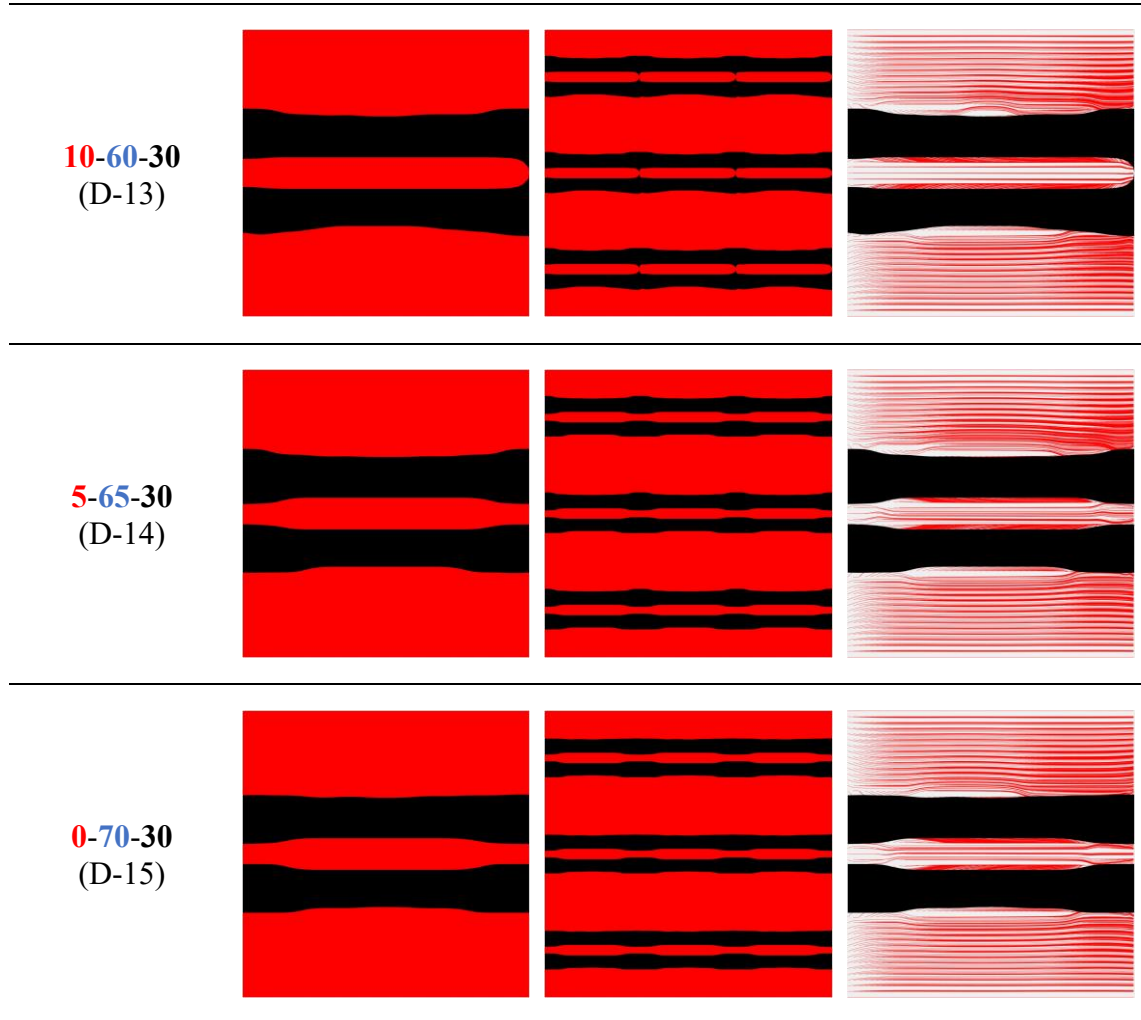
In series D, the weight factor W_3 is specified as 30%, and W_1 and W_2 are varied in a range from 0% to 70%. In Table 5-4, we can see that NPR features will be gradually die off as the decrease of W_1, and the auxetic properties will disappear when W_1 is less than 35%. In contrast, when W_1 is greater than 45%, thin struts will appear around the re-entrant features. Simultaneously, the distorted impact of the microstructure on the flow pattern will decrease as the increase of W_2, which can be found from the changes of the streamlines in the design domain. It is easy to find that more flow patterns in the design domain orientate to the flow direction as the increase of W_2, such as the changes between the results D-1 and D-15.

Moreover, in the aspect of the optimization of macro stiffness, 30% weight factor can lead to more uniform material distributions for the microstructures compared with the results in the first series, which can help to against horizontal deformations but retains the structural changes introduced by other optimization objectives to some extent. By comparison, the results D-6, D-7, and D-8 are found that have obvious re-entrant features and uniform material distributions. Besides that, all three microstructures have an opening inlet or outlet. All of them can lead to larger spaces for the fluid and facilitate to restore disturbed flow. Therefore, the relevant three combinations of the weight factors are adopted and recorded as 45%-25%-30%, 40%-30%-30%, and 35%-35%-30%, where the three values in each combination are W_1, W_2, W_3, respectively.

5.5.2 Studies of varying volume fractions
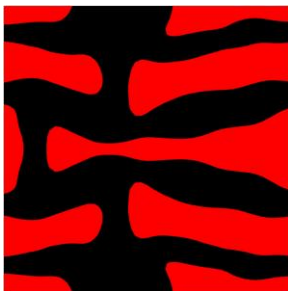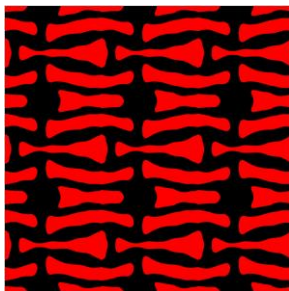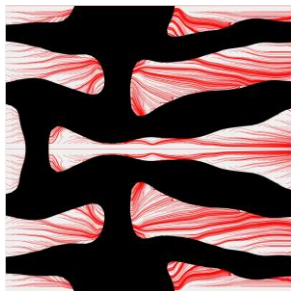
In the above four series studies, three combinations of the three weight factors for the optimization objectives are obtained: 45%-25%-30%, 40%-30%-30%, and 35%-35%-30%. As discussed, the adoption of volume fractions can also influence the optimization results. Hence, three new series studies are established to investigate the impacts of various volume fractions on the optimization results, based on the three weight factor combinations. The volume fraction of the microstructure should not be too big to block blood flow or too small that cannot support the artery, but a narrow range of adoption cannot summarize the impacts of varying volume fractions. Thus, the volume fraction values are specified from 25% to 60% in each series study.

1) **The results of series E**

The results of varying volume fractions in the range from 25% to 60% for the weight factor combination 45%-25%-30% are defined as series E and summarized in Table 5-5,

where the microstructure of each case, the related 3×3 arrays structure, and the fluid streamlines in the design domain are presented. In the table, we can see that all results present the structural characteristics of NPR and large fluid spaces along the blood flow direction. The impacts of different volume fractions mainly concentrate on the formations of different structural features to obtain the optimization objectives. When the volume fraction is greater than 50%, the structures still contain many vertical struts to obstruct the blood flow, even though some long fluid spaces are formed, such as in the middle of the case E-1 and the top and bottom regions of the case E-2. As the decrease of the volume fractions, the optimized structures show similar topologies. All the structures proximately contain two horizontal struts and three vertical struts. The differences mainly focus on the locations of the three struts, which are driven by the design of MFP and determined by the obstructions to the blood flow. In cases E-3 to E-5, some relatively thin struts exist around the re-entrant features. They can maintain large magnitudes NPR but also cause non-uniform material distributions, leading to non-uniform stress distributions. Thus, by considering the uniform distributions of the solid material and proper volume fractions, E-6, E-7, and E-8 are adopted to be further discussed.

Table 5-5 The results of various volume fractions for 45%-25%-30%

Volume(V%) (Series E)	Microstructure	Microstructure (3×3)	Streamline
60 (E-1)			
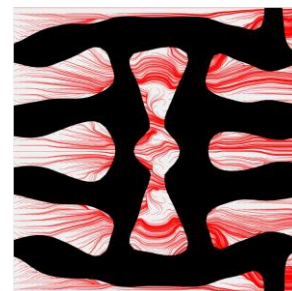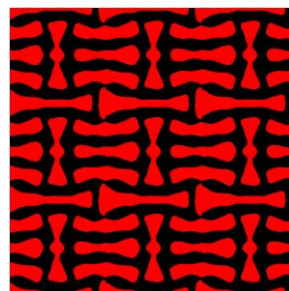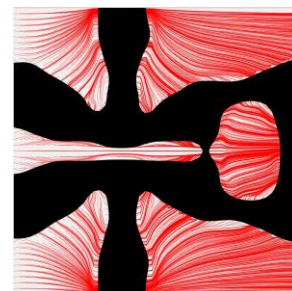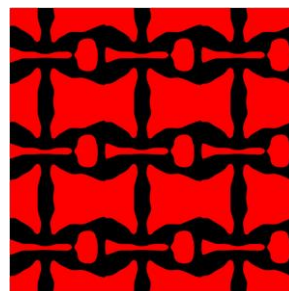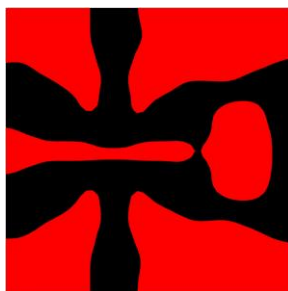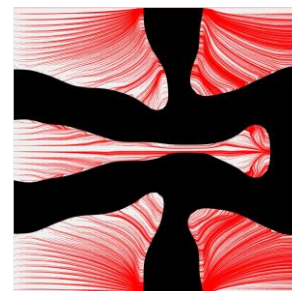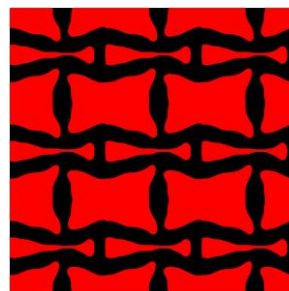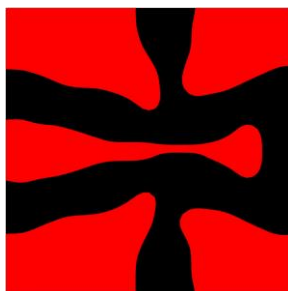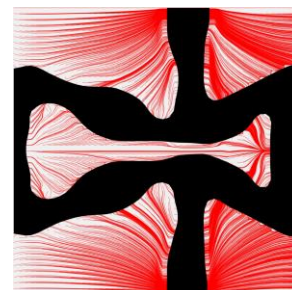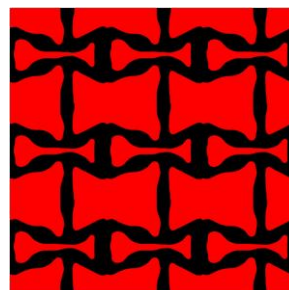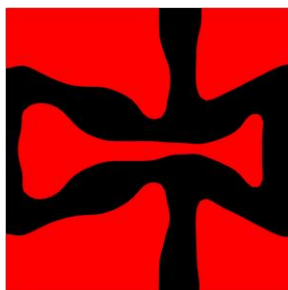
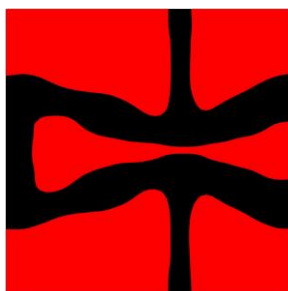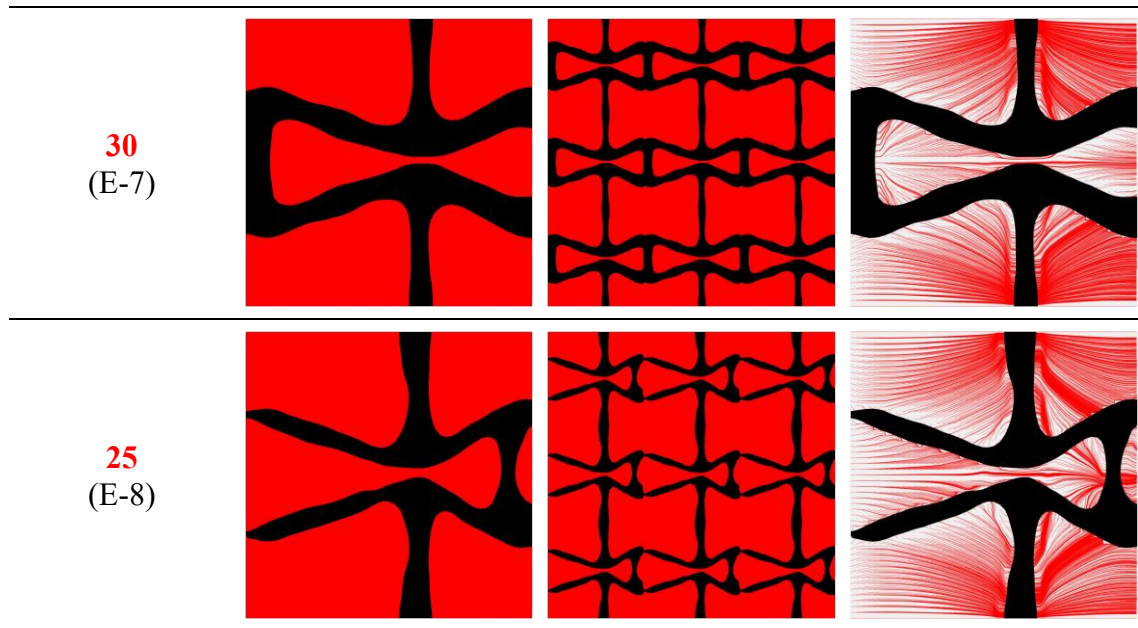| **55**
(E-2) | | | |
50 (E-3)			
45 (E-4)			
40 (E-5)			
35 (E-6)			
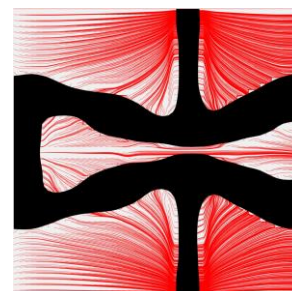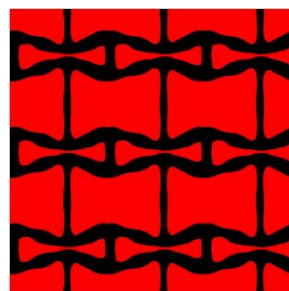
The scaled homogenized effective elasticity tensor and the MFP of cases E-6, E-7, and E-8 are summarized in Table 5-6. The relevant values of the NPRs in the two main directions(horizontal and vertical directions) and the vertical permeability are calculated in Table 5-7. From the tables, we can see both results have smaller NPR magnitudes in the flow direction and larger NPR magnitudes in the vertical direction. It means the horizontal stiffness of each structure is higher than the vertical stiffness, which can consequently enhance the ability of stents to adapt to large deformations of arteries, improving their flexibility. Meanwhile, in another direction, the NPR properties can result in a smaller compressed volume to facilitate deliverability.

On the other hand, the purpose of facilitating blood flow through the stented segment of arteries can be obtained by reducing the obstructions in the vertical direction to decrease the vertical flow, which actually requires directional differences for the optimized stent in the two main directions. Hence, those directional differences have a positive effect on the optimization result. In the fluid aspect, the differences can be detected as different

values of the effective MFPs in the two main directions, as seen in the tables. It can also find that the vertical MFP is reduced as the decrease of the volume fraction. That is because less material in the design domain can lead to larger fluid spaces, reducing the obstacles in the design domain. However, MFP in the flow direction also exhibits the same decrease trend as the vertical. The reason is that the MFPs are proportional to the flow velocities since the obstructions can accelerate the flow. Consequently, when reducing the volume fraction of the optimization, the MFPs in two main directions will decrease.

Table 5-6 The effective elasticity tensor and modified permeability of E-6, 7,8

Case	Effective Elasticity Tensor	Effective Modified Permeability
E-6	$\begin{bmatrix} 0.1281 & -0.0378 & 0 \\ -0.0378 & 0.0375 & 0 \\ 0 & 0 & 0.0024 \end{bmatrix}$	$\begin{bmatrix} 1.1998\times10^{-3} & 0 \\ 0 & 3.8157\times10^{-4} \end{bmatrix}$
E-7	$\begin{bmatrix} 0.0950 & -0.0307 & 0 \\ -0.0307 & 0.0298 & 0 \\ 0 & 0 & 0.0016 \end{bmatrix}$	$\begin{bmatrix} 1.07794\times10^{-3} & 0 \\ 0 & 2.7799\times10^{-4} \end{bmatrix}$
E-8	$\begin{bmatrix} 0.0563 & -0.0220 & 0 \\ -0.0220 & 0.0235 & 0 \\ 0 & 0 & 0.0017 \end{bmatrix}$	$\begin{bmatrix} 9.8282\times10^{-4} & 0 \\ 0 & 2.6847\times10^{-4} \end{bmatrix}$

Table 5-7 The NPRs and vertical Permeability of E-6, 7, 8

Case	NPRs	Vertical Permeability
E-6	$Mu1 = -0.2951$ $Mu2 = -1.0080$	$\mathbf{K}_{2D}^{H(2,2)} = 3.8157\times10^{-4}$
E-7	$Mu1 = -0.3232$ $Mu2 = -1.0302$	$\mathbf{K}_{2D}^{H(2,2)} = 2.7799\times10^{-4}$

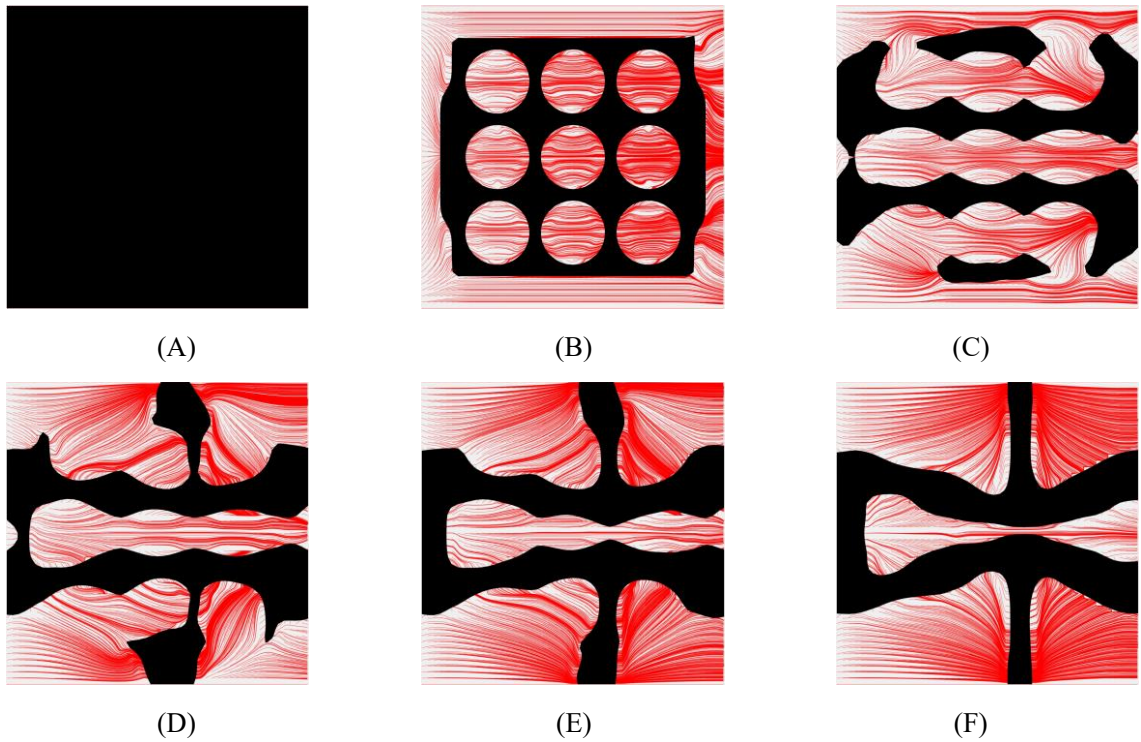| E-8	$Mu1 = -0.3907$ $Mu2 = -0.9362$	$\mathbf{K}_{2D}^{H(2,2)} = 2.6847 \times 10^{-4}$

(A)

(B)

(C)

(D)

(E)

(F)

Figure 5-5 The optimization of E-6: (A) Initial design; (B-E) Four intermediate results; (F) Final design.

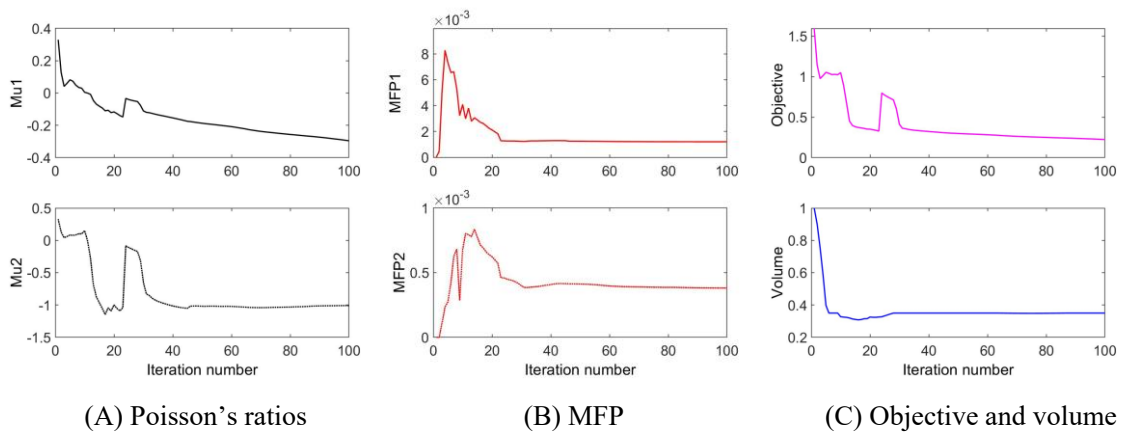(A) Poisson's ratios

(B) MFP

(C) Objective and volume

Figure 5-6 The convergent histories of E-6.

The dynamic changes of the microstructure of case E-6 are presented in Figure 5-5, where

four intermediate results are shown in Figure 5-5 (B)-(E), and the Figure 5-5 (A) and (F) show the initial design and final optimization results, respectively. In each result, the structure is presented in black colour surrounded by red flow streamlines. Besides that, the convergence curves of the two Poisson's ratios Mu1 and Mu2 can be seen in Figure 5-6 (A). The MFPs in two main directions are defined as MFP1 and MFP2. Their convergent histories can be seen in Figure 5-6 (B). Figure 5-6 (c) shows the convergence curves of the overall objective and structural volume fraction. From these figures, it is easy to find that most streamlines in the design domain gradually orient to the flow direction during the optimization, which can also be detected from the decrease of the vertical MFP.

Since the design domain is filled with solid material in the initial state, it blocks the blood flow. The values of MFP in both directions are zero. Thus, as the optimization starts, the blood flow occurs in the design domain as the structural material decreases, leading to a dramatic increase of the MFP in both directions. After the volume fraction of the structure obtains the prescribed value, both MFPs begin to decrease as the optimization. The MFP2 becomes much smaller than MFP1, indicating the efficiency of the optimization for MFP. However, vertical flows cannot be avoided in the design domain due to the optimization for auxetics. It introduces re-entrant features into the optimized structure. The re-entrant structural characteristics make the horizontal struts at an angle to the blood flow, leading to vertical flows. As for the weighted objective and volume fraction changes, they are stably converged to the final results, except fluctuations in a short period, as shown in Figure 5-6.
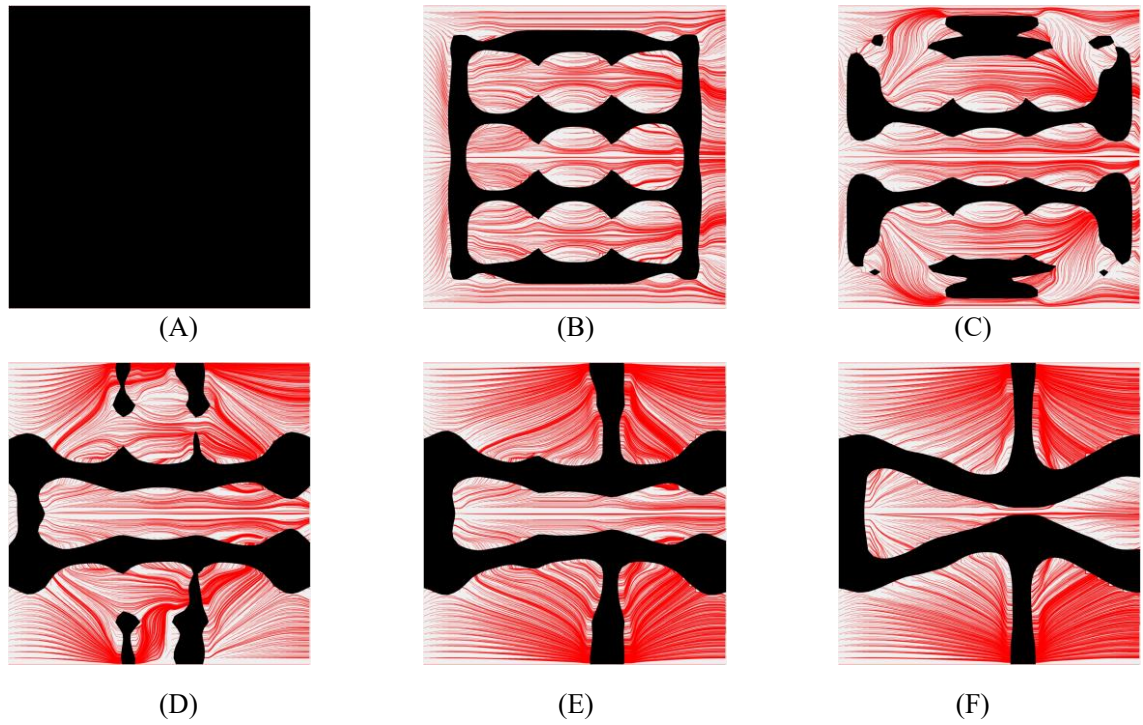
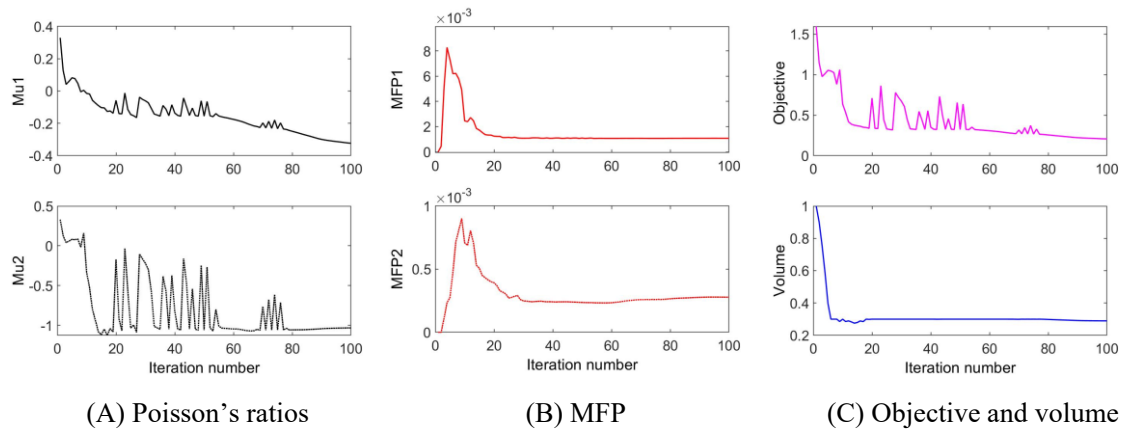Figure 5-7 The optimization of E-7: (A) Initial design; (B-E) Four intermediate results; (F) Final design.

(A) Poisson's ratios　　　(B) MFP　　　(C) Objective and volume

Figure 5-8 The convergent history of E-7.

The dynamic changes of the microstructure in case E-7 are presented in Figure 5-7. The final optimized microstructure is very similar to E-6 but has more uniform material distribution due to less material volume fraction. The convergent histories of relevant metrics are shown in Figure 5-8. Although some fluctuations occur in the NPR

convergence, especially for *Mu2*, the fluctuations are gradually die out as the optimization, and the NPR is converged to the final result.

(A) (B) (C)

(D) (E) (F)
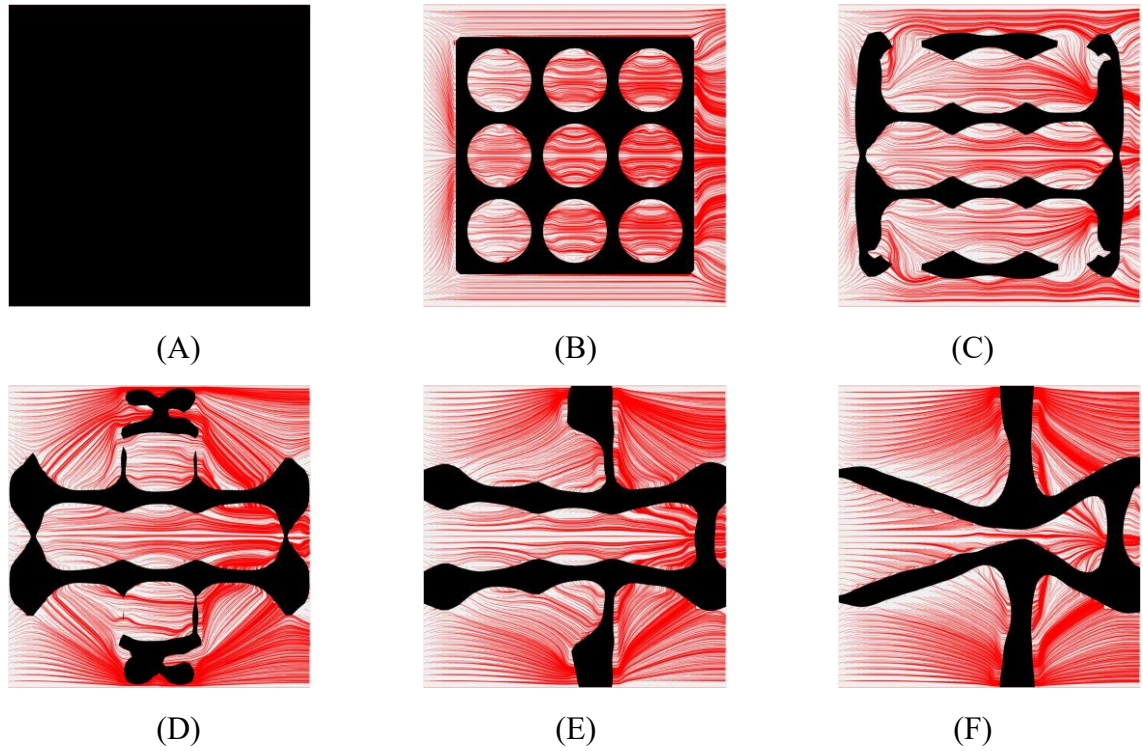
Figure 5-9 The optimization of E-8: (A) Initial design; (B-E) Four intermediate results; (F) Final design.

(A) Poisson's ratios (B) MFP (C) Objective and volume
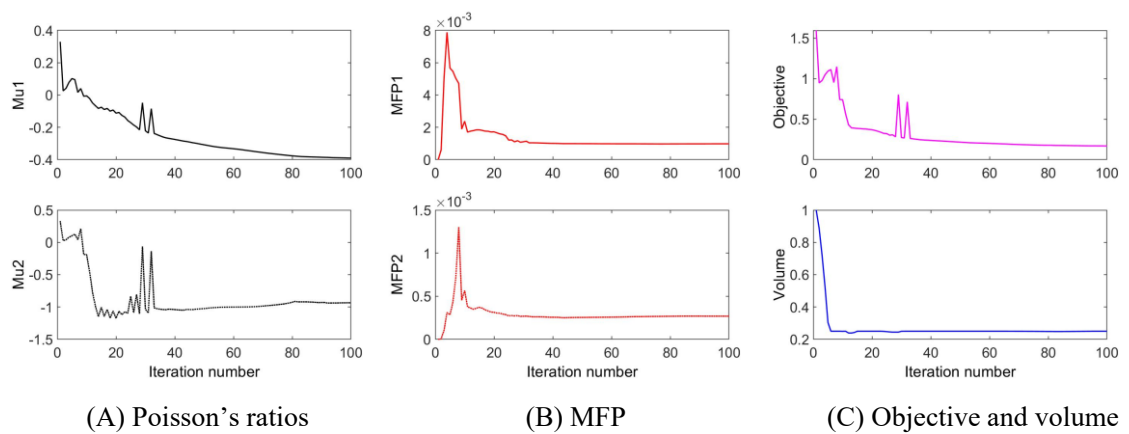
Figure 5-10 The convergent history of E-8.

The dynamic changes of the microstructure in case E-8 are presented in Figure 5-9. The

optimized microstructure also forms a long fluid space in the middle region, but it presents an opening at the inlet side, forming a vertical strut close to the outlet. Since the opening in the design domain still orients to the flow direction, it can also reduce the obstructions to the blood flow. In Figure 5-10, the convergent histories of relevant metrics are also presented. They all show a stable optimization process in that case. Overall, in all three results, we can easily find that long fluid spaces between struts in the middle regions can help recover flow patterns and facilitate blood flow.
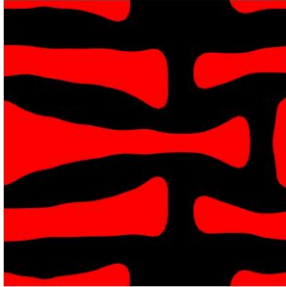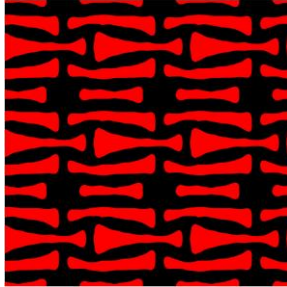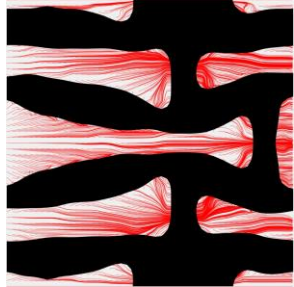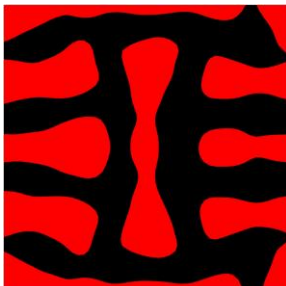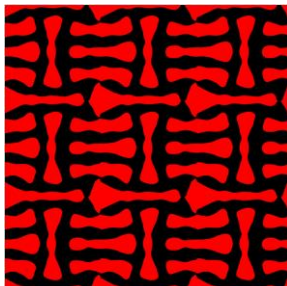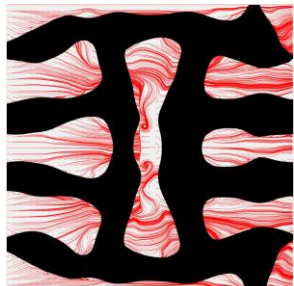
2) The results of series F

The studies of varying volume fractions in a range of 25 - 60% for the weight factor combination 40%-30%-30% are defined as series F. The results are summarized in Table 5-8, where the microstructures, the related 3×3 arrays structures, and the fluid streamlines in the design domain are presented. It shows that all results have obvious re-entrant features, indicating NPR properties. Besides that, all the optimized microstructures exhibit structural differences along the direction of blood flow, which mainly concerns the distributions of vertical struts. For example, in the results F-1, the vertical struts are closer to the outlet, leading to a relatively long fluid space behind the inlet to facilitate blood flow. As the decrease of volume fractions, the members and widths of vertical struts are gradually reduced, such as F-2, 3, and 4. When the volume fraction is equal or less than 35%, only two horizontal struts exist in the design domain and are connected by a single vertical strut, resulting in one opening in the inlet or outlet side. The other two vertical struts are formed beside the two horizontal struts to connect different microstructures, as shown in their 3×3 arrays structures. As for these results, the design domain can be divided into three subregions by the two horizontal struts. Although the locations of the three vertical struts are different, only one vertical strut exists in each

subregion. Thus, in the F-6, 7, and 8, the three vertical struts with different locations induce similar obstructions to the blood flow. However, since the obstructions of struts can also accelerate blood flow, the vertical struts closer to the inlet side lead to more blood flow be accelerated behind the struts in the design domain. The accelerations of the struts to the blood flow may affect the WSS.

Compared with series E, series F adopts a smaller weight factor of auxetic optimization. Thus, the results exhibit less thin struts around the re-entrant features, resulting in more uniform material distributions in the design domain. Among that, the results F-6, F-7, and F-8 have fewer obstructions to the blood flow and more uniform material distributions. They can be further discussed.
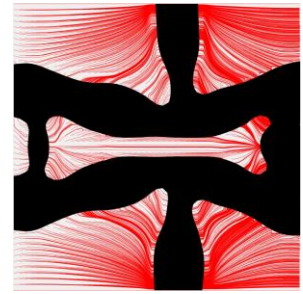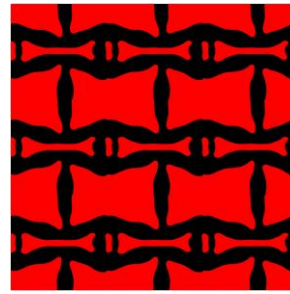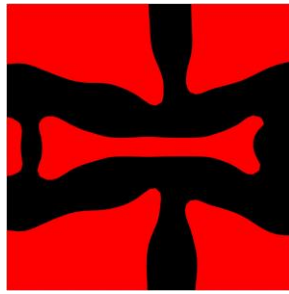
Table 5-8 The results of various volume fractions for 40%-30%-30%

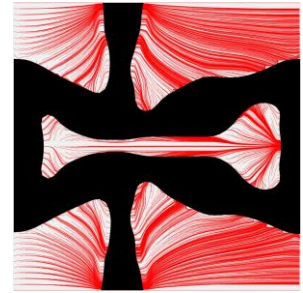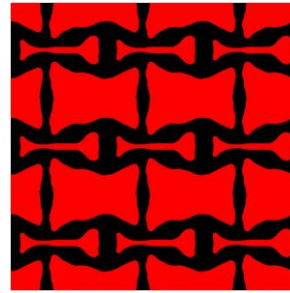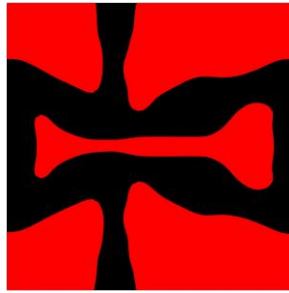| Volume(V%) (Series F)	Microstructure	Microstructure (3×3)	Streamline
60 (F-1)			
55 (F-2)			
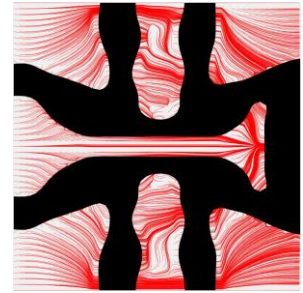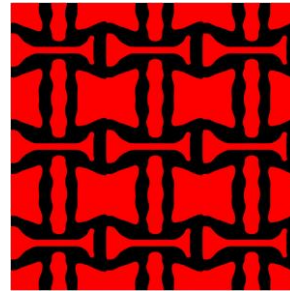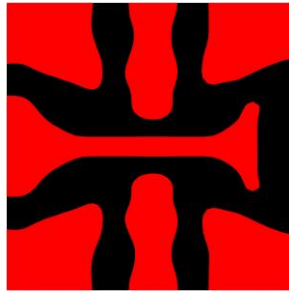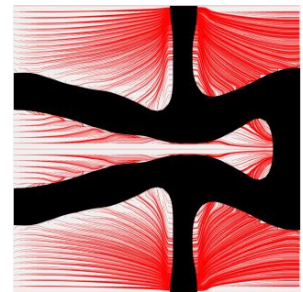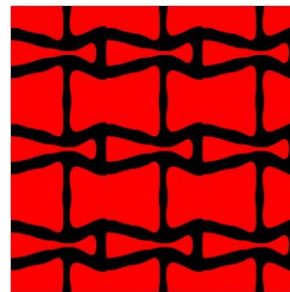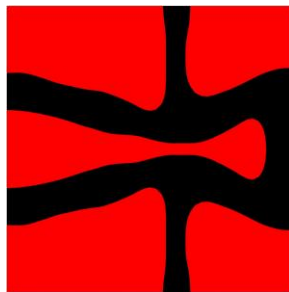
50 (F-3)			
45 (F-4)			
40 (F-5)			
35 (F-6)			
30 (F-7)			
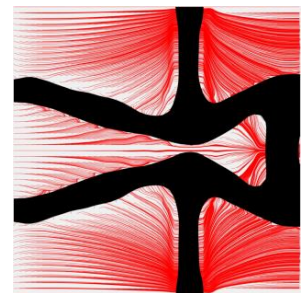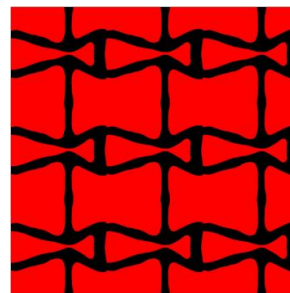
25
(F-8)
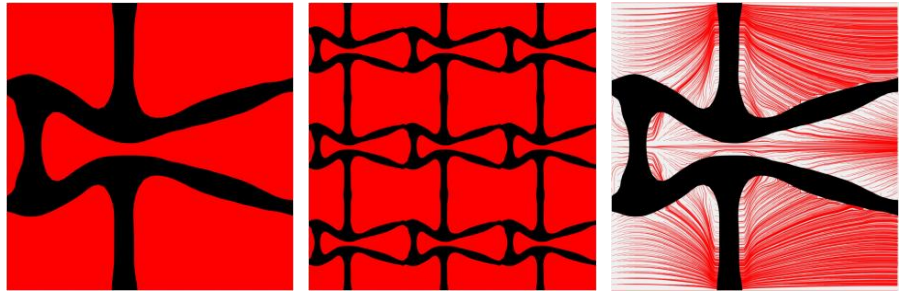
Table 5-9 The effective elasticity tensor and modified permeability of F-6, 7, 8

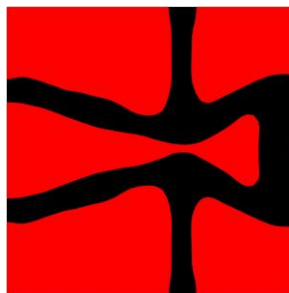| Case	Effective Elasticity Tensor	Effective Modified Permeability
F-6	$\begin{bmatrix} 0.1778 & -0.0349 & 0 \\ -0.0349 & 0.0314 & 0 \\ 0 & 0 & 0.0019 \end{bmatrix}$	$\begin{bmatrix} 1.1683\times10^{-3} & 0 \\ 0 & 3.3433\times10^{-4} \end{bmatrix}$
F-7	$\begin{bmatrix} 0.1647 & -0.0281 & 0 \\ -0.0281 & 0.0277 & 0 \\ 0 & 0 & 0.0020 \end{bmatrix}$	$\begin{bmatrix} 1.1358\times10^{-3} & 0 \\ 0 & 2.2706\times10^{-4} \end{bmatrix}$
F-8	$\begin{bmatrix} 0.0712 & -0.0259 & 0 \\ -0.0259 & 0.0259 & 0 \\ 0 & 0 & 0.0021 \end{bmatrix}$	$\begin{bmatrix} 9.2690\times10^{-4} & 0 \\ 0 & 1.8221\times10^{-4} \end{bmatrix}$

Table 5-10 The NPRs and vertical Permeability of F-6, 7, 8

Case	NPRs	Vertical Permeability
F-6	$Mu1 = -0.1963$ $Mu2 = -1.1115$	$\mathbf{K}_{2D}^{H(2,2)} = 3.3433\times10^{-4}$
F-7	$Mu1 = -0.1706$ $Mu2 = -1.0144$	$\mathbf{K}_{2D}^{H(2,2)} = 2.2706\times10^{-4}$
F-8	$Mu1 = -0.3638$ $Mu2 = -1.0000$	$\mathbf{K}_{2D}^{H(2,2)} = 1.8221\times10^{-4}$

The scaled homogenized effective elasticity tensors and the MFPs of the cases F-6, F-7, and F-8 are summarized in Table 5-9. The relevant values of the NPRs in the two main directions and the vertical MFP are presented in Table 5-10. All the results exhibit NPRs. The results in the tables also show directional differences in the effective properties in the two main directions. The similar directional differences are also detected in series E. As we discussed, the differences can benefit stenting mechanical performances and reduce obstructions of the structures to the blood flow. Although the locations of the openings in the results are different, they all orient to the flow direction. Both of them can reduce the stenting obstructions and facilitate blood flow, which can be found that all their vertical MFP are much smaller than the horizontal MFP. Besides that, the MFPs in all directions are reduced as the decrease of volume fraction. It indicates that the accelerations of the stenting structures to the blood flow are reduced as the decrease of the fluid obstructions. As we know, the accelerations from the stenting structures can lead to extremely high WSS to significantly increase the risk of ST. Hence, the decrease in fluid obstructions can prevent too high WSS. In order to further investigate their optimization process, the structural changes and relevant convergences of the objectives are discussed following.
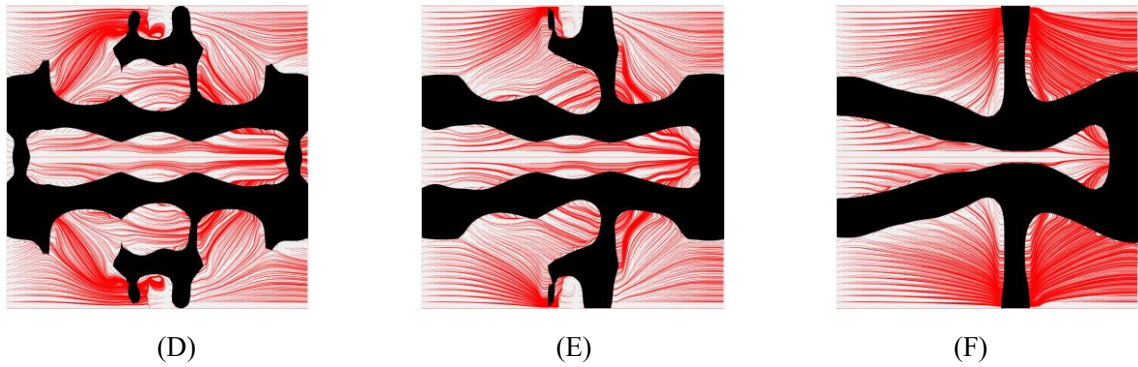

(A)   (B)   (C)

(D)   (E)   (F)
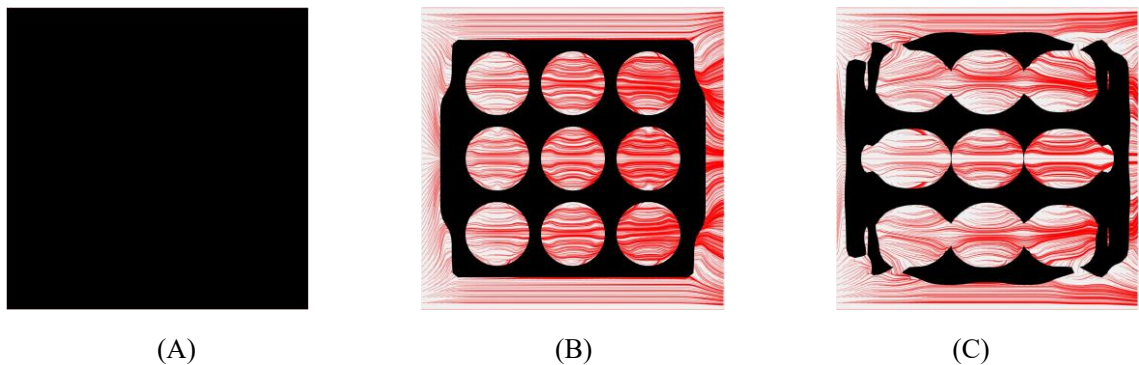
Figure 5-11 The optimization of F-6: (A) Initial design; (B-E) Four intermediate

results; (F) Final design.

(A) Poisson's ratios   (B) MFP   (C) Objective and volume
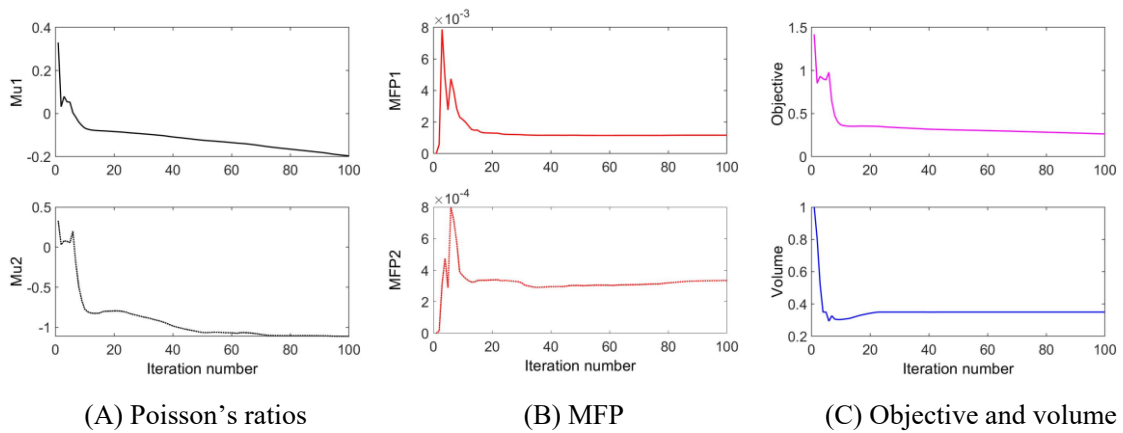
Figure 5-12 The convergent history of F-6.

The dynamic changes of the microstructure of case F-6 are presented in Figure 5-11, where the initial design, intermediate results, and final optimization results presented. From the topological changes of case F-6, we can see that the material is more prone to concentrate on the two vertical struts during the optimization, and most streamlines around the microstructure gradually orient to the blood flow as the optimization. Besides that, three vertical struts are formed. One of them is utilized to connect the horizontal struts, creating an opening at the inlet side. The other two vertical struts are generated to connect other microstructures in the same circumference. We can also find that, in the optimization, two re-entrant features are gradually formed at the junctions of the vertical

and horizontal struts. Thus, the two vertical struts are at an angle to the flow direction.

The convergent curves of the design objectives and effective properties are presented in Figure 5-12. All objectives are gradually converged to the results. From the convergences, we can find that the changes mainly exist in the first 20 iterations. It is because that the volume fraction is quickly reduced to the prescribed value in the early iterations, which can induce significant structural changes in that period. After that, the structural topology is nearly determined, and then the changes mainly focus on the local features and the shapes, such as the re-entrant angles and the outlines of the struts, which are all critical to the optimization result, especially for the MFPs.

| (A) | (B) | (C) |
| (D) | (E) | (F) |

Figure 5-13 The optimization of F-7: (A) Initial design; (B-E) Four intermediate results; (F) Final design.
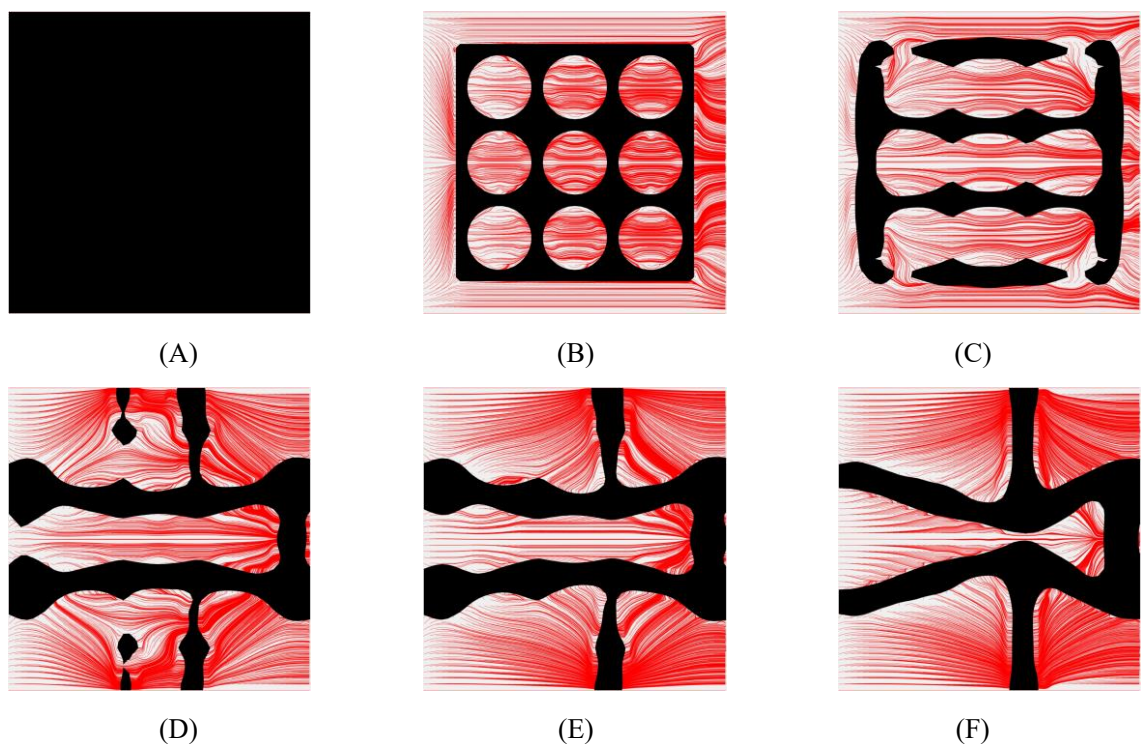
(A) Poisson's ratios   (B) MFP   (C) Objective and volume

Figure 5-14 The convergent history of F-7.

The dynamic changes of the microstructure in case F-7 are presented in Figure 5-13. The result is very similar to F-6 but has more uniform material distribution due to less volume fraction. Moreover, the streamline patterns around the microstructure also indicate fewer obstructions. The convergences of the related objectives in the optimization of case F-7 are shown in Figure 5-14. Among that, the MFPs and structural volume are steadily converged to the results. Some fluctuations occur in the NPRs convergence curves, especially for the Mu2, which also leads to fluctuations in the convergence of the design objective. It can be found that the fluctuations gradually die out as the optimization, and the NPRs and objectives are converged to the final results.

(A)   (B)   (C)

<center>(D)   (E)   (F)</center>
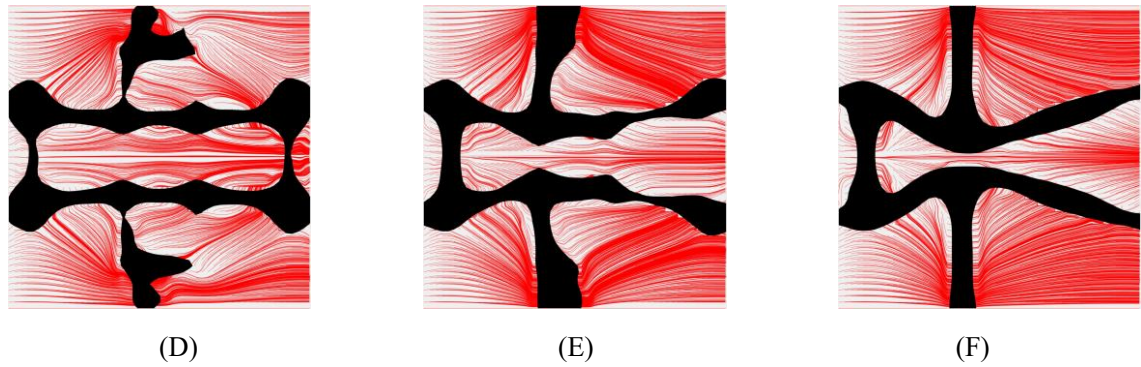
Figure 5-15 The optimization of F-8: (A) Initial design; (B-E) Four intermediate results; (F) Final design.
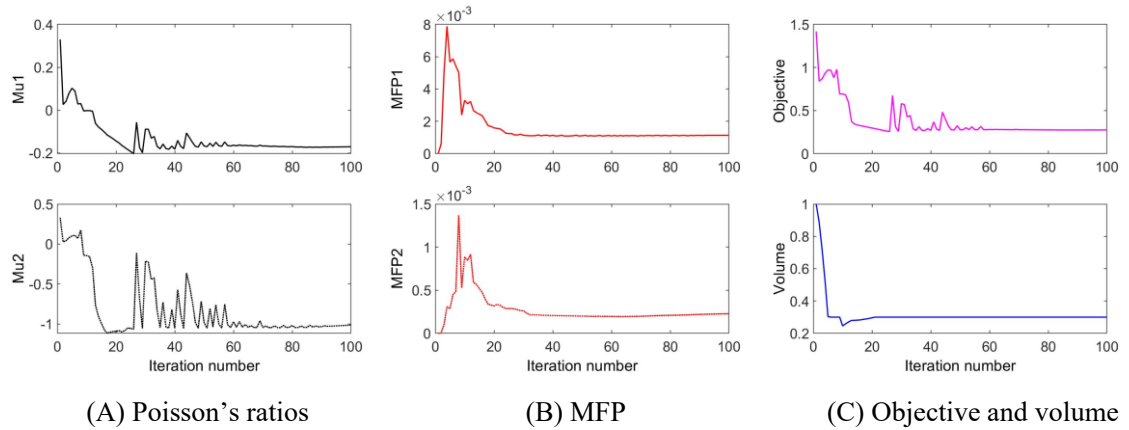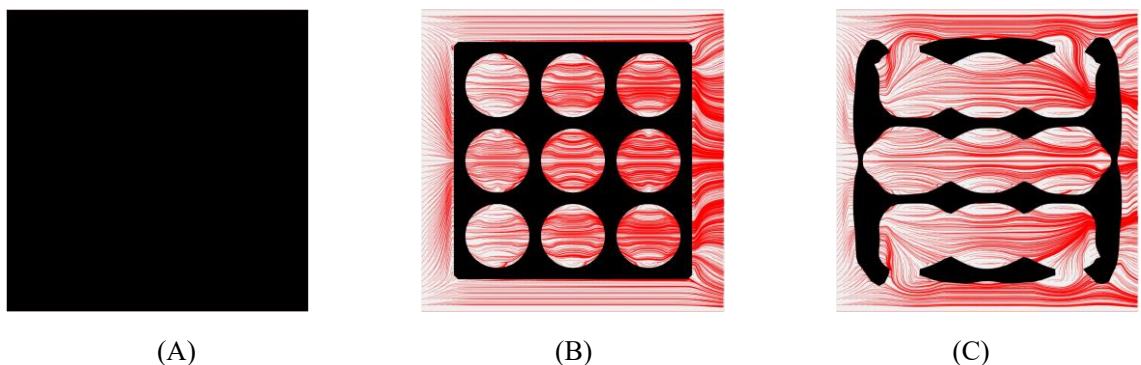

<center>(A) Poisson's ratios   (B) MFP   (C) Objective and volume</center>
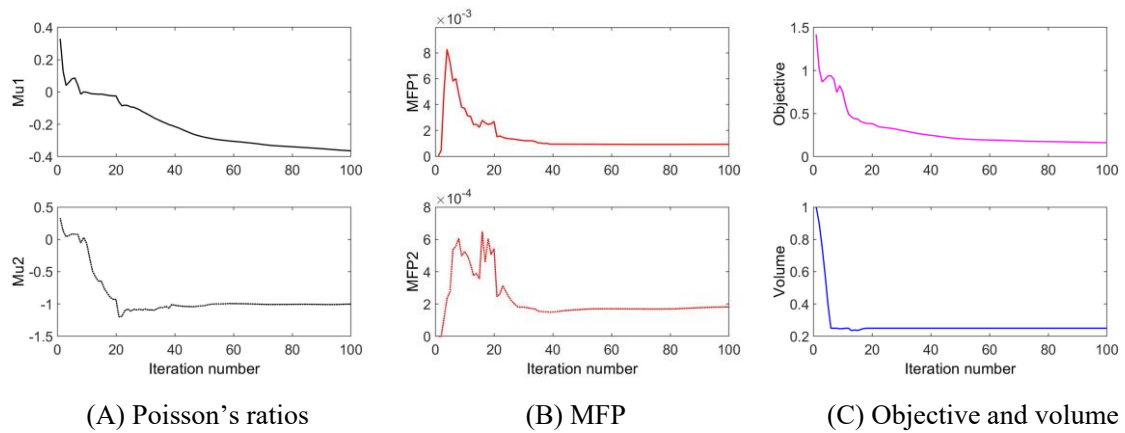
Figure 5-16 The convergent history of F-8.

The dynamic changes of the microstructure in case F-8 are presented in Figure 5-15. From the results, we can see that the streamlines around the structures gradually orient to the flow direction as the optimization, indicating the efficiency of the MFP optimization. Similar to the result F-7, the optimized structure in F-8 also contains two horizontal struts and three vertical struts. Besides that, two re-entrant features are also created in the conjunctions of the struts. The main difference between F-7 and F-8 is the opening location, where the opening in F-8 is located at the outlet side. Additionally, due to the lower volume fraction, the struts of the structures are thinner than F-7. The convergences of the related objectives and volume fraction are shown in Figure 5-16. All the objectives

and volume fractions are steadily converged to the results.
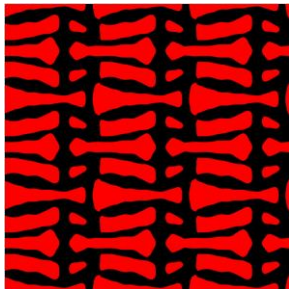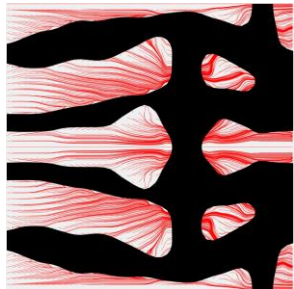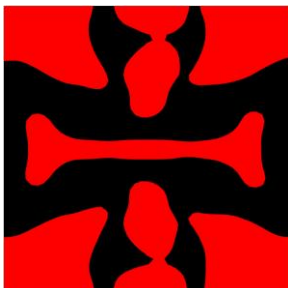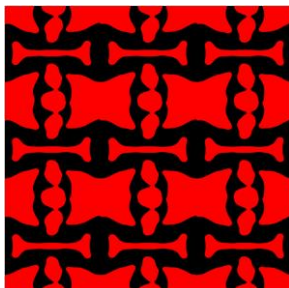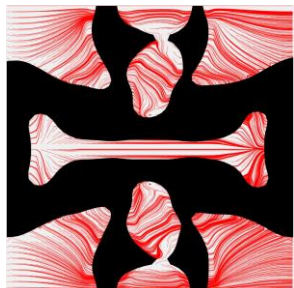
In a word, all these optimized results in series F present more uniform material distributions and fewer obstructions than series E, which can be demonstrated by the optimized structure and their MFPs. Besides that, the results in E-6 to E-8 and F-6 to F-8 exhibit similar structural characteris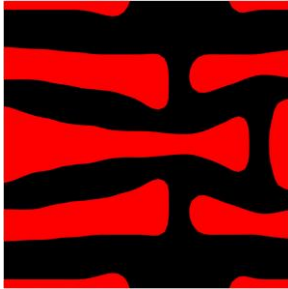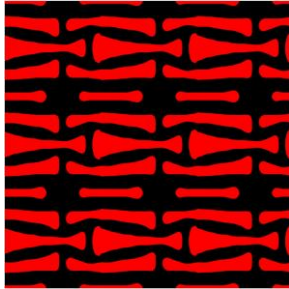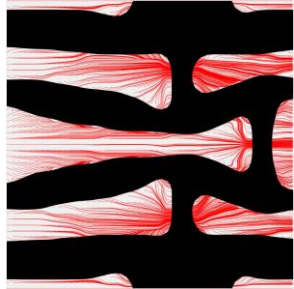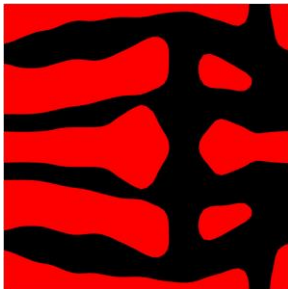tics. Their differences mainly focus on the locations of the openings along the flow direction, where some of them located at the inlet side and others at the outlet side. The results indicate that both opening locations can facilitate blood flow, resulting in fewer obstructions.

3) The results of series G

The studies of varying volume fractions in a range of 25 - 60% for the weight factor combination 35%-35%-30% are defined as series G. The results are summarized in Table 5-11, where the microstructures, the related 3×3 arrays microstructures, and the fluid streamlines in the design domain are presented. In that series, the same weight factors are defined for the objectives of auxetics and MFP. It can be found that all the optimized structures containing long fluid regions along the flow direction, facilitating blood flow. It indicates that even though the objectives of auxetics and MFP have the same weight factors, the optimization for MFP exhibits more contributions to the result. Thus, more material in the design domain is assigned to the horizontal struts, leading to relatively thinner struts around the re-entrant conjunctions to maintain auxetic properties. In G-1 and G-2, although openings are formed at the inlet side to reduce the obstacles along the flow direction, the structures with large volume fractions still block most blood flows. As the volume fractions decrease, the optimized structure with 45% material exhibits less disturbed streamlines but still contains more vertical struts that obstruct the blood flow.

When the volume fractions are equal or less than 40 %, the optimized structures present similar structural layouts, which are also similar to the results in series E and F. In G-5 to G-8, each result consists of two horizontal struts and three vertical struts, forming an opening at the inlet side. Among these results, G-6 and G-7 with relatively uniform material distributions are further investigated.

Table 5-11 The results of various volume fractions for 35%-35%-30%

Volume(V%) (Series G)	Microstructure	Microstructure (3×3)	Streamline
60 (G-1)			
55 (G-2)			
50 (G-3)			

45 (G-4)			
40 (G-5)			
35 (G-6)			
30 (G-7)			
25 (G-8)			
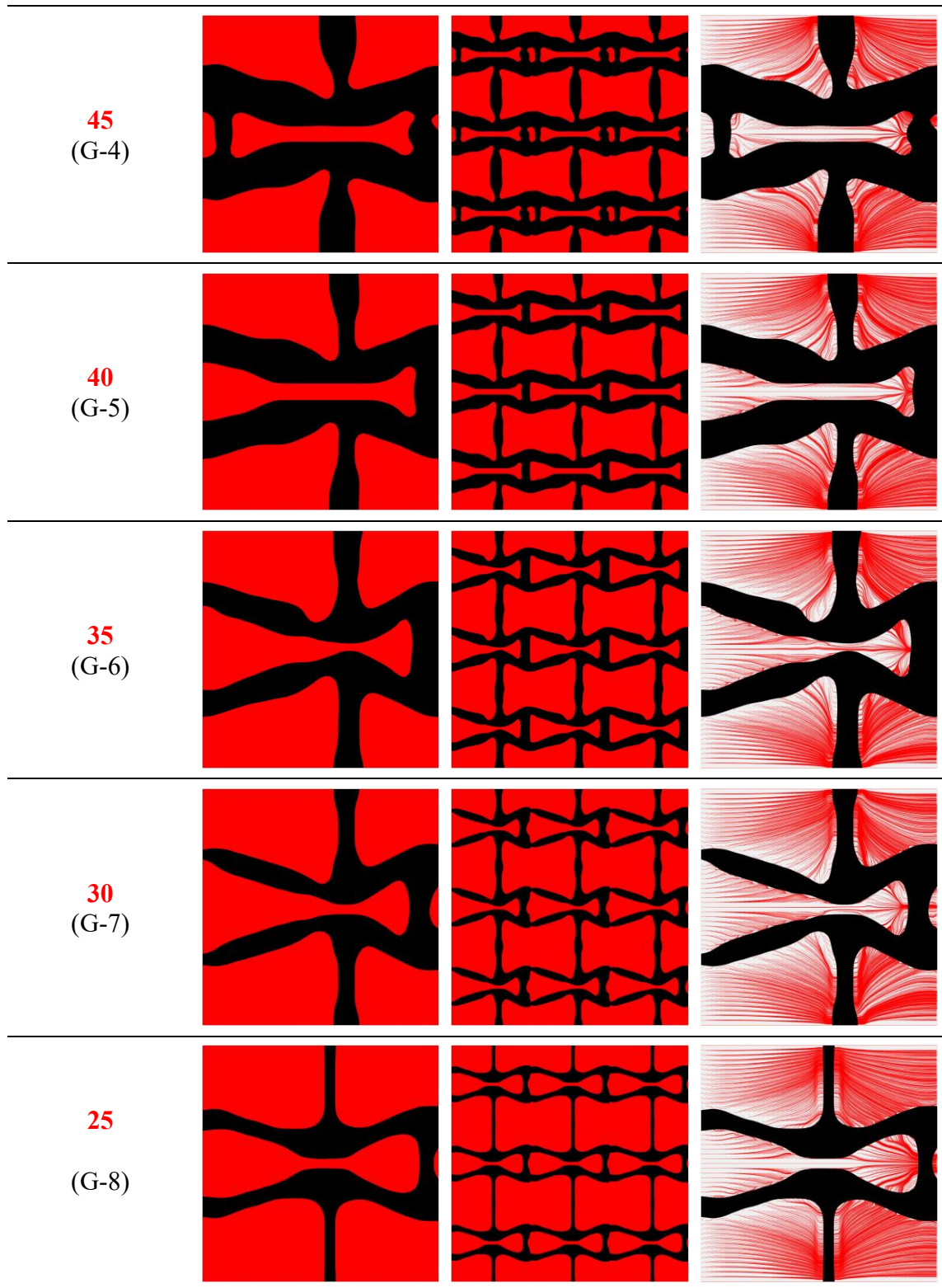
Table 5-12 The effective elasticity tensor and modified permeability of G-6, 7

Case	Effective Elasticity Tensor	Effective Modified Permeability
G-6	$\begin{bmatrix} 0.1416 & -0.0389 & 0 \\ -0.0389 & 0.0372 & 0 \\ 0 & 0 & 0.0029 \end{bmatrix}$	$\begin{bmatrix} 1.1982 \times 10^{-3} & 0 \\ 0 & 3.1531 \times 10^{-4} \end{bmatrix}$
G-7	$\begin{bmatrix} 0.1082 & -0.0339 & 0 \\ -0.0339 & 0.0324 & 0 \\ 0 & 0 & 0.0022 \end{bmatrix}$	$\begin{bmatrix} 1.0593 \times 10^{-3} & 0 \\ 0 & 2.5233 \times 10^{-4} \end{bmatrix}$

Table 5-13 The NPRs and vertical Permeability of G-6, 7

Case	NPRs	Vertical Permeability
G-6	$Mu1 = -0.2747$ $Mu2 = -1.0457$	$\mathbf{K}_{2D}^{H(2,2)} = 3.1531 \times 10^{-4}$
G-7	$Mu1 = -0.3133$ $Mu2 = -1.0463$	$\mathbf{K}_{2D}^{H(2,2)} = 2.5233 \times 10^{-4}$

The scaled homogenized effective elasticity tensor and the MFPs of cases G-6 and G-7 are listed in Table 5-12. Their NPRs and the vertical MFPs are presented in Table 5-13. Both results of G-6 and G-7 show significant NPRs and the reduced vertical MFP. Besides that, the effective properties of the results exhibit directional differences, which can also be detected from the structural differences in the two main directions. As discussed in series E and F, these differences can benefit both the mechanical and fluid properties of stents.
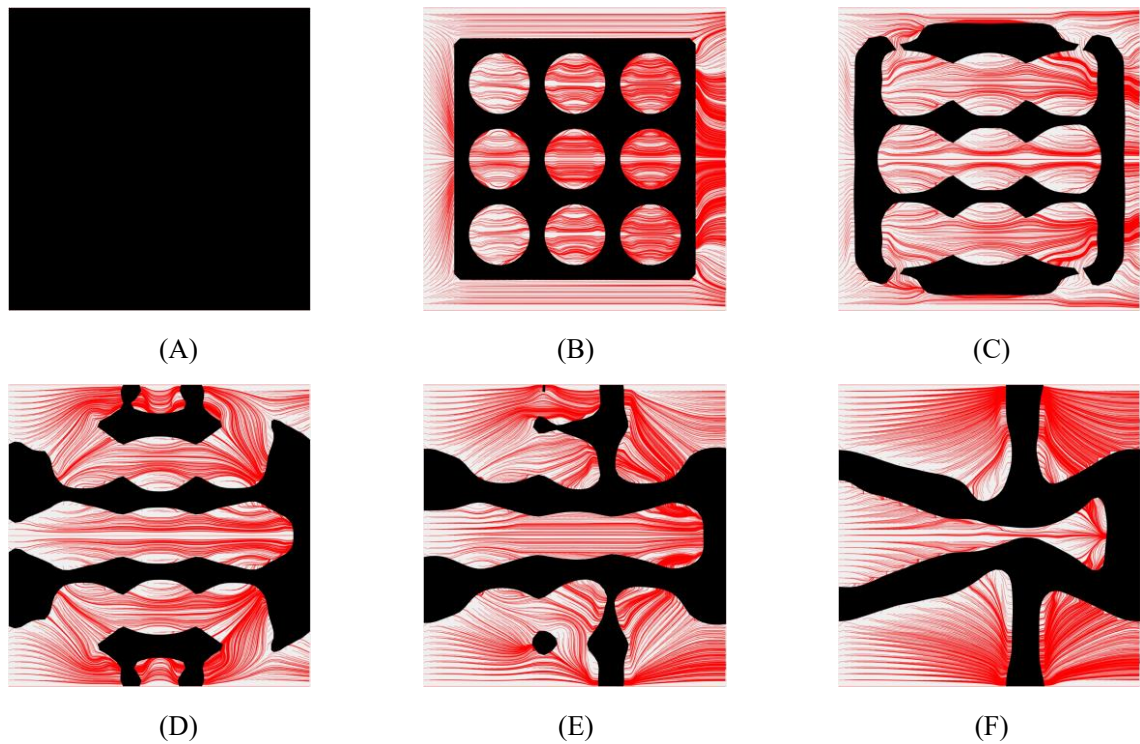
Figure 5-17 The optimization of G-6: (A) Initial design; (B-E) Four intermediate results; (F) Final design.
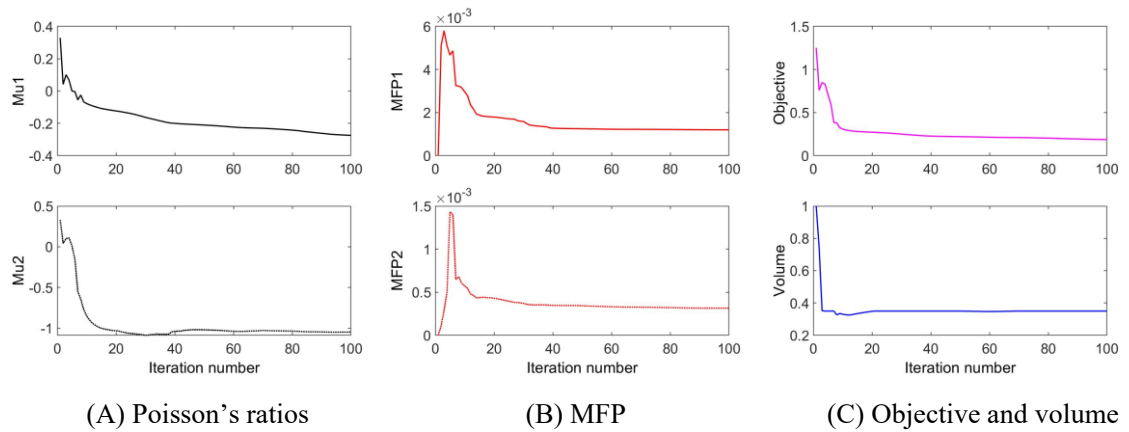
Figure 5-18 The convergent history of G-6.
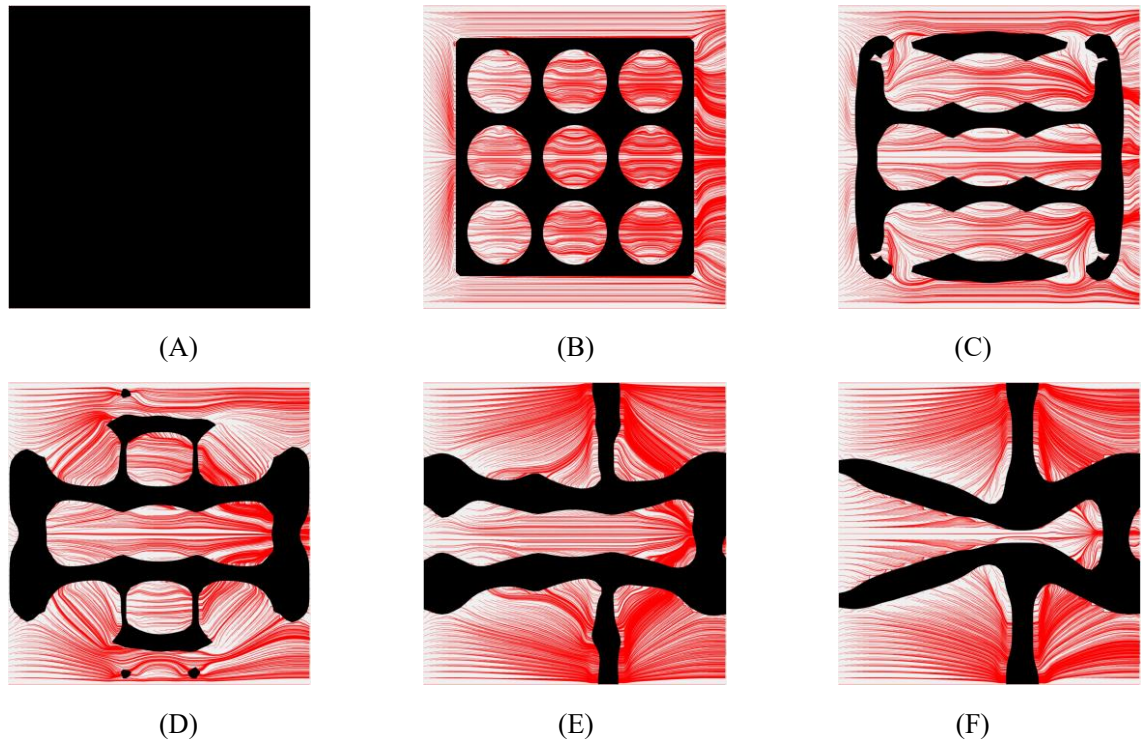
Figure 5-19 The optimization of G-7: (A) Initial design; (B-E) Four intermediate results; (F) Final design.

(A) Poisson's ratios   (B) MFP   (C) Objective and volume
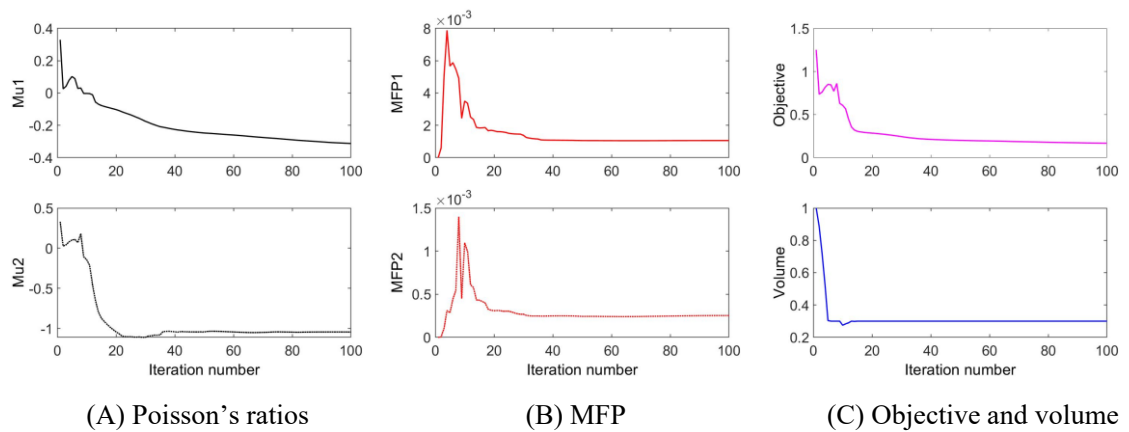
Figure 5-20 The convergent history of G-7.

The dynamic changes of the microstructure in case G-6 are presented in Figure 5-17. We can see the solid material is gradually assigned to the horizontal struts during the optimization, resulting in fewer obstructions to the blood flow. Moreover, apparent re-entrant characteristics are also formed simultaneously to introduce auxetic properties. As

shown in Figure 5-17 (F), the blood flow is mainly disturbed by the vertical struts, but the flow patterns can be recovered behind the struts due to large fluid spaces. Thus, local recirculation regions may occur around the vertical struts but should be very small. The dynamic changes of the microstructure in case G-7 present a similar optimization process and are shown in Figure 5-19. Since G-7 has a smaller volume fraction, it has more uniform material distributions than G-6. The convergences of the design objectives and volume fractions for G-6 and G-7 are presented in Figures 18 and 20, respectively. All effective properties, objectives, and volume in two cases are steadily converged to the results.

5.5.3 Discussion

From the above studies, we can find two main aspects that can determine the optimization results. One is the combination of the three weight factors of the objectives, and another one is the volume fraction. Among that, the weight factors have more impacts on the topology of the structures than volume fractions. In this optimization model, all three design objectives are demonstrated to have similar contribution levels to the results. By the investigations of series E, F, and G, all the three combinations can lead to some results with uniform material distributions and obtain a balance of the three design objectives. The investigations also indicate that two different kinds of structures can benefit optimization more. One is the structure with an opening at the inlet side, such as E-8, F-6, F-7, G-6, and G-7. Another one is the structure with an opening at the outlet side, such as E-6, E-7, and F-8. All these results have similar structural layouts with directional differences. As we discussed, both two kinds can significantly reduce the obstructions to flows and facilitate blood flow. Hence, the results of F-7, F-8, and G-7 are adopted for

the new stents by considering the uniform material distributions and different structural types. Among that, the result of F-8 with an opening outlet. The results of F-7 and G-7 have opening inlets, but their vertical struts beside the outlet are different. In the following, the three optimized stenting structures will also be numerically validated by using commercial software ANSYS.

Chapter 6 Numerical validation for the hemodynamic optimized auxetic stents

The proposed optimization model for stents aims to minimize the stent induced adverse hemodynamic changes via reducing the obstructions of the stenting structures to the blood flow. It can be achieved by minimizing the vertical flow, which can be measured by the vertical MFP. However, as the widely accepted metrics for stented hemodynamic behaviors, WSS and related derivatives are usually used. Hence, in order to further validate the properties of the optimization results, the optimized microstructures in cases F-7, F-8, and G-7 are then simulated by using software ANSYS 2019R3. The results F-7 and F-8 are the designs with 30% and 25% volume fractions, respectively. They share a same set of weight factors: 40%, 30%, and 30%. The results G-7 is the design with 30% volume fraction, and the weight factor of this design is 35%, 35%, and 30%. As for the optimized stents, the auxetic properties, disturbances to the blood flow, and distributions of WSS are numerical validated and calculated, respectively.

6.1 Validation of auxetic deformation behaviors

The auxetic property is one of the essential design objectives for stents in the proposed optimization model. Although the effective elasticity tensors of the three optimized microstructures show significant NPRs, the validations of the auxetic properties for the related stenting macrostructures are still necessary. Since the effective properties of the three microstructures exhibit directional differences in the two main directions, two compression tests are performed: one is to apply a radial compression load; another one

is to apply an axial compression load. In the validations, the stenting geometries based on the optimization results need to be created. At first, the optimized microstructures are obtained from MATLAB via the STL type, and the software SpaceClaim integrated into ANSYS is further utilized to finish the creating.

6.1.1 The radial compression tests

From the effective elasticity tensors of the three stents, it can be found that their properties have directional differences. The vertical stiffness is smaller than the horizontal. Thus, when the optimized microstructures are utilized for stents, the stents will exhibit different NPRs in the radial and axial directions. Firstly, radial compression tests are performed for the three optimized stents to test one of the NPRs.

(A) Axonometric view　　　　　(B) Partially enlarged view
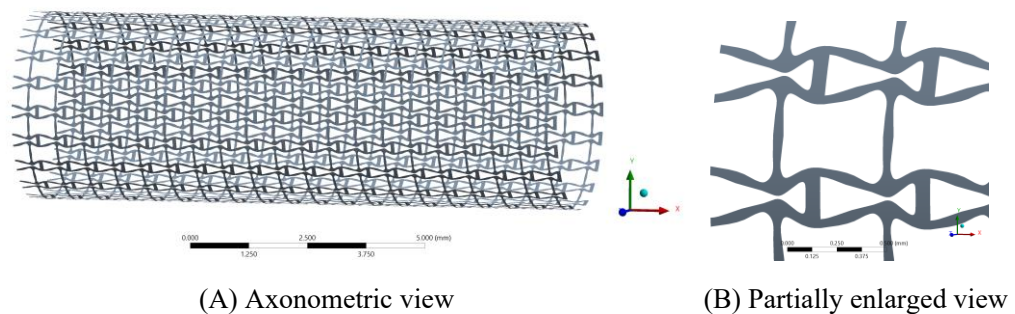
Figure 6-1 The geometry of F-7.

The geometry of the result F-7 is created in the software SpaceClaim which is integrated into ANSYS. As the proposed assumption, the stent consists of 20×20 periodic unit cells. The geometry of the optimized stent is shown in Figure 6-1. The stent thickness is 0.1 mm; the length and the diameter are 12 mm and 4 mm, respectively. In the model, 20 unit cells are defined along the peripheral direction and 20 unit cells along the axial direction.
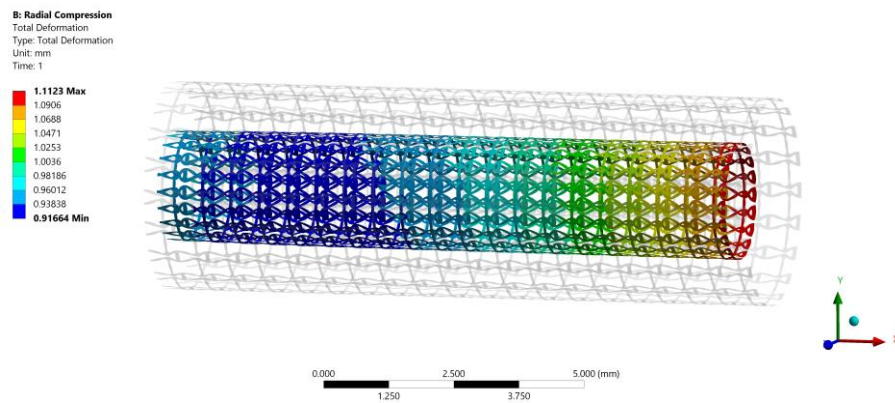
(A) Axonometric view
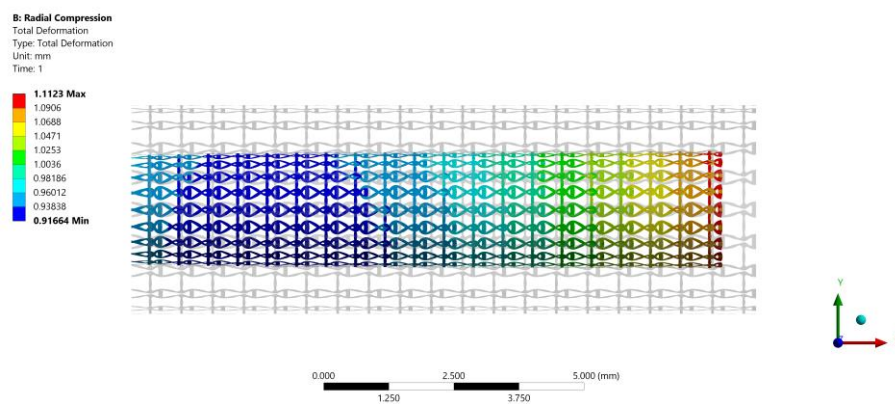
(B) Side view

Figure 6-2 The Compression test for F-7.

The deformation result of the radial compression test for F-7 is shown in Figure 6-2, where both axonometric and side views are utilized to present its deformation behavior. A pressure load is applied on the stenting surface to compress the diameter to about half size in the test. We can see the stent contracts a little small in the axial direction due to larger axial stiffness. Thus, part of the stent will be compressed when adapting to the various artery shapes, changing the radial sizes, but the stenting axial length is relatively stable. It can maintain enough length of the stent to completely cover the lesion even though the stenting radial dimension is changed.
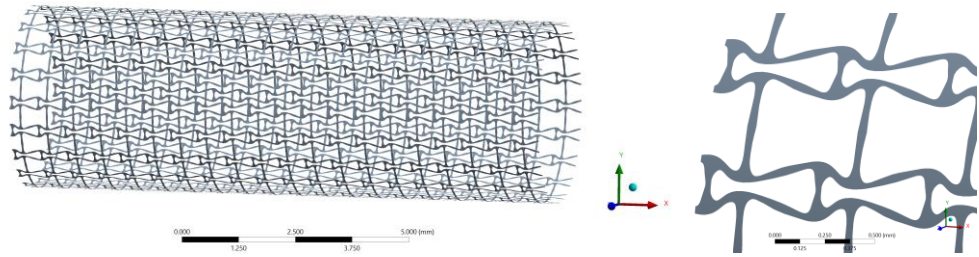
(A) Axonometric view　　　　　　(B) Partially enlarged view

Figure 6-3 The geometry of F-8.
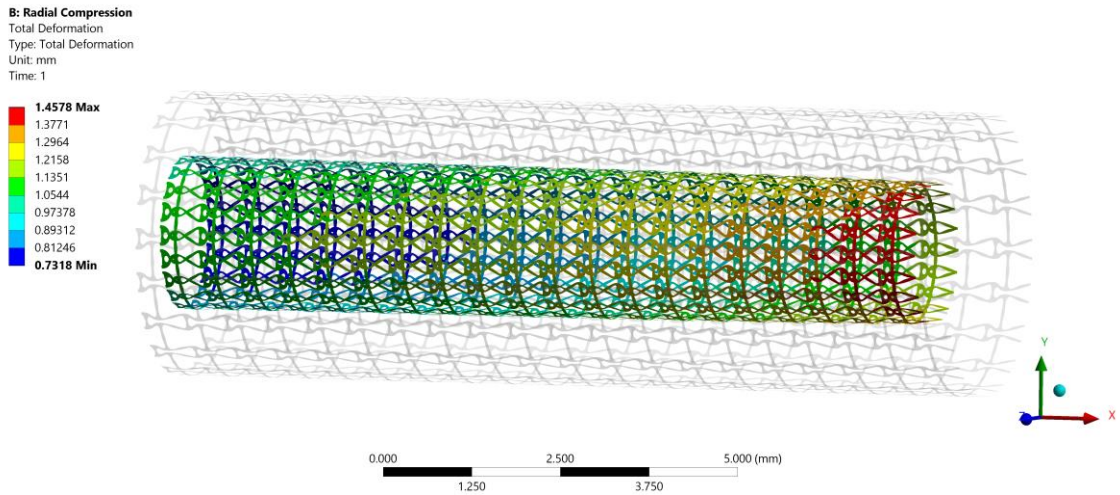
(A) Axonometric view
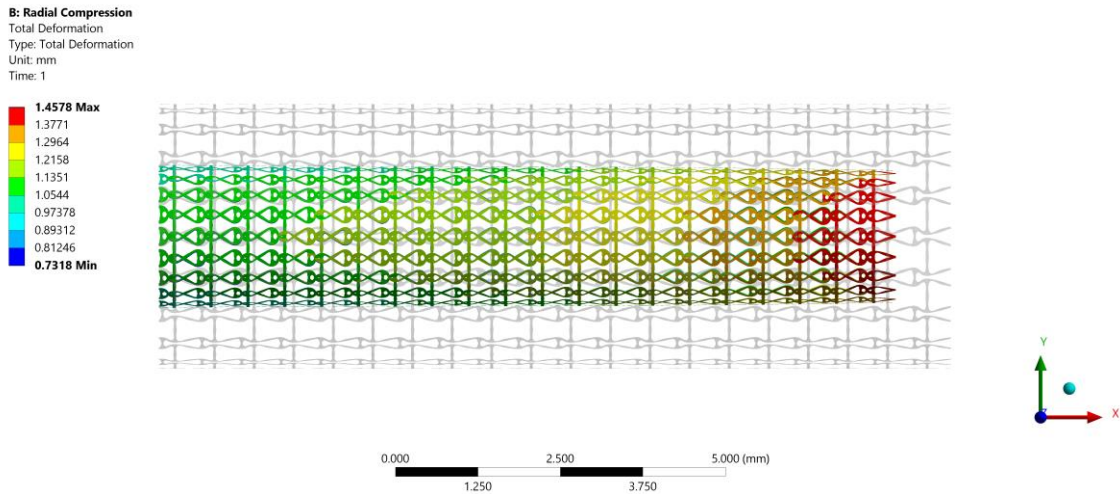
(B) Side view

Figure 6-4 The Compression test for F-8.

| (A) Axonometric view | (B) Partial enlarged view |
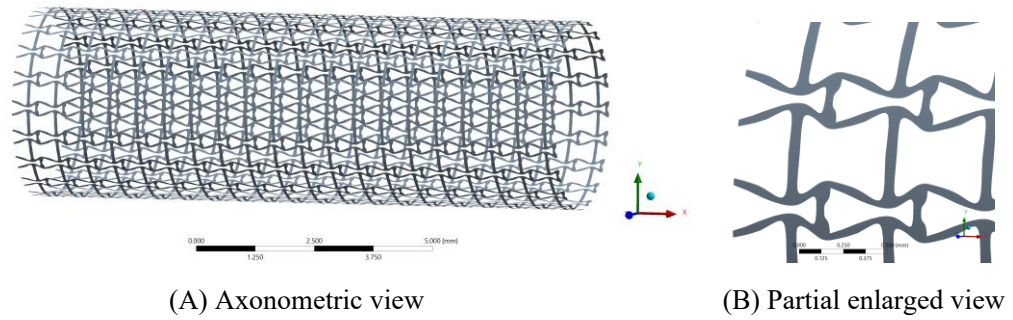
Figure 6-5 The geometry of G-7.

(A) Axonometric view

(B) Side view
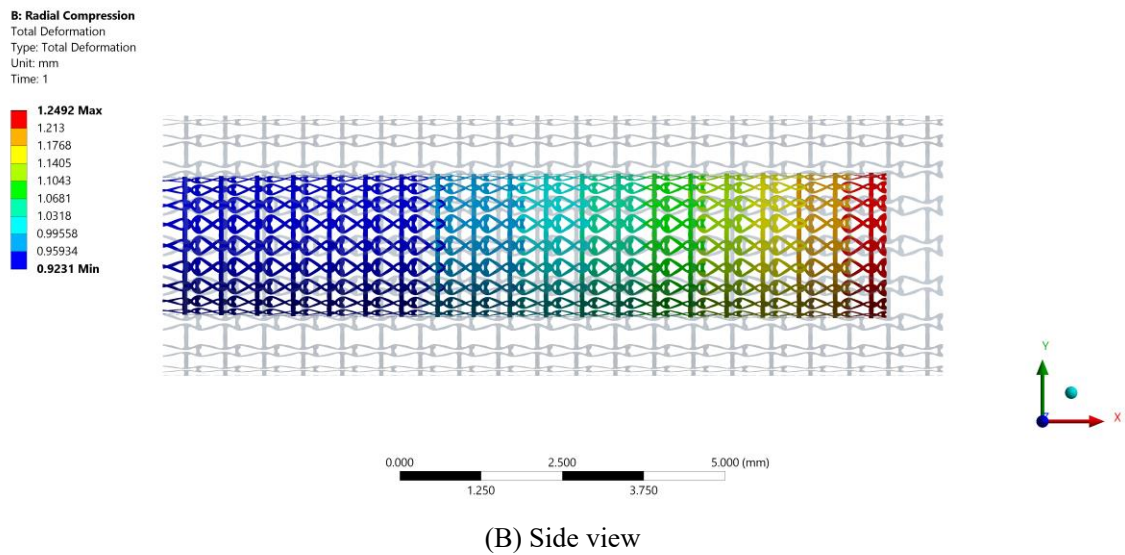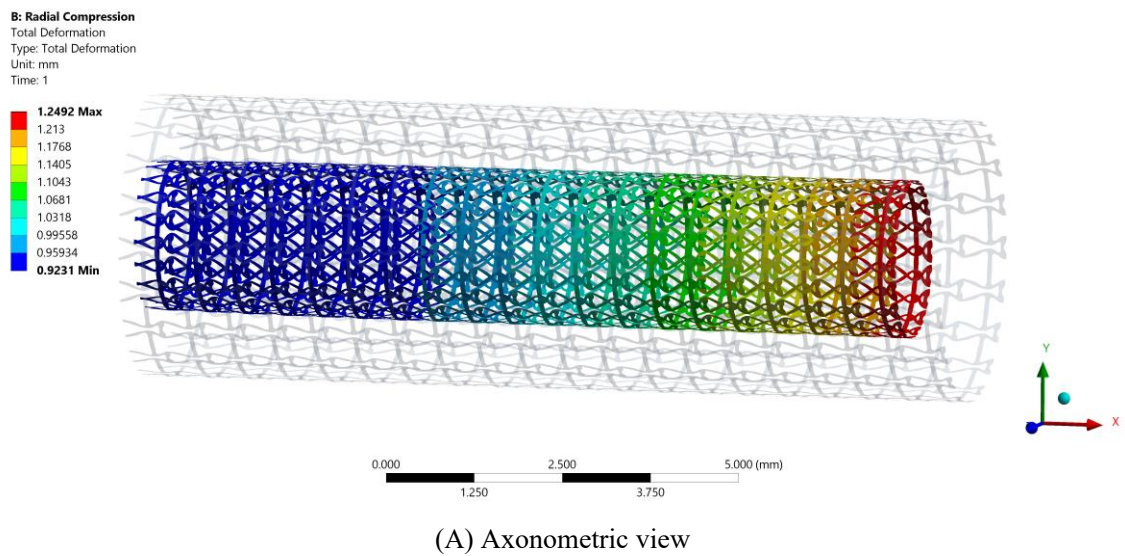
Figure 6-6 The Compression test for G-7.

Two more radial compression tests are performed to investigate the auxetic properties for the other two results of cases F-8 and G-7. The geometry of F-8 can be found in Figure 6-3, while the geometry of G-7 is in Figure 6-5. The deformations of the two stents in the tests are presented in Figures 6-4 and 6-6, respectively. From the results, we can see the two stents share similar deformation behaviors with F-6. Both stents will contract along the axis when they are compressed in the radial direction. The amounts of the contractions are relatively small compared with the radial deformations. It indicates that they have similar NPRs when performing radial compressions. Thus, on the one hand, the auxetic properties can make them easier to adapt to the radial deformations or the various artery shapes. On the other hand, they all can maintain relatively stable axial lengths of the stents.

6.1.2 The axial compression tests

Since the optimized stents exhibit different properties in the two main directions, the compression tests in another direction are also needed, where three axial compression tests are performed to validate the properties of the stents, respectively. The axial compression test results are presented in Figure 6-7. The test result shows that the stent obviously contracts in the radial direction when applying compression loads in the axial direction from the right side, indicating NPR behavior, resulting in a smaller compression volume to improve deliverability.
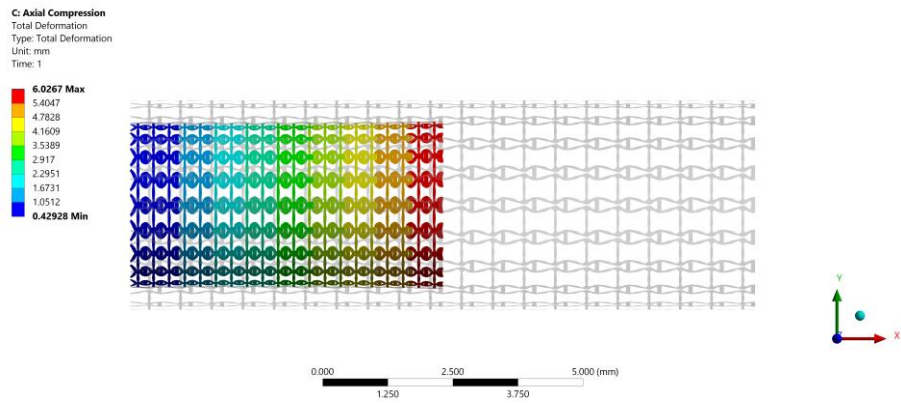
(A) The deformation of F-7 by Axial compression
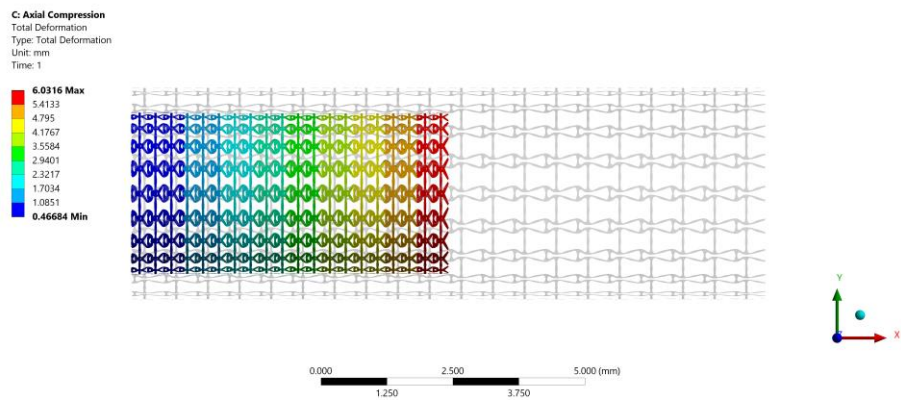
(B) The deformation of F-8 by Axial compression
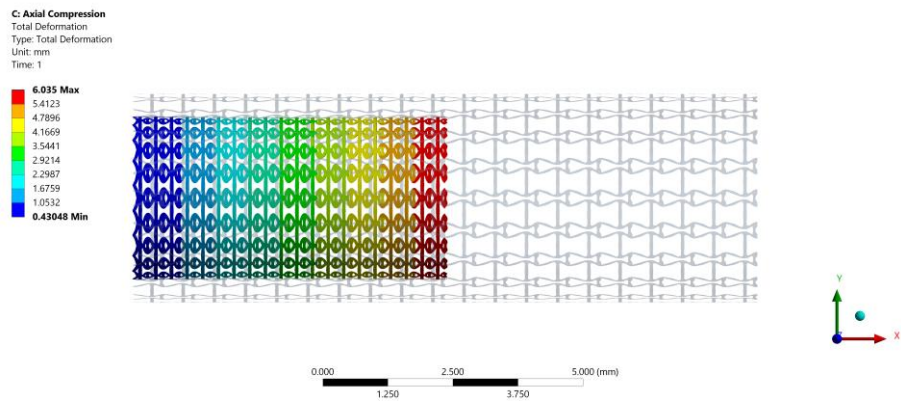
(C) The deformation of G-7 by Axial compression

Figure 6-7 The deformation results of the axial compression test.

Hence, from the results of the two compression tests, we can see the three optimized stents exhibit significant auxetic properties and have directional differences in the deformation behaviors in the two main directions. Moreover, the directional differences can maintain

large NPR behavior to benefit the mechanical properties of the stent and can also exhibit smaller vertical stuffiness to adapt to the radial deformations and various artery shapes easily. Since the benefits of introducing auxetic properties to the mechanical properties of the stent have been demonstrated in Chapter 4, the simulations here are only performed to validate the NPR deformation behaviors of the stents.

6.2 Blood flow in the stented segment

The disturbance of stents on blood flow is another essential issue of stent optimization. The simulations for blood flow through the stented segment are necessary to validate the optimization results. Hence, the software CFX in ANSYS is utilized to perform the fluid simulations for the optimized stents. In the validations, the distribution of WSS is used as one metric to evaluate the stents. Besides that, this thesis aims to minimize the adverse hemodynamic changes by reducing the disturbances induced by stents to the blood flow. Thus, the disturbed blood flows around stents also need to be investigated, where the streamlines generated by blood flow are extracted to present the disturbances.

6.2.1 Fluid validations for F-7
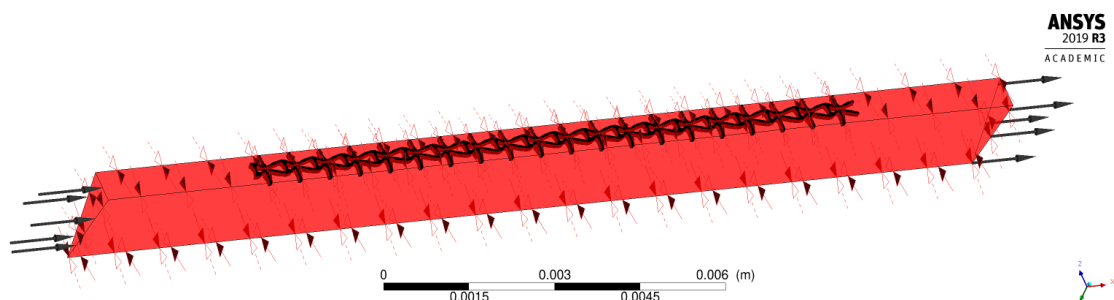
Figure 6-8 The CFD model for the stent F-7.

By considering the computational cost, the CFD model is established based on only 1 unit

cell along the peripheral direction and 20 unit cells in the axial direction, as shown in Figure 6-8, where the black one is the stent, and the red one is blood. The stent thickness is 0.1 mm; the length and the diameter are 12 mm and 4 mm, respectively. By considering the impact of the boundary conditions on flow, the distance between the inlet and the stent struts is specified as 3mm and another 3 mm between the outlet and the stent. The blood in the model is defined as an incompressible Newtonian viscous fluid. The density is 1050 Kg/m3; the dynamic viscosity is 3.5 mPa·s. The flow is assumed as a steady-state with 0.35 m/s inflow velocity and 0 Pa outlet boundary condition, and no-slip conditions are applied on the fluid-solid interfaces and the fluid walls. The cylindrical symmetric boundary condition is defined in the peripheral direction.
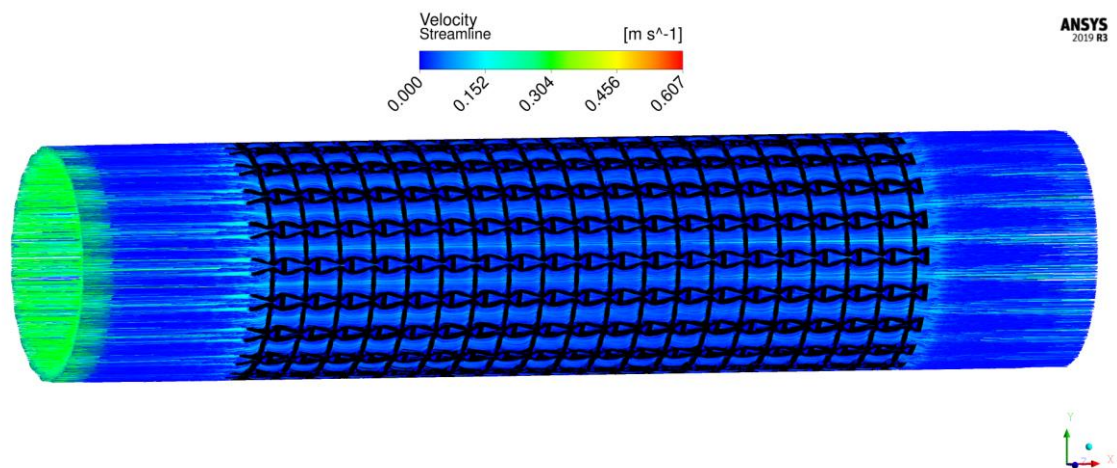
Figure 6-9 The streamlines of blood around the stent F-7.

The results of blood flow streamlines are obtained to investigate the stent disturbances, as shown in Figure 6-9, where the lower velocities of the streamlines are printed with darker colours. In the figure, the maximum velocity of the flow is greater than the inflow condition, which is because the flow can be accelerated around the stent struts. Due to the

applied no slid boundary conditions, the minimum velocity is zero. From Figure 6-9, we can find that velocities of the streamlines are affected by the stenting struts. Since relatively narrow spaces are formed between the horizontal struts in each unit cell, the blood flows are obstructed around these spaces and exhibits lower velocities. Moreover, the blood flows between each unit cell can maintain higher speeds due to fewer obstructions and larger fluid areas. Overall, blood flow can keep a high velocity, which can be found that many streamlines with light colours through the whole fluid region.

The overall influences of stenting obstructions can be evaluated by blood flow changes in the upstream side and downstream side of the stent. Thus, the effects of stent design on the blood flow are further investigated by the streamlines in the proximal and distal unit cells of the stent. The streamlines in the proximal and distal struts are presented in Figures 6-10 and 6-11, respectively. In the figure, the fluid region around the stent can be divided into two kinds of spaces: one is the inner space of each unit cell; another one is the connecting space between unit cells. When blood through these spaces, the flow can be accelerated around the struts and may lead to recirculation zones. In the connecting spaces of the proximal struts, the disturbances to the blood flow focus on the four corners and cause small recirculation zones, especially for the corners behind the struts. Besides that, a few vertical flows occur along the left struts in the connecting spacings. However, small recirculation zones are also formed around the vertical struts in the inner spaces of proximal struts due to the narrow fluid spaces. Compared with the proximal struts, similar blood flow behaviors can be found around the distal struts but exhibit relatively smaller flow disturbances and recirculation zones. Although the recirculation zones may induce adverse effects, they only cover very few regions around different struts' connections. Hence, the result shows that the optimization for the MFP of the stent effectively reduces

the vertical flow, which can essentially reduce the stenting obstructions to benefit blood flow.
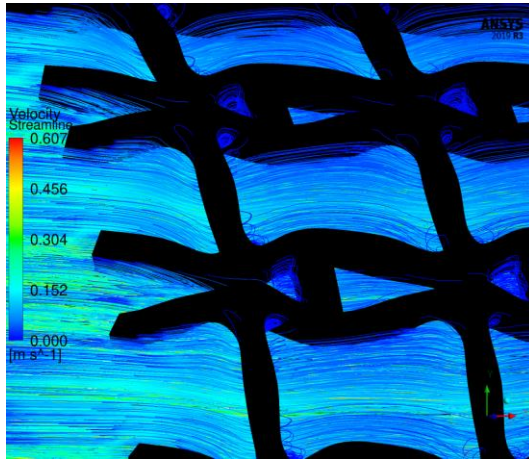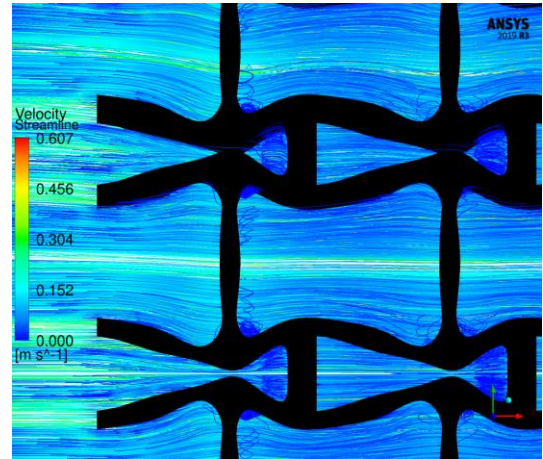
(A) Axonometric view   (B) Side view

Figure 6-10 The streamlines of blood around the proximal struts of the stent F-7.

(A) Axonometric view   (B) Side view

Figure 6-11 The streamlines of blood around the distal struts of the stent F-7.

As we know, the WSS is an important metric to quantify the hemodynamic impacts of implanting stents. The abnormal WSS is usually associated with adverse effects, such as ST (extremely high WSS) and ISR (extremely low WSS). It is investigated that the

magnitude of WSS higher than 2.5 Pa poses a risk of ST, while lower than 0.5 Pa increases ISR incidence. Based on the flow direction, the WSS magnitude is mainly determined by the axial component, so the axial WSS is utilized to evaluate the stent.
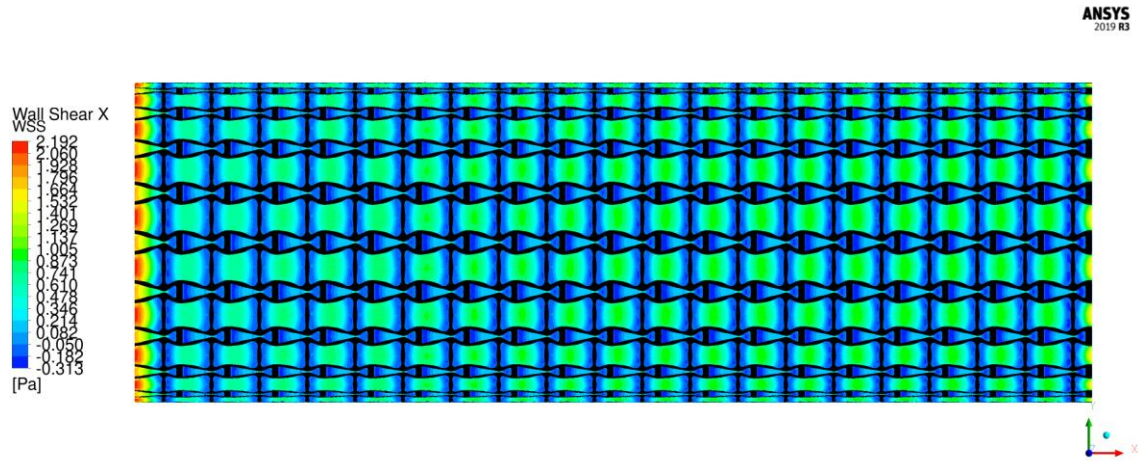
(A) Covered by stent
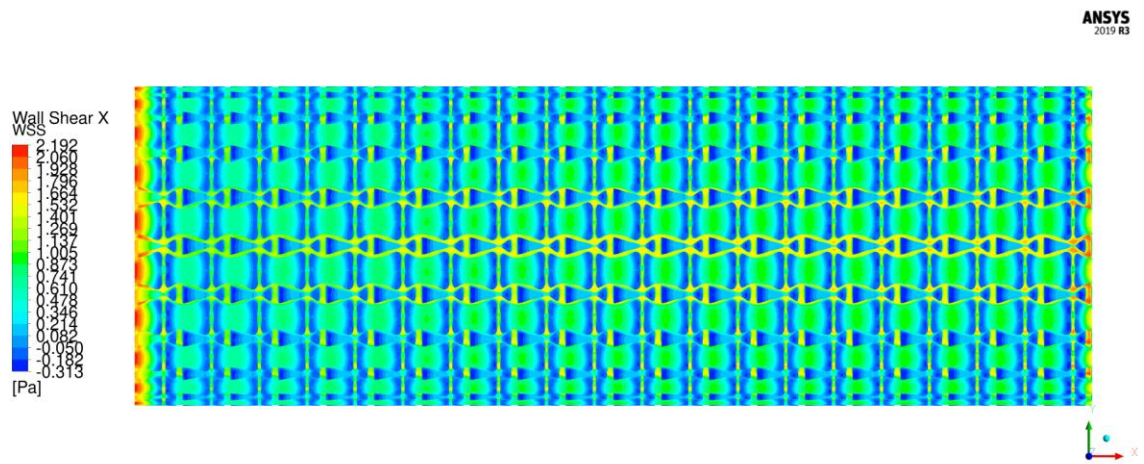
(B) Without stent

Figure 6-12 Axial WSS of the stent F-7.

The axial WSS of the stent is illustrated in Figure 6-12. It is easy to find that the regions

covered with the stent have higher WSS than uncovered regions. The WSS around the stent exhibits an increasing trend along the flow direction, except for the inlet and outlet sides. It is caused by the acceleration of stenting struts to the blood flow. In the results, the maximum axial WSS is 2.192 Pa and less than the high adverse stress 2.5 Pa, which indicates a lower incidence of ST. However, the regions surrounded by the stent struts exhibit lower and even negative axial WSS, indicating recirculation zones. The same recirculation zones are also detected in the streamline results. Among that, the connecting spaces between unit cells have higher WSS compared with their inner spaces due to larger fluid regions. The average WSS in most regions of the stent is around 1 Pa and greater than the lower bound of the threshold 0.5 Pa, but the areas close to the vertical struts exhibit smaller, even negative WSS. It is because the struts protruding into the artery lumen disrupt and separate the laminar flow, resulting in lower shear rates around the struts. This kind of effect is determined by the shape and size of the strut profiles but cannot be eliminated unless the stent is fully embedded into the artery walls. Although the regions with lower WSS cannot be completely avoided, few areas are under the impact. Moreover, the WSS distribution of the stent is relatively uniform, which can also benefit the reducing the incidence of ST and ISR. Thus, the validations for the other two stents are performed in the following to compare their results.

6.2.2 Fluid validations for F-8

The blood flow streamlines around the stent F-8 are presented in Figure 6-13. It is easy to find that the blood flow streamlines located at the lower position of the unit cells can still retain higher velocities, exhibiting the streamlines with light colours through the whole fluid region. Most of the fluid regions with high flow velocities are located at the

connecting spaces of the stent due to the relatively large fluid fields. The streamline results of F-8 are similar to F-7. It indicates that the opening locations of the stenting microstructures cannot induce too many differences in the obstructions. That is because the openings of these structures are located at the inlet side and outlet side. Both openings orient the flow direction. Moreover, the maximum velocity of the flow around the stent F-8 is a little faster than the stent F-7.
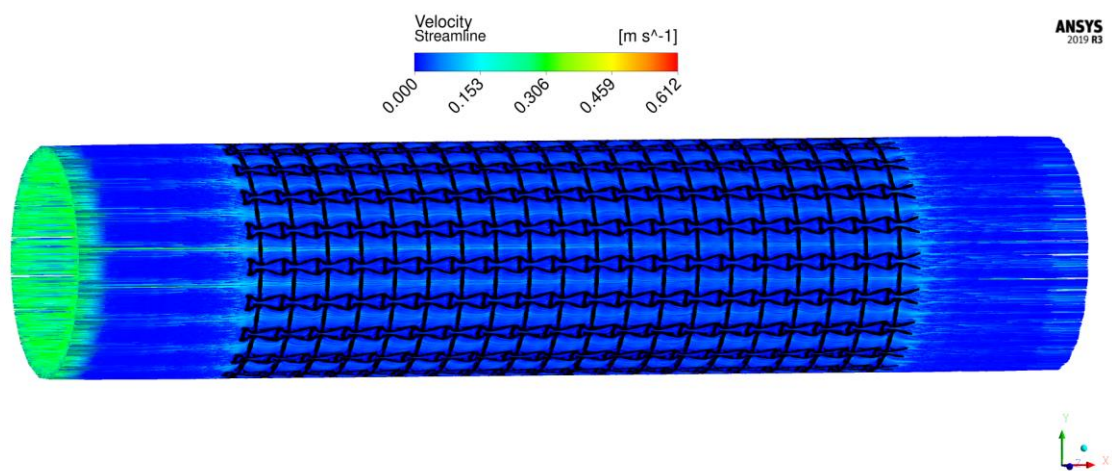
Figure 6-13 The streamlines of blood around the stent F-8.

The streamlines in the proximal and distal struts of the stent F-8 are shown in Figures 6-14 and 6-15, respectively. Although the opening location in F-8 is different from F-7, their distributions of the disturbed flows are very similar. The disturbances to the blood flow are also mainly located at the inner spaces of the unit cells and forming recirculation zones in the narrow upstream spaces. However, recirculation zones are formed at both ends of the inner spaces in F-8, compared with only one side in F-7. Because of thinner struts, the recirculation zones and impact regions are smaller than the results of F-7.
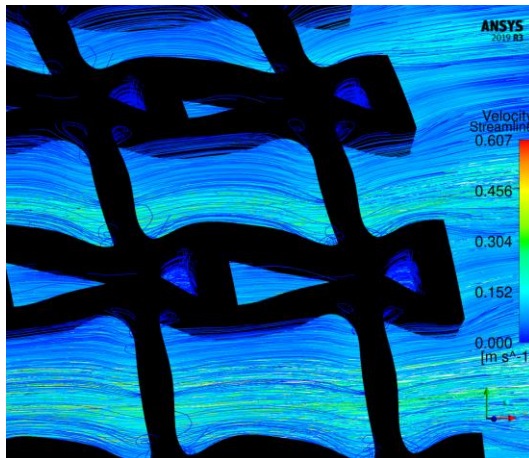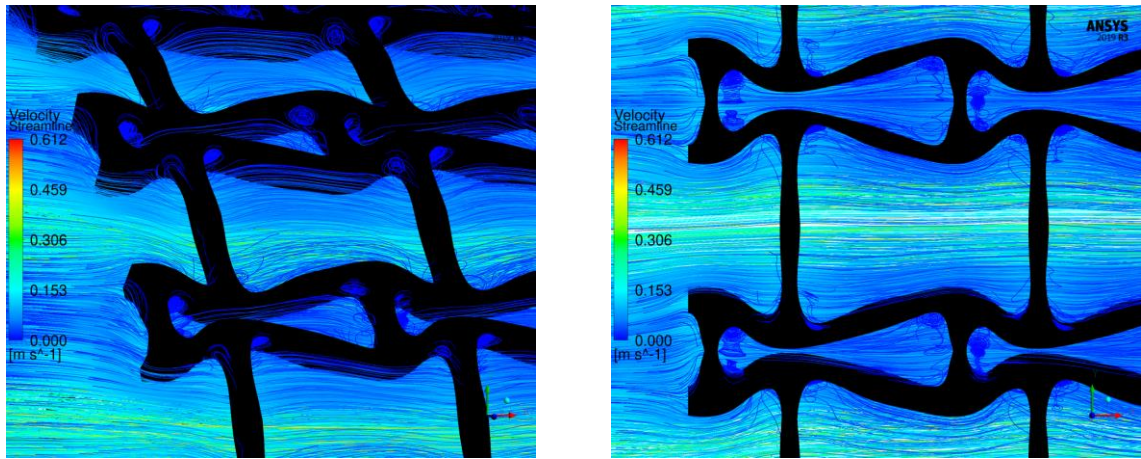
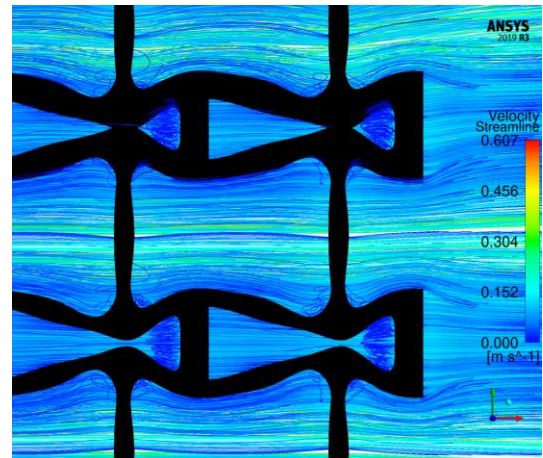(A) Axonometric view   (B) Side view

Figure 6-14 The streamlines of blood around the proximal struts of the stent F-8.
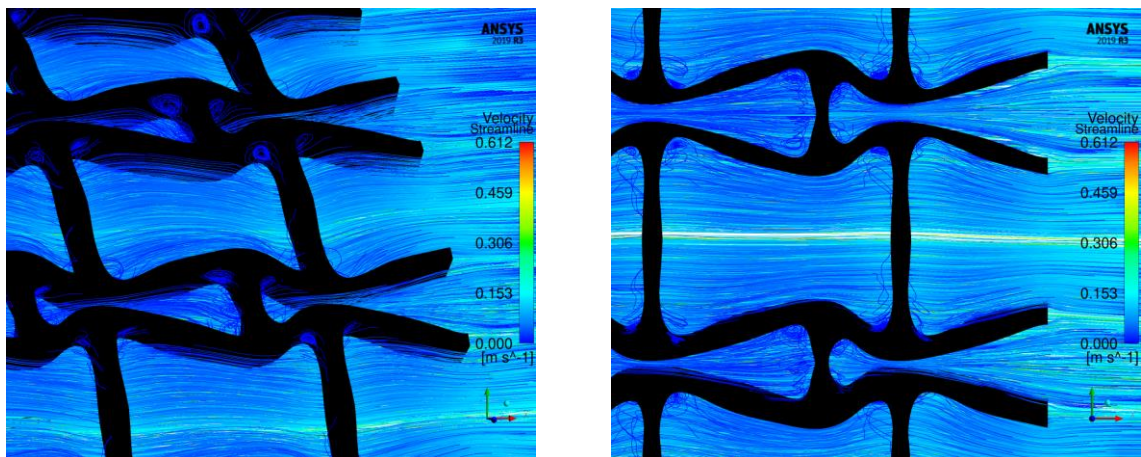

(A) Axonometric view   (B) Side view

Figure 6-15 The streamlines of blood around the distal struts of the stent F-8.

The axial WSS of F-8 is calculated to investigate the fluid behaviors in the stent regions, and the distributions are presented in Figure 6-16. The WSS distributions and changes are similar to the results of F-7, but with higher values. However, the maximum WSS in F-8 is 2.550 Pa, a little larger than the upper bound of the threshold. Although the regions with WSS greater than 2 Pa only exist in a narrow band around the outlet side, they still

pose risks of ST and may affect the hemodynamic environment behind the stent. Thus, the design of F-8.
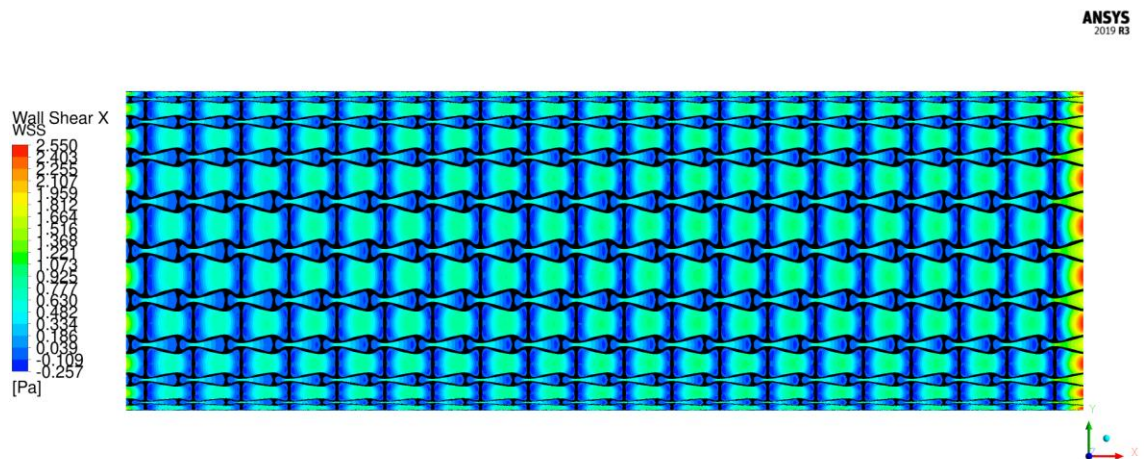
(A) Covered by stent
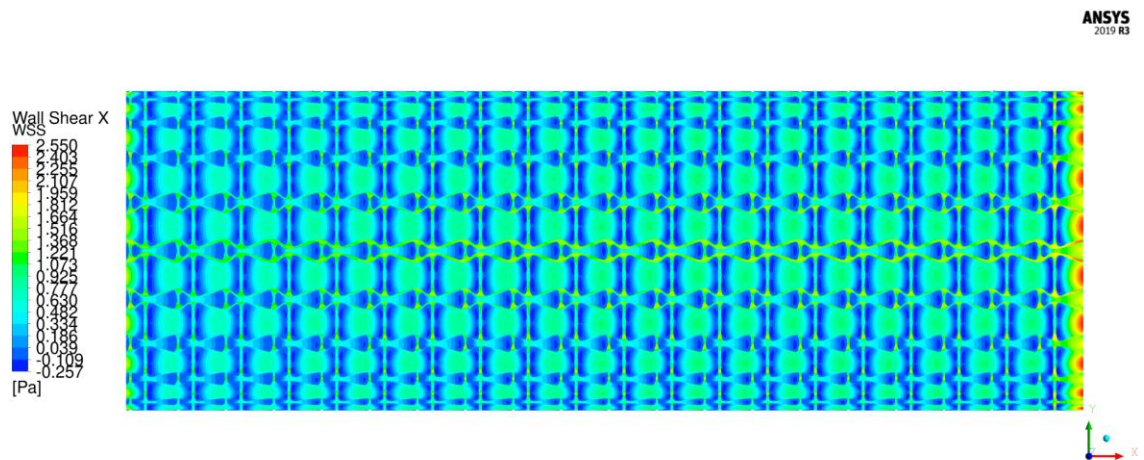
(B) Without stent

Figure 6-16 The distributions of WSS of the stent F-8.

6.2.3 Fluid validations for G-7

The geometric characteristics of G-8 are very similar to F-7, but with a thinner vertical

strut to connect the horizontal struts in each microstructure. Parts of the blood flow streamlines around the stent G-7 can also retain high velocities through the whole fluid domain, same as the stent F-7 but with a little faster maximum flow velocity, as shown in Figure 6-17. Additionally, more details of the streamlines in the proximal and distal struts of the stent G-7 can be found in the enlarged view in Figures 6-18 and 6-19, respectively. From the results, we can see that recirculation zones are formed at both ends of the inner spaces due to the concave boundaries of the vertical struts. However, the recirculation zones generated around the downstream sides of the inner spaces become smaller than the results of F-7.
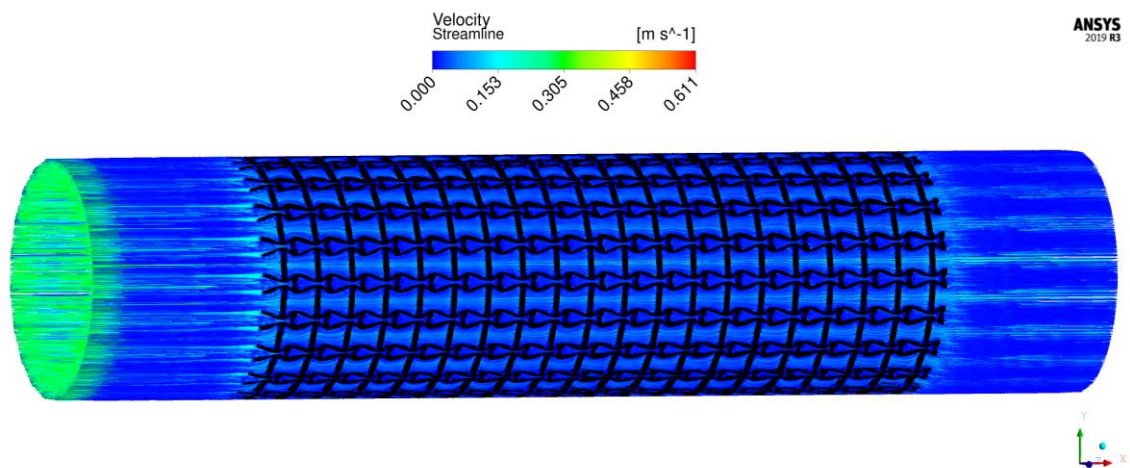
Figure 6-17 The streamlines of blood around the stent G-7.
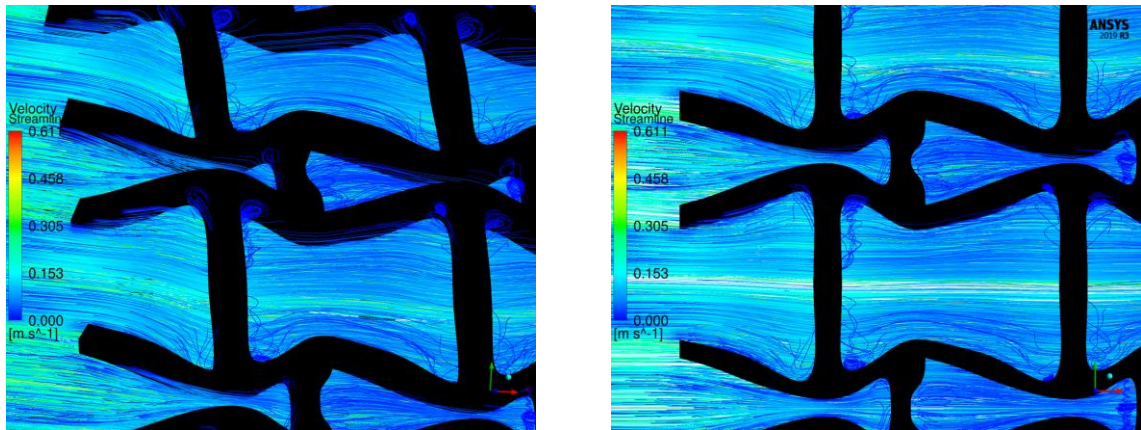
(A) Axonometric view   (B) Side view

Figure 6-18 The streamlines of blood around the proximal struts of the stent G-7.
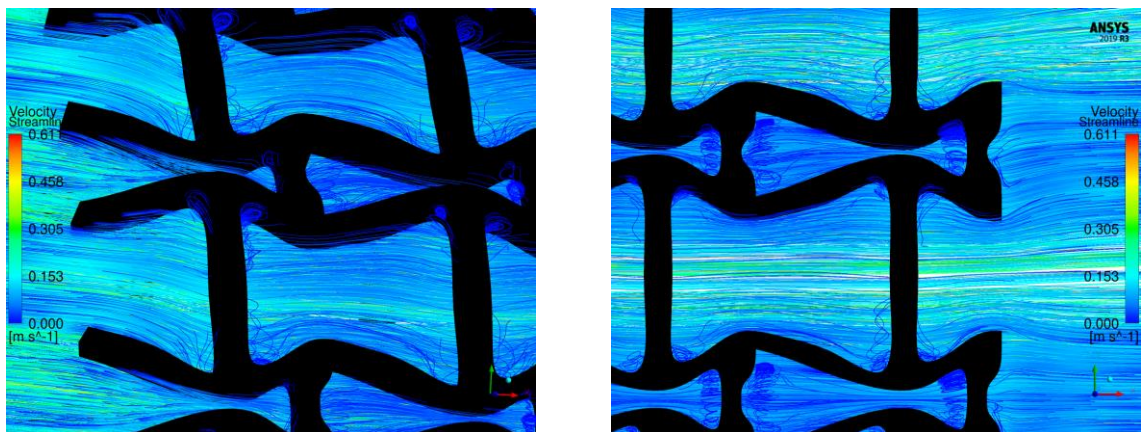
(A) Axonometric view   (B) Side view

Figure 6-19 The streamlines of blood around the distal struts of the stent G-7.

The axial WSS distributions of the stent G-7 is presented in Figure 6-20. The distributions are very similar to F-7. A similar maximum WSS value results in a lower incidence of ST. As for the lowest WSS, the magnitude of the minimum negative WSS in G-7 is less than F-7. It indicates that the recirculation zones are reduced, which is the same as the streamlines results, we discussed. The lower WSS occurs around the stent struts, and the recirculation zones are mainly formed in the inner spaces of the unit cells. Overall, the

stenting structures with openings at the inlet side exhibit better WSS results.
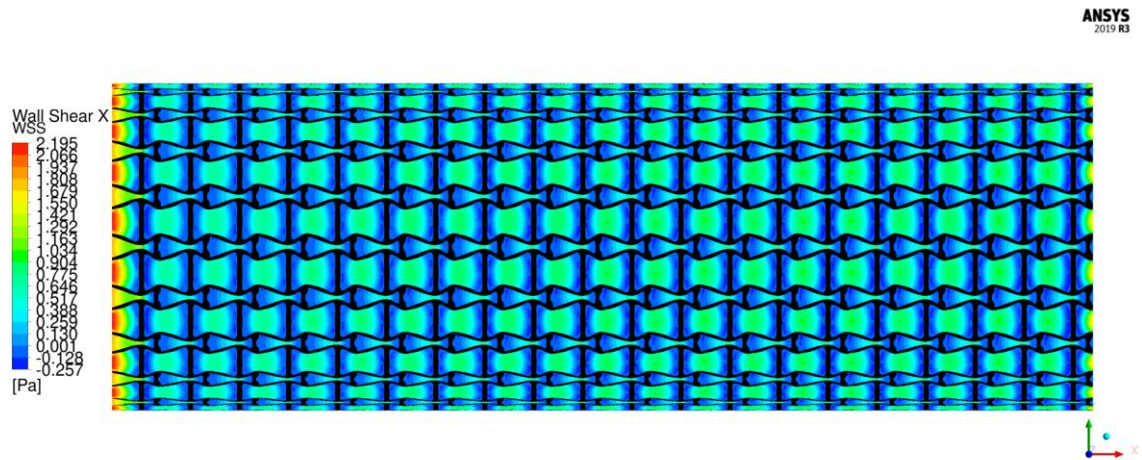
(A) Covered by stent
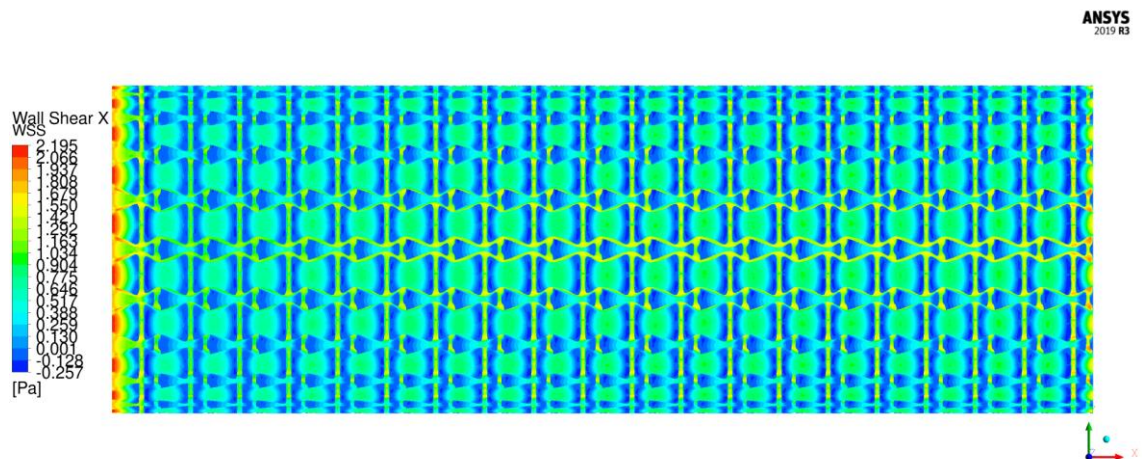
(B) Without stent

Figure 6-20 The distributions of WSS of the stent G-7.

6.3 Discussion and conclusion

The compression tests demonstrate that the three optimized stents exhibit significant

auxetic properties in both radial and axial directions. Besides that, the relatively smaller

radial stiffness can benefit the flexibility of stents and help keep a stable axial length of the stents during the deformation. In order to investigate the hemodynamic effects of the three stents, two kinds of results are utilized: blood flow streamlines and the axial WSS distributions. From the streamlines results, we can find that the streamlines through the connecting spaces of the three stents can still retain higher velocities than other locations, indicating fewer obstructions. The disturbances of stents to blood flow mainly occur around the struts, especially in their inner spaces, resulting in recirculation zones.

Table 6-1 The WSS results of the three optimized stents

Optimized stents	WSS(MAX Pa)	WSS(MIN Pa)
F-7	2.192	-0.313
F-8	2.550	-0.257
G-7	2.195	-0.257

As listed in Table 6-1, the results of the axial WSS distributions show that maximum WSS magnitudes of F-7 and G-7 are around 2.2 Pa less than the upper bound of the threshold 2.5 Pa, indicating lower risks of ST. However, the maximum WSS of F-8 is 2.55 exceed the upper bound of the threshold. It indicates that the stenting structures with openings at the inlet side can prevent extremely high WSS to some extend in these cases. On the other hand, due to the stenting obstructions, the lower WSS occurs around the struts. The disturbances or lower WSS regions cannot be eliminated unless the stent is fully embedded into the artery walls but can be reduced by changing the structures of stents. Besides that, the conventional stent designs are usually hard to consider all the geometric factors of the induced hemodynamic changes. Thus, most of them exhibit extreme WSS higher than the threshold, while the WSS values in the recirculation zones are usually much lower than the optimized stents.

In this chapter, a homogenized effective MFP is proposed to measure the disturbances of the stenting periodic microstructures on the blood flow. Based on the parametric level set method, a multi-objective multiscale optimization model is then established for the design of SE stents. In the model, three design objectives are defined: the first one is to introduce auxetic properties to enhance mechanical properties of the stent and benefit deliverability and flexibility; the second one is to minimize the vertical MFP of the stenting microstructure to reduce the adverse hemodynamic changes caused by implanting stents and finally decrease the incidences of ST and ISR; the third one is to maximize the stiffness of the macroscopic stent. The numerical examples and simulations show that the topologically optimized structures exhibit significant auxetic properties and higher radial stiffness of the stents and show the effectivity of the MFP optimization on reducing blood flow disturbances, which can benefit blood flow and finally reduce the risks of ST and ISR. Additionally, the material distributions of the stenting microstructures are successfully associated with the adverse blood flows via the MFP. Thus, the topology optimization can be easily applied for the related stent designs to obtain new structural layouts and eliminate the dependencies of initial designs, which is the limitation in most optimization designs for stents. In other words, all the structural characteristics of the stent can be taken into account to reduce the adverse hemodynamic effects of implanting stents. In future studies, the pulsatile blood flow state will be considered to get more accurate fluid behaviors.

Chapter 7 Conclusion and prospect

7.1 Summary

This thesis develops systematic topology optimization methods for coronary artery stent designs to reduce the risks of ST and ISR by preventing mechanical failures and adverse hemodynamic changes. Among that, auxetic metamaterials are applied to enhance the mechanical performances of stents to prevent mechanical failures. On the other hand, the proposed MFP efficiently quantifies the obstructions of stents on the blood flow and is applied in the optimization to reduce the stent induced adverse hemodynamic changes.

In Chapter 2, a comprehensive literature review is provided for coronary artery stents and topology optimization. At first, the developments of different coronary artery stents are reviewed to show their advantages and existing problems. Then, the mechanical failures and adverse hemodynamic changes caused by stenting structures are discussed to explain the associations between the structural characteristics and complications. Besides that, the current structural optimization design methods for stents are summarized. The issue of highly initial design-dependent in current stent optimization methods are discussed as well. In the aspect of topology optimization, different approaches are reviewed and discussed. Moreover, the application of topology optimization design in artificial functional cellular composites is also discussed. Finally, the review of auxetic metamaterials and their unusual properties are presented.

In Chapter 3, the PLSM and the involved interpolation based on CSRBFs are introduced. After that, the X-PLSM is developed to transform the level set function from the cartesian coordinate system to a curvilinear system. Thus, the X-PLSM can implicitly represent the boundaries of shell structures efficiently rather than using the 3D PLSM models, which can benefit the design of stents.

In Chapter 4, the abilities of SE stents on addressing the mechanical failures are explained. Then, the benefits of auxetic metamaterials to SE stents are presented. Thus, the purpose of optimizing the stenting structures to prevent mechanical failures is transformed to introduce auxetics in SE stents to enhance the mechanical performances and improve the applications. After that, a multiscale topology optimization based on X-PLSM is developed to introduce auxetics into the design of SE stents. The numerical validations in ANSYS show that the optimized auxetic SE stent exhibit significant auxetic properties and good flexibility, and the new stent can help overcome the drawbacks of conventional SE stents. Additionally, the optimized stent is prototyped using additive manufacturing techniques.

In Chapter 5, by adopting the Darcy-Stokes coupling system, the MFP is proposed to quantify the obstructions of stents to the blood flow. It successfully transforms the optimization of reducing stent induced adverse hemodynamic changes into a model to minimize the MFP in other directions except for the blood flow direction. On the other hand, we intend to utilize the auxetics to enhance the mechanical performances of the stent. Thus, a multiscale multi-objective topology optimization based on PLSM is

developed for SE stents to introduce auxetics, maximize macroscopic stiffness, and minimize the stent induced obstructions quantified by MFP. The contribution of each design objective to the optimization result is determined via the investigations of the relevant three weight factors. The properties of optimized stents exhibit directional differences in the structures. They have larges MFP in the axial direction to facilitate blood flow and smaller MFP along the circumference direction to reduce the obstructions. As for the mechanical properties, the structures exhibit relatively smaller radial stiffness, resulting in good flexibility. Simultaneously, the large axial stiffness can maintain smaller changes in stent length when generating radial deformations. It can ensure the stent to cover the lesions efficiently.

In Chapter 6, the numerical validations in software ANSNS and CFX demonstrate the directional differences of the stenting properties. Besides that, the WSS distributions of the stents are also simulated, whose results illustrate the efficiency of the MFP in hemodynamic optimization.

Overall, this project successfully realizes the stent structural design by using level set based topology optimization method. In the respect of stent mechanical performances, the design of auxetic metamaterials overcome the drawbacks of SE stents and enhance the mechanical properties. In the respect of stent induced adverse hemodynamic changes, the proposed MFP associates all the stent structural features to a single design objective, and significantly reduces the amount of design variables and optimization objectives. And the numerical validations present the efficiency of the proposed optimization methods.

7.2 Prospect for future works

Although the project shows the efficiency of the proposed methods, some limitations are still needed to be addressed in the further works, such as including pulsatile blood flow state, improving the accuracy of the optimization model, considering more design objectives. The future works mainly focus on the following aspects:

In the thesis, the blood flow is assumed as a steady-state. Although some research works have already demonstrated that the steady-state is a reasonable assumption and acceptable in the stent design, the pulsatile blood flow state can get more accurate fluid behaviors. Thus, pulsatile blood flow behaviors will be considered in the optimization model in future works.

The auxetic metamaterials can enhance the mechanical performances for SE stent, but they can also be applied to the BE stent to address the foreshortening and improve flexibility. Moreover, the BE stents by using auxetic designs can also lead to a smaller initial structure before the expansion to improve the deliverability. Thus, the application of auxetics in BE stents will be investigated in the future.

The proposed X-PLSM can efficiently reduce the computational cost for stent design. However, when performing fluid optimization for stents, the X-PLSM is hard to take into account the effects of the thickness. Thus, in the next work, we will extend the X-PLSM to 3D curved elements to include more layers. And then, the optimization for stents will be directly performed for the 3D model. Among that, the MFP will also include the blood

flow in the radial direction.

There are many design requirements for stent structures. In current work, the applications of topology optimization methods in stent designs show the efficiency. Hence, in the future, we will utilize topology optimization to improve other properties of stents, such as recoil, fatigue, and drug release.

References

[1]   Canfield, J. and H. Totary-Jain, 40 Years of Percutaneous Coronary Intervention: History and Future Directions. Journal of personalized medicine, 2018, 8(4): 33.

[2]   Vos, T., et al., Global, regional, and national incidence, prevalence, and years lived with disability for 310 diseases and injuries, 1990–2015: a systematic analysis for the Global Burden of Disease Study 2015. The Lancet, 2016, 388(10053): 1545-1602.

[3]   Wang, H., et al., Global, regional, and national life expectancy, all-cause mortality, and cause-specific mortality for 249 causes of death, 1980–2015: a systematic analysis for the Global Burden of Disease Study 2015. The Lancet, 2016, 388(10053): 1459-1544.

[4]   Dotter, C.T. and M.P. Judkins, Transluminal Treatment of Arteriosclerotic Obstruction. Description of a New Technic and a Preliminary Report of Its Application. Circulation, 1964, 30(5): 654-70.

[5]   Gruntzig, A., Transluminal dilatation of coronary-artery stenosis. Lancet, 1978, 1(8058): 263.

[6]   Garg, S. and P.W. Serruys, Coronary stents: current status. Journal of the American College of Cardiology, 2010, 56(10 Suppl): S1-42.

[7]   Gruntzig, A.R., A. Senning, and W.E. Siegenthaler, Nonoperative dilatation of coronary-artery stenosis: percutaneous transluminal coronary angioplasty. The New England journal of medicine, 1979, 301(2): 61-8.

[8]   Venkitachalam, L., et al., Twenty-year evolution of percutaneous coronary intervention and its impact on clinical outcomes: a report from the National Heart, Lung, and Blood Institute-sponsored, multicenter 1985-1986 PTCA and 1997-2006 Dynamic Registries. Circulation. Cardiovascular Interventions, 2009, 2(1): 6-13.

[9]   Palmaz, J.C., et al., Expandable intraluminal graft: a preliminary study. Work in progress. Radiology, 1985, 156(1): 73-7.

[10]   Schatz, R.A., et al., Balloon-expandable intracoronary stents in the adult dog. Circulation, 1987, 76(2): 450-7.

[11]   Sigwart, U., et al., Intravascular stents to prevent occlusion and restenosis after transluminal angioplasty. The New England journal of medicine, 1987, 316(12): 701-6.

[12]   Roubin, G.S., et al., Intracoronary stenting for acute and threatened closure complicating percutaneous transluminal coronary angioplasty. Circulation, 1992, 85(3): 916-27.

[13]   Serruys, P.W., et al., Angiographic follow-up after placement of a self-expanding coronary-artery stent. The New England journal of medicine, 1991, 324(1): 13-7.

[14]   Serruys, P.W., et al., A comparison of balloon-expandable-stent implantation with balloon angioplasty in patients with coronary artery disease. Benestent Study Group. The New England journal of medicine, 1994, 331(8): 489-95.

[15]   Fischman, D.L., et al., A randomized comparison of coronary-stent placement and balloon angioplasty in the treatment of coronary artery disease. Stent Restenosis Study Investigators. The New England journal of medicine, 1994, 331(8): 496-501.

[16]   O'Brien, B. and W. Carroll, The evolution of cardiovascular stent materials and surfaces in response to clinical drivers: a review. Acta Biomaterialia, 2009, 5(4): 945-58.

[17]   Gori, T., et al., Predictors of stent thrombosis and their implications for clinical practice. Nature

Reviews. Cardiology, 2019, 16(4): 243-256.

[18] Mehta, S.R., et al., Effects of pretreatment with clopidogrel and aspirin followed by long-term therapy in patients undergoing percutaneous coronary intervention: the PCI-CURE study. Lancet, 2001, 358(9281): 527-33.

[19] Torrado, J., et al., Restenosis, Stent Thrombosis, and Bleeding Complications: Navigating Between Scylla and Charybdis. Journal of the American College of Cardiology, 2018, 71(15): 1676-1695.

[20] Bertrand, O.F., et al., Biocompatibility aspects of new stent technology. Journal of the American College of Cardiology, 1998, 32(3): 562-71.

[21] Heldman, A.W., et al., Paclitaxel stent coating inhibits neointimal hyperplasia at 4 weeks in a porcine model of coronary restenosis. Circulation, 2001, 103(18): 2289-2295.

[22] Colombo, A., et al., Preliminary observations regarding angiographic pattern of restenosis after rapamycin-eluting stent implantation. Circulation, 2003, 107(17): 2178-2180.

[23] Stettler, C., et al., Outcomes associated with drug-eluting and bare-metal stents: a collaborative network meta-analysis. Lancet, 2007, 370(9591): 937-48.

[24] Stone, G.W., et al., Safety and efficacy of sirolimus- and paclitaxel-eluting coronary stents. The New England journal of medicine, 2007, 356(10): 998-1008.

[25] Stone, G.W., et al., One-year clinical results with the slow-release, polymer-based, paclitaxel-eluting TAXUS stent: the TAXUS-IV trial. Circulation, 2004, 109(16): 1942-7.

[26] Joner, M., et al., Pathology of drug-eluting stents in humans: delayed healing and late thrombotic risk. Journal of the American College of Cardiology, 2006, 48(1): 193-202.

[27] Palmerini, T., et al., Long-term safety of drug-eluting and bare-metal stents: evidence from a comprehensive network meta-analysis. Journal of the American College of Cardiology, 2015, 65(23): 2496-2507.

[28] O'Brien, B.J., et al., A platinum–chromium steel for cardiovascular stents. Biomaterials, 2010, 31(14): 3755-3761.

[29] Kalra, A., et al., New-generation coronary stents: current data and future directions. Current Atherosclerosis Reports, 2017, 19(3): 14.

[30] Tomberli, B., A. Mattesini, G.I. Baldereschi, and C. Di Mario, A brief history of coronary artery stents. Revista Española de Cardiología (English Edition), 2018, 71(5): 312-319.

[31] Räber, L., et al., Very late coronary stent thrombosis of a newer-generation everolimus-eluting stent compared with early-generation drug-eluting stents: a prospective cohort study. Circulation, 2012, 125(9): 1110-1121.

[32] Kufner, S., et al., Randomized trial of polymer-free sirolimus-and probucol-eluting stents versus durable polymer zotarolimus-eluting stents: 5-year results of the ISAR-TEST-5 trial. JACC: Cardiovascular Interventions, 2016, 9(8): 784-792.

[33] Kang, S.H., et al., Biodegradable-polymer drug-eluting stents vs. bare metal stents vs. durable-polymer drug-eluting stents: a systematic review and Bayesian approach network meta-analysis. European Heart Journal, 2014, 35(17): 1147-58.

[34] Windecker, S., et al., Biolimus-eluting stent with biodegradable polymer versus sirolimus-eluting stent with durable polymer for coronary revascularisation (LEADERS): a randomised non-inferiority trial. The Lancet, 2008, 372(9644): 1163-1173.

[35] Kereiakes, D.J., et al., Efficacy and safety of a novel bioabsorbable polymer-coated, everolimus-eluting coronary stent: the EVOLVE II Randomized Trial. Circulation: Cardiovascular Interventions,

2015, 8(4): e002372.

[36]   Kereiakes, D.J., Y. Onuma, P.W. Serruys, and G.W. Stone, Bioresorbable vascular scaffolds for coronary revascularization. Circulation, 2016, 134(2): 168-182.

[37]   McMahon, S., et al., Bio-resorbable polymer stents: a review of material progress and prospects. Progress in Polymer Science, 2018, 83: 79-96.

[38]   Mattesini, A., et al., Absorb vs. DESolve: an optical coherence tomography comparison of acute mechanical performances. EuroIntervention: journal of EuroPCR in collaboration with the Working Group on Interventional Cardiology of the European Society of Cardiology, 2016, 12(5): e566.

[39]   Duerig, T. and M. Wholey, A comparison of balloon-and self-expanding stents. Minimally invasive therapy & allied technologies, 2002, 11(4): 173-178.

[40]   Lu, H., et al., Five-year clinical follow-up of the STENTYS self-apposing stent in complex coronary anatomy: a single-centre experience with report of specific angiographic indications. Netherlands heart journal : monthly journal of the Netherlands Society of Cardiology and the Netherlands Heart Foundation, 2018, 26(5): 263-271.

[41]   Pellegrini, D. and B. Cortese, Focus on STENTYS((R)) Xposition S Self-Apposing((R)) stent: a review of available literature. Future cardiology, 2019, 15(3): 145-159.

[42]   Pyxaras, S.A., T. Schmitz, and C.K. Naber, The STENTYS self-apposing® stent. EuroIntervention, 2015, 11(Suppl V): V147-V148.

[43]   Schmidt, T. and J.D. Abbott, Coronary Stents: History, Design, and Construction. Journal of clinical medicine, 2018, 7(6): 126.

[44]   Kidawa, M., et al., Self-expanding STENTYS stents in daily routine use. Kardiologia Polska, 2017, 75(6): 554-563.

[45]   Lim, D., et al., Suggestion of potential stent design parameters to reduce restenosis risk driven by foreshortening or dogboning due to non-uniform balloon-stent expansion. Annals of Biomedical Engineering, 2008, 36(7): 1118-1129.

[46]   Duerig, T., D. Tolomeo, and M. Wholey, An overview of superelastic stent design. Minimally invasive therapy & allied technologies, 2000, 9(3-4): 235-246.

[47]   Foin, N., et al., Incomplete stent apposition causes high shear flow disturbances and delay in neointimal coverage as a function of strut to wall detachment distance: implications for the management of incomplete stent apposition. Circulation. Cardiovascular Interventions, 2014, 7(2): 180-9.

[48]   Stoeckel, D., C. Bonsignore, and S. Duda, A survey of stent designs. Minimally invasive therapy & allied technologies, 2002, 11(4): 137-147.

[49]   Karanasiou, G.S., et al., Stents: Biomechanics, Biomaterials, and Insights from Computational Modeling. Annals of Biomedical Engineering, 2017, 45(4): 853-872.

[50]   Chen, C., et al., Experimental and numerical simulation of biodegradable stents with different strut geometries. Cardiovascular engineering and technology, 2020, 11(1): 36-46.

[51]   Tammareddi, S., G. Sun, and Q. Li, Multiobjective robust optimization of coronary stents. Materials & Design, 2016, 90: 682-692.

[52]   Bressloff, N.W., G. Ragkousis, and N. Curzen, Design Optimisation of Coronary Artery Stent Systems. Annals of Biomedical Engineering, 2016, 44(2): 357-67.

[53]   Blair, R.W., N.J. Dunne, A.B. Lennon, and G.H. Menary, Multi-objective optimisation of material properties and strut geometry for poly(L-lactic acid) coronary stents using response surface

methodology. PLoS ONE, 2019, 14(8): e0218768.

[54] Putra, N.K., et al., Multiobjective design optimization of stent geometry with wall deformation for triangular and rectangular struts. Medical & Biological Engineering & Computing, 2019, 57(1): 15-26.

[55] Rigattieri, S., A. Sciahbasi, and P. Loschiavo, The clinical spectrum of longitudinal deformation of coronary stents: from a mere angiographic finding to a severe complication. The Journal of invasive cardiology, 2013, 25(5): E101-E105.

[56] Petrini, L., F. Migliavacca, F. Auricchio, and G. Dubini, Numerical investigation of the intravascular coronary stent flexibility. Journal of Biomechanics, 2004, 37(4): 495-501.

[57] Shen, X., et al., Multi-Objective Optimization Design of Balloon-Expandable Coronary Stent. Cardiovascular engineering and technology, 2019, 10(1): 10-21.

[58] Li, H., et al., Multi-objective optimization of coronary stent using Kriging surrogate model. Biomedical Engineering Online, 2016, 15(2): 148.

[59] Alaimo, G., F. Auricchio, M. Conti, and M. Zingales, Multi-objective optimization of nitinol stent design. Medical Engineering & Physics, 2017, 47: 13-24.

[60] Azaouzi, M., N. Lebaal, A. Makradi, and S. Belouettar, Optimization based simulation of self-expanding Nitinol stent. Materials & Design, 2013, 50: 917-928.

[61] Chen, C., et al., In vivo and in vitro evaluation of a biodegradable magnesium vascular stent designed by shape optimization strategy. Biomaterials, 2019, 221: 119414.

[62] Farhan Khan, M., et al., A novel approach to design lesion-specific stents for minimum recoil. Journal of Medical Devices, 2017, 11(1).

[63] James, K.A. and H. Waisman, Layout design of a bi-stable cardiovascular stent using topology optimization. Computer Methods in Applied Mechanics and Engineering, 2016, 305: 869-890.

[64] Beier, S., et al., Hemodynamics in Idealized Stented Coronary Arteries: Important Stent Design Considerations. Annals of Biomedical Engineering, 2016, 44(2): 315-29.

[65] Gijsen, F., et al., Expert recommendations on the assessment of wall shear stress in human coronary arteries: existing methodologies, technical considerations, and clinical applications. European Heart Journal, 2019, 40(41): 3421-3433.

[66] Van der Heiden, K., et al., The effects of stenting on shear stress: relevance to endothelial injury and repair. Cardiovascular Research, 2013, 99(2): 269-75.

[67] LaDisa Jr, J.F., et al., Stent design properties and deployment ratio influence indexes of wall shear stress: a three-dimensional computational fluid dynamics investigation within a normal artery. Journal of Applied Physiology, 2004, 97(1): 424-430.

[68] Bukač, M., S. Čanić, J. Tambača, and Y. Wang, Fluid–structure interaction between pulsatile blood flow and a curved stented coronary artery on a beating heart: A four stent computational study. Computer Methods in Applied Mechanics and Engineering, 2019, 350: 679-700.

[69] Ng, J., et al., Local Hemodynamic Forces After Stenting: Implications on Restenosis and Thrombosis. Arteriosclerosis, Thrombosis, and Vascular Biology, 2017, 37(12): 2231-2242.

[70] Ku, D.N., Blood flow in arteries. Annual review of fluid mechanics, 1997, 29(1): 399-434.

[71] Gharleghi, R., et al., Advanced Multi-objective Design Analysis to Identify Ideal Stent Design, in Machine Learning and Medical Engineering for Cardiovascular Health and Intravascular Imaging and Computer Assisted Stenting. 2019, Springer. 193-200.

[72] Prithipaul, P.K., M. Kokkolaras, and D. Pasini, Assessment of structural and hemodynamic

performance of vascular stents modelled as periodic lattices. Medical Engineering & Physics, 2018, 57: 11-18.

[73] Stone, P.H., et al., Prediction of progression of coronary artery disease and clinical outcomes using vascular profiling of endothelial shear stress and arterial plaque characteristics: the PREDICTION Study. Circulation, 2012, 126(2): 172-181.

[74] Stone, P.H., et al., Effect of endothelial shear stress on the progression of coronary artery disease, vascular remodeling, and in-stent restenosis in humans: in vivo 6-month follow-up study. Circulation, 2003, 108(4): 438-44.

[75] Dolan, J.M., J. Kolega, and H. Meng, High wall shear stress and spatial gradients in vascular pathology: a review. Annals of Biomedical Engineering, 2013, 41(7): 1411-27.

[76] Ku, D.N., D.P. Giddens, C.K. Zarins, and S. Glagov, Pulsatile flow and atherosclerosis in the human carotid bifurcation. Positive correlation between plaque location and low oscillating shear stress. Arteriosclerosis: An Official Journal of the American Heart Association, Inc., 1985, 5(3): 293-302.

[77] Wentzel, J.J., et al., The influence of shear stress on in-stent restenosis and thrombosis. EuroIntervention, 2008, 4 Suppl C: C27-32.

[78] Traub, O. and B.C. Berk, Laminar shear stress: mechanisms by which endothelial cells transduce an atheroprotective force. Arteriosclerosis, Thrombosis, and Vascular Biology, 1998, 18(5): 677-685.

[79] Samady, H., et al., Coronary artery wall shear stress is associated with progression and transformation of atherosclerotic plaque and arterial remodeling in patients with coronary artery disease. Circulation, 2011, 124(7): 779-788.

[80] DePaola, N., M.A. Gimbrone, Jr., P.F. Davies, and C.F. Dewey, Jr., Vascular endothelium responds to fluid shear stress gradients. Arteriosclerosis and thrombosis : a journal of vascular biology, 1992, 12(11): 1254-7.

[81] Duraiswamy, N., R.T. Schoephoerster, and J.E. Moore, Jr., Comparison of near-wall hemodynamic parameters in stented artery models. Journal of Biomechanical Engineering, 2009, 131(6): 061006.

[82] LaDisa Jr, J.F., et al., Circumferential vascular deformation after stent implantation alters wall shear stress evaluated with time-dependent 3D computational fluid dynamics models. Journal of Applied Physiology, 2005, 98(3): 947-957.

[83] Wentzel, J.J., et al., Extension of increased atherosclerotic wall thickness into high shear stress regions is associated with loss of compensatory remodeling. Circulation, 2003, 108(1): 17-23.

[84] Keller, B.K., et al., Contribution of mechanical and fluid stresses to the magnitude of in-stent restenosis at the level of individual stent struts. Cardiovascular engineering and technology, 2014, 5(2): 164-175.

[85] Balossino, R., F. Gervaso, F. Migliavacca, and G. Dubini, Effects of different stent designs on local hemodynamics in stented arteries. Journal of Biomechanics, 2008, 41(5): 1053-61.

[86] Tominaga, R., et al., Effects of design geometry of intravascular endoprostheses on stenosis rate in normal rabbits. American Heart Journal, 1992, 123(1): 21-8.

[87] Rogers, C. and E.R. Edelman, Endovascular stent design dictates experimental restenosis and thrombosis. Circulation, 1995, 91(12): 2995-3001.

[88] Garasic, J.M., et al., Stent and artery geometry determine intimal thickening independent of arterial injury. Circulation, 2000, 101(7): 812-8.

[89] Berry, J.L., et al., Experimental and computational flow evaluation of coronary stents. Annals of Biomedical Engineering, 2000, 28(4): 386-98.

[90]   Wentzel, J.J., et al., Relationship between neointimal thickness and shear stress after Wallstent implantation in human coronary arteries. Circulation, 2001, 103(13): 1740-1745.

[91]   LaDisa Jr, J.F., et al., Alterations in wall shear stress predict sites of neointimal hyperplasia after stent implantation in rabbit iliac arteries. American Journal of Physiology-Heart and Circulatory Physiology, 2005, 288(5): H2465-H2475.

[92]   Jimenez, J.M. and P.F. Davies, Hemodynamically driven stent strut design. Annals of Biomedical Engineering, 2009, 37(8): 1483-94.

[93]   Gundert, T.J., A.L. Marsden, W. Yang, and J.F. LaDisa, Optimization of cardiovascular stent design using computational fluid dynamics. Journal of Biomechanical Engineering, 2012, 134(1).

[94]   Wei, L., H.L. Leo, Q. Chen, and Z. Li, Structural and Hemodynamic Analyses of Different Stent Structures in Curved and Stenotic Coronary Artery. Frontiers in Bioengineering and Biotechnology, 2019, 7: 366.

[95]   He, Y., N. Duraiswamy, A.O. Frank, and J.E. Moore, Jr., Blood flow in stented arteries: a parametric comparison of strut design patterns in three dimensions. Journal of Biomechanical Engineering, 2005, 127(4): 637-47.

[96]   Freeman, J.W., P.B. Snowhill, and J.L. Nosher, A link between stent radial forces and vascular wall remodeling: the discovery of an optimal stent radial force for minimal vessel restenosis. Connective Tissue Research, 2010, 51(4): 314-326.

[97]   Otsuka, F., et al., Pathologic etiologies of late and very late stent thrombosis following first-generation drug-eluting stent placement. Thrombosis, 2012, 2012.

[98]   Gundert, T.J., et al., A rapid and computationally inexpensive method to virtually implant current and next-generation stents into subject-specific computational fluid dynamics models. Annals of Biomedical Engineering, 2011, 39(5): 1423-1437.

[99]   Ellwein, L.M., et al., Optical coherence tomography for patient-specific 3D artery reconstruction and evaluation of wall shear stress in a left circumflex coronary artery. Cardiovascular engineering and technology, 2011, 2(3): 212.

[100]   Chiastra, C., et al., Computational fluid dynamic simulations of image-based stented coronary bifurcation models. Journal of the Royal Society, Interface, 2013, 10(84): 20130193.

[101]   Bourantas, C.V., et al., Fusion of optical coherence tomographic and angiographic data for more accurate evaluation of the endothelial shear stress patterns and neointimal distribution after bioresorbable scaffold implantation: comparison with intravascular ultrasound-derived reconstructions. The international journal of cardiovascular imaging, 2014, 30(3): 485-94.

[102]   Thondapu, V., et al., Improvement in local haemodynamics 5 years after implantation of a coronary bioresorbable scaffold: a pulsatile non-Newtonian shear stress analysis. European heart journal cardiovascular Imaging, 2017, 18(11): 1294.

[103]   Thondapu, V., et al., Interventional cardiology Endothelial shear stress 5 years after implantation of a coronary bioresorbable scaffold. 2018.

[104]   Chiastra, C., G. Dubini, and F. Migliavacca, Hemodynamic perturbations due to the presence of stents, in Biomechanics of Coronary Atherosclerotic Plaque. 2020, Elsevier. 257-278.

[105]   Young, D.F. and F.Y. Tsai, Flow characteristics in models of arterial stenoses—I. Steady flow. Journal of Biomechanics, 1973, 6(4): 395-410.

[106]   Young, D.F. and F.Y. Tsai, Flow characteristics in models of arterial stenoses—II. Unsteady flow. Journal of Biomechanics, 1973, 6(5): 547-559.

[107] Gould, K.L., K.O. Kelley, and E.L. Bolson, Experimental validation of quantitative coronary arteriography for determining pressure-flow characteristics of coronary stenosis. Circulation, 1982, 66(5): 930-7.

[108] Morlacchi, S., et al., Stent deformation, physical stress, and drug elution obtained with provisional stenting, conventional culotte and Tryton-based culotte to treat bifurcations: a virtual simulation study. EuroIntervention: journal of EuroPCR in collaboration with the Working Group on Interventional Cardiology of the European Society of Cardiology, 2014, 9(12): 1441.

[109] Beier, S., et al., Vascular hemodynamics with computational modeling and experimental studies, in Computing and Visualization for Intravascular Imaging and Computer-Assisted Stenting. 2017, Elsevier. 227-251.

[110] Seo, T., L.G. Schachter, and A.I. Barakat, Computational study of fluid mechanical disturbance induced by endovascular stents. Annals of Biomedical Engineering, 2005, 33(4): 444-56.

[111] Razavi, A., E. Shirani, and M. Sadeghi, Numerical simulation of blood pulsatile flow in a stenosed carotid artery using different rheological models. Journal of Biomechanics, 2011, 44(11): 2021-2030.

[112] Johnston, B.M., P.R. Johnston, S. Corney, and D. Kilpatrick, Non-Newtonian blood flow in human right coronary arteries: transient simulations. Journal of Biomechanics, 2006, 39(6): 1116-28.

[113] Zeng, D., Z. Ding, M.H. Friedman, and C.R. Ethier, Effects of cardiac motion on right coronary artery hemodynamics. Annals of Biomedical Engineering, 2003, 31(4): 420-9.

[114] Mattace-Raso, F.U., et al., Arterial stiffness and risk of coronary heart disease and stroke: the Rotterdam Study. Circulation, 2006, 113(5): 657-63.

[115] Torii, R., et al., Fluid–structure interaction analysis of a patient-specific right coronary artery with physiological velocity and pressure waveforms. Communications in numerical methods in engineering, 2009, 25(5): 565-580.

[116] Chaichana, T., Z. Sun, and J. Jewkes, Computation of hemodynamics in the left coronary artery with variable angulations. Journal of Biomechanics, 2011, 44(10): 1869-78.

[117] Atherton, M. and R. Bates, Robust optimization of cardiovascular stents: a comparison of methods. Engineering optimization, 2004, 36(2): 207-217.

[118] Putra, N.K., et al. Stent design optimization based on Kriging surrogate model under deformed vessel wall: pulsatile inlet flow. in 2017 5th International Conference on Instrumentation, Control, and Automation (ICA). 2017. IEEE.

[119] Pant, S., G. Limbert, N.P. Curzen, and N.W. Bressloff, Multiobjective design optimisation of coronary stents. Biomaterials, 2011, 32(31): 7755-73.

[120] Amirjani, A., M. Yousefi, and M. Cheshmaroo, Parametrical optimization of stent design; a numerical-based approach. Computational Materials Science, 2014, 90: 210-220.

[121] Blouza, A., L. Dumas, and I. M'Baye. Multiobjective optimization of a stent in a fluid-structure context. in Proceedings of the 10th annual conference companion on Genetic and evolutionary computation. 2008.

[122] Srinivas, K., et al., Studies on design optimization of coronary stents. Journal of Medical Devices, 2008, 2(1).

[123] Bendsøe, M.P. and N. Kikuchi, Generating optimal topologies in structural design using a homogenization method. Computer Methods in Applied Mechanics and Engineering, 1988, 71(2): 197-224.

[124] Bendsøe, M.P. and O. Sigmund, Material interpolation schemes in topology optimization. Archive

of Applied Mechanics (Ingenieur Archiv), 1999, 69(9-10): 635-654.

[125] Zhou, M. and G.I.N. Rozvany, The COC algorithm, Part II: Topological, geometrical and generalized shape optimization. Computer Methods in Applied Mechanics and Engineering, 1991, 89(1-3): 309-336.

[126] Xie, Y.M. and G.P. Steven, A simple evolutionary procedure for structural optimization. Computers & structures, 1993, 49(5): 885-896.

[127] Sethian, J.A. and A. Wiegmann, Structural boundary design via level set and immersed interface methods. Journal of Computational Physics, 2000, 163(2): 489-528.

[128] Wang, M.Y., X. Wang, and D. Guo, A level set method for structural topology optimization. Computer Methods in Applied Mechanics and Engineering, 2003, 192(1-2): 227-246.

[129] Allaire, G., F. Jouve, and A.-M. Toader, Structural optimization using sensitivity analysis and a level-set method. Journal of Computational Physics, 2004, 194(1): 363-393.

[130] Wang, M.Y. and S. Zhou, Phase field: a variational method for structural topology optimization. CMES-Computer Modeling in Engineering and Sciences, 2004, 6(6): 547.

[131] Takezawa, A., S. Nishiwaki, and M. Kitamura, Shape and topology optimization based on the phase field method and sensitivity analysis. Journal of Computational Physics, 2010, 229(7): 2697-2718.

[132] Guo, X., W. Zhang, and W. Zhong, Doing topology optimization explicitly and geometrically—a new moving morphable components based framework. Journal of Applied Mechanics, 2014, 81(8).

[133] Guo, X., W. Zhang, J. Zhang, and J. Yuan, Explicit structural topology optimization based on moving morphable components (MMC) with curved skeletons. Computer Methods in Applied Mechanics and Engineering, 2016, 310: 711-748.

[134] Cioranescu, D. and J.S.J. Paulin, Homogenization in open sets with holes. Journal of mathematical analysis and applications, 1979, 71(2): 590-607.

[135] Suzuki, K. and N. Kikuchi, A homogenization method for shape and topology optimization. 1991.

[136] Diaz, A. and M. Bendsøe, Shape optimization of structures for multiple loading conditions using a homogenization method. Structural optimization, 1992, 4(1): 17-22.

[137] Allaire, G., Shape optimization by the homogenization method. Vol. 146. 2012: Springer Science & Business Media.

[138] Diaz, A. and O. Sigmund, Checkerboard patterns in layout optimization. Structural optimization, 1995, 10(1): 40-45.

[139] Sigmund, O. and J. Petersson, Numerical instabilities in topology optimization: a survey on procedures dealing with checkerboards, mesh-dependencies and local minima. Structural optimization, 1998, 16(1): 68-75.

[140] Huang, X. and Y.M. Xie, Bi-directional evolutionary topology optimization of continuum structures with one or multiple materials. Computational Mechanics, 2009, 43(3): 393.

[141] Huang, X. and Y.-M. Xie, A further review of ESO type methods for topology optimization. Structural and Multidisciplinary Optimization, 2010, 41(5): 671-683.

[142] Osher, S. and J.A. Sethian, Fronts propagating with curvature-dependent speed: algorithms based on Hamilton-Jacobi formulations. Journal of Computational Physics, 1988, 79(1): 12-49.

[143] Osher, S.J. and F. Santosa, Level set methods for optimization problems involving geometry and constraints: I. Frequencies of a two-density inhomogeneous drum. Journal of Computational Physics, 2001, 171(1): 272-288.

[144] Sokolowski, J. and J.-P. Zolésio, Introduction to shape optimization, in Introduction to shape

optimization. 1992, Springer. 5-12.

[145] Wang, M.Y. and X. Wang, "Color" level sets: a multi-phase method for structural topology optimization with multiple materials. Computer Methods in Applied Mechanics and Engineering, 2004, 193(6-8): 469-496.

[146] Osher, S., R. Fedkiw, and K. Piechor, Level set methods and dynamic implicit surfaces. Applied Mechanics Reviews, 2004, 57(3): B15-B15.

[147] Luo, Z., L. Tong, M.Y. Wang, and S. Wang, Shape and topology optimization of compliant mechanisms using a parameterization level set method. Journal of Computational Physics, 2007, 227(1): 680-705.

[148] Luo, Z., L. Tong, and Z. Kang, A level set method for structural shape and topology optimization using radial basis functions. Computers & structures, 2009, 87(7-8): 425-434.

[149] Sigmund, O., Materials with prescribed constitutive parameters: an inverse homogenization problem. International Journal of Solids and Structures, 1994, 31(17): 2313-2329.

[150] Sigmund, O. and S. Torquato, Composites with extremal thermal expansion coefficients. Applied Physics Letters, 1996, 69(21): 3203-3205.

[151] Sigmund, O., A new class of extremal composites. Journal of the Mechanics and Physics of Solids, 2000, 48(2): 397-428.

[152] Guest, J.K. and J.H. Prévost, Optimizing multifunctional materials: design of microstructures for maximized stiffness and fluid permeability. International Journal of Solids and Structures, 2006, 43(22-23): 7028-7047.

[153] Chen, J., Y. Huang, and M. Ortiz, Fracture analysis of cellular materials: a strain gradient model. Journal of the Mechanics and Physics of Solids, 1998, 46(5): 789-828.

[154] Gibson, L.J. and M.F. Ashby, Cellular solids: structure and properties. 1999: Cambridge university press.

[155] Christensen, R.M., Mechanics of cellular and other low-density materials. International Journal of Solids and Structures, 2000, 37(1-2): 93-104.

[156] Sigmund, O. and S. Torquato, Design of materials with extreme thermal expansion using a three-phase topology optimization method. Journal of the Mechanics and Physics of Solids, 1997, 45(6): 1037-1067.

[157] Guest, J.K. and J.H. Prévost, Design of maximum permeability material structures. Computer Methods in Applied Mechanics and Engineering, 2007, 196(4-6): 1006-1017.

[158] Zhang, W., et al., Using strain energy-based prediction of effective elastic properties in topology optimization of material microstructures. Acta Mechanica Sinica, 2007, 23(1): 77-89.

[159] Diaz, A.R. and O. Sigmund, A topology optimization method for design of negative permeability metamaterials. Structural and Multidisciplinary Optimization, 2010, 41(2): 163-177.

[160] Schwerdtfeger, J., et al., Design of auxetic structures via mathematical optimization. Advanced Materials, 2011, 23(22‑23): 2650-2654.

[161] Radman, A., X. Huang, and Y. Xie, Topological optimization for the design of microstructures of isotropic cellular materials. Engineering optimization, 2013, 45(11): 1331-1348.

[162] Andreassen, E., B.S. Lazarov, and O. Sigmund, Design of manufacturable 3D extremal elastic microstructure. Mechanics of Materials, 2014, 69(1): 1-10.

[163] Wang, Y., Z. Luo, N. Zhang, and Z. Kang, Topological shape optimization of microstructural metamaterials using a level set method. Computational Materials Science, 2014, 87: 178-186.

[164] Li, H., Z. Luo, L. Gao, and P. Walker, Topology optimization for functionally graded cellular composites with metamaterials by level sets. Computer Methods in Applied Mechanics and Engineering, 2018, 328: 340-364.

[165] Evans, K.E. and A. Alderson, Auxetic materials: functional materials and structures from lateral thinking! Advanced Materials, 2000, 12(9): 617-628.

[166] Lakes, R., Deformation mechanisms in negative Poisson's ratio materials: structural aspects. Journal of Materials Science, 1991, 26(9): 2287-2292.

[167] Masters, I. and K. Evans, Models for the elastic deformation of honeycombs. Composite structures, 1996, 35(4): 403-422.

[168] Smith, C.W., J. Grima, and K. Evans, A novel mechanism for generating auxetic behaviour in reticulated foams: missing rib foam model. Acta Materialia, 2000, 48(17): 4349-4356.

[169] Spadoni, A. and M. Ruzzene, Elasto-static micropolar behavior of a chiral auxetic lattice. Journal of the Mechanics and Physics of Solids, 2012, 60(1): 156-171.

[170] Frenzel, T., M. Kadic, and M. Wegener, Three-dimensional mechanical metamaterials with a twist. Science, 2017, 358(6366): 1072-1074.

[171] Fu, M., F. Liu, and L. Hu, A novel category of 3D chiral material with negative Poisson's ratio. Composites Science and Technology, 2018, 160: 111-118.

[172] Grima, J.N. and K.E. Evans, Auxetic behavior from rotating squares. 2000.

[173] Xia, L. and P. Breitkopf, Design of materials using topology optimization and energy-based homogenization approach in Matlab. Structural and Multidisciplinary Optimization, 2015, 52(6): 1229-1241.

[174] Zhang, H., Y. Luo, and Z. Kang, Bi-material microstructural design of chiral auxetic metamaterials using topology optimization. Composite structures, 2018, 195: 232-248.

[175] de Lima, C.R. and G.H. Paulino, Auxetic structure design using compliant mechanisms: A topology optimization approach with polygonal finite elements. Advances in Engineering Software, 2019, 129: 69-80.

[176] Wang, F., O. Sigmund, and J.S. Jensen, Design of materials with prescribed nonlinear properties. Journal of the Mechanics and Physics of Solids, 2014, 69: 156-174.

[177] Clausen, A., et al., Topology optimized architectures with programmable Poisson's ratio over large deformations. Advanced Materials, 2015, 27(37): 5523-5527.

[178] Wang, F., Systematic design of 3D auxetic lattice materials with programmable Poisson's ratio for finite strains. Journal of the Mechanics and Physics of Solids, 2018, 114: 303-318.

[179] Zong, H., et al., On two-step design of microstructure with desired Poisson's ratio for AM. Materials & Design, 2018, 159: 90-102.

[180] Wang, S. and M.Y. Wang, Radial basis functions and level set method for structural topology optimization. International journal for numerical methods in engineering, 2006, 65(12): 2060-2090.

[181] Luo, Z., M.Y. Wang, S. Wang, and P. Wei, A level-set-based parameterization method for structural shape and topology optimization. International journal for numerical methods in engineering, 2008, 76(1): 1-26.

[182] Wendland, H., Piecewise polynomial, positive definite and compactly supported radial functions of minimal degree. Advances in computational Mathematics, 1995, 4(1): 389-396.

[183] Takahira, H., T. Horiuchi, and S. Banerjee, An Improved Three-Dimensional Level Set Method for Gas-Liquid Two-Phase Flows. Journal of Fluids Engineering, 2004, 126(4): 578-585.

[184] Yue, W., C.-L. Lin, and V.C. Patel, Coherent Structures In Open-Channel Flows Over a Fixed Dune. Journal of Fluids Engineering, 2005, 127(5): 858-864.

[185] Park, K.-S. and S.-K. Youn, Topology optimization of shell structures using adaptive inner-front (AIF) level set method. Structural and Multidisciplinary Optimization, 2007, 36(1): 43-58.

[186] Suzuki, K. and N. Kikuchi, A homogenization method for shape and topology optimization. Computer Methods in Applied Mechanics and Engineering, 1991, 93(3): 291-318.

[187] Guest, J.K. and J.H. Prévost, Topology optimization of creeping fluid flows using a Darcy–Stokes finite element. International journal for numerical methods in engineering, 2006, 66(3): 461-484.

[188] Wang, Y., Z. Luo, N. Zhang, and Q. Qin, Topological shape optimization of multifunctional tissue engineering scaffolds with level set method. Structural and Multidisciplinary Optimization, 2016, 54(2): 333-347.

[189] Hughes, T.J., L.P. Franca, and M. Balestra, A new finite element formulation for computational fluid dynamics: V. Circumventing the Babuška-Brezzi condition: A stable Petrov-Galerkin formulation of the Stokes problem accommodating equal-order interpolations. Computer Methods in Applied Mechanics and Engineering, 1986, 59(1): 85-99.

[190] Nakshatrala, K., D. Turner, K. Hjelmstad, and A. Masud, A stabilized mixed finite element method for Darcy flow based on a multiscale decomposition of the solution. Computer Methods in Applied Mechanics and Engineering, 2006, 195(33-36): 4036-4049.

[191] Masud, A. and T.J. Hughes, A stabilized mixed finite element method for Darcy flow. Computer Methods in Applied Mechanics and Engineering, 2002, 191(39-40): 4341-4370.

[192] Babuška, I., Error-bounds for finite element method. Numerische Mathematik, 1971, 16(4): 322-333.

[193] Brezzi, F., On the existence, uniqueness and approximation of saddle-point problems arising from Lagrangian multipliers. Publications mathématiques et informatique de Rennes, 1974(S4): 1-26.

[194] Whitaker, S., Flow in porous media I: A theoretical derivation of Darcy's law. Transport in Porous Media, 1986, 1(1): 3-25.

[195] Sánchez-Palencia, E., Non-homogeneous media and vibration theory. Lecture Notes in Physics, 1980, 127.

[196] Marler, R.T. and J.S. Arora, Survey of multi-objective optimization methods for engineering. Structural and Multidisciplinary Optimization, 2004, 26(6): 369-395.